UNIVERSITÀ
POLITECNICA
DELLE MARCHE

Università Politecnica delle Marche

DIPARTIMENTO DI INGEGNERIA INDUSTRIALE E SCIENZE MATEMATICHE - DIISM

Corso di Dottorato di Ricerca in Ingegneria Industriale – Curriculum Ingegneria Energetica

Ph.D. Thesis

Experimental and numerical analysis of natural convection in a square cavity with a vertical baffle

Advisor:
Prof. Corvaro Francesco

Ph.D. Dissertation of:
Benucci Maurizio

Curriculum Supervisor:
Prof. Ferruccio Mandorli

XVI Edition – New Series

Alla mia famiglia

Contents

List of Figures

List of Tables

Abstract

In this work, natural convection in a square cavity with an internal vertical obstacle and differentially heated from the side has been studied. Air is the working fluid and the divider is large, poorly conducting and located on the floor of the enclosure. Three divider position and four divider heights (or aperture ratio A_p) are considered. The effect of the direction of the gravity vector is also investigated for a certain number of inclination angle. PIV (Particle Image Velocimetry) system has been used to measure the flow field within the cavity; contour velocity maps and streamlines has been extracted. Was found that for all the configurations and for the entire field of Ra analyzed, the flow pattern remains the same. However, increasing the tilting angle, the flow pattern within the cavity considerably changes and four different vortices can be seen for $\theta = \frac{\pi}{2}$. Experimental results have been compared with numerical data, obtained through CFD simulation: both pure convective and combined convective-radiative models have been adopted to predict the flow and thermal field. A very good agreement between experimental and numerical results was found, especially for the radiative model when $A_p \geq 2/5$. Numerical isotherms and calculated Nusselt number value along the hot wall have been reported to evaluate the heat exchange. Results show that the inclination angle and the presence of the obstacle affected the thermal field within the cavity; divider height had a stronger effect on the enclosure heat transfer than the baffle position.

Sommario

Il presente documento descrive il lavoro di ricerca effettuato relativamente alla convezione naturale in una cavità quadrata in presenza di un ostacolo verticale posizionato internamente. Il fluido analizzato è aria in condizioni di flusso laminare e stazionario; le pareti laterali della cavità sono raffreddate e riscaldate attraverso degli scambiatori a piastre. Gli effetti della posizione e dell'altezza dell'ostacolo, valutate a diversi angoli di inclinazione della cavità sono stati studiati attraverso prove sperimentali (PIV) e indagine numerica (CFD) e valutati per mezzo di mappe scalari di velocità, temperatura e line di flusso. I risultati sperimentali hanno mostrato come lo schema del flusso convettivo, caratterizzato da un vortice principale e uno secondario, rimanga sostanzialmente invariato nell'intero campo di Ra e per tutte le configurazioni considerate; solamente

per angoli di inclinazione prossimi a $\frac{\pi}{2}$ il flusso si divide in quattro differenti vortici. I risultati del modello numerico mostrano un ridotto scostamento rispetto all'analisi sperimentale e permettono di individuare l'importanza dello scambio termico radiativo sulle configurazioni analizzate. La presenza dell'ostacolo e la variazione dell'angolo di inclinazione della cavità influenzano notevolmente l'intero campo di temperatura; tuttavia l'altezza dell'ostacolo ha un effetto maggiore sullo scambio termico attraverso le superfici della cavità rispetto alla posizione dello stesso.

Introduction

Convection is one of the three modes of heat transfer and takes place between a solid surface and the adjacent moving fluid. This thermal exchange phenomenon implies combined effects of conduction and mass transport. Contrary to forced convection, natural convection as a mean of thermal control does not require the installation of external mechanical devices as fans or pumps. Moreover, the use of natural convection does not develop noise and vibration in the surrounding environment as it is based on the floating effect experienced by the gravity fluid to guide the heat transfer process. In addition to the advantage of its spontaneous nature, natural convection excludes the risk of mechanical malfunction existing for systems activated by forced convection. The absence of mechanical equipment also allows reducing the overall size that often represents a significant constraint and a large cost factor in industrial design. On the other hand, natural convection, while being a heat transfer method less effective than forced convection, is widely used because it does not require any specific equipment in order to function, reducing electrical and electronic failure risks and involves important cost savings.

For these reasons, the attention to this topic has grown from the 1980s, especially for equipment located in limited volumes (cavities or enclosures). Natural convection in cavities, also known as internal convection, has been widely addressed for many years due to its effectiveness and the large number of applications in a lot of sectors and industries: building [1–3] and construction supply [4], fire safety, electronics [5], thermal conversion of solar energy and other renewables [6], refrigerators, storage devices, furnaces, cooling of nuclear reactors and many others. Natural convective phenomena were usually investigated experimentally, numerically and/or theoretically. Bairi *et al.* review work [7] shows that in recent years since computers have made numerical investigation fast and reliable, the number of works about the numerical analysis of various configurations has increased. However, the experimental analysis is still of great importance and allows to understand how the phenomenon of thermal exchange by natural convection really takes place. In fact, many aspects remain unclear and continue to be studied by researchers from all over the world. Moreover, the validation of the numerical models would be impossible without comparing numerical results with the results of the experimentation.

The objective of this thesis is to investigate natural convection in a square cavity by determining how the presence, position and height of a vertical baffle applied to the lower surface influence velocity pattern and thermal exchange. The evaluation of radiant effect is taken into account from a numerical point of view. Moreover, for a simple case, the effect of cavity inclination is studied. This analysis is performed through numerical temperature maps and both experimental (Particle Image Velocimetry) and numerical velocity field and streamlines. The average Nusselt number on the hot wall determined numerically is also compared with literature values to enhance the comprehension of

heat transfer. The experiments were carried out using experimental Particle Image Velocimetry (PIV) and numerical CFD techniques through ANSYS Fluent.

Chapter 1

Overview of natural convection in cavity

1.1 General concept of natural convection

The convective mode of heat transfer is generally divided into two basic processes: forced convection if the motion of the fluid is induced by external means as fans, blowers, the wind or the motion of the heated object itself, and natural convection if the flow field is generated by a density difference or density gradient. This density difference may result from a temperature or concentration different (or gradient) in a body force field. The most common body force is the gravitational force, but the body force resulting from centrifugal or Coriolis forces is also possible. The combined body force and the density difference or gradient will produce buoyancy force within the fluid, which is the driving force behind natural convection. Some examples of natural convection are the buoyant flow arising from heat or material rejection to the atmosphere, heating and cooling of rooms and buildings, recirculating flow driven by temperature and salinity differences in oceans, and flows generated by fires.

While the flow field for most forced convection problems is generally known or can be solved apart from the temperature distribution, in natural convection it results from the interaction of the density difference with the gravitational (or some other body force) field and is therefore inevitably linked with; the flow field and temperature distribution cannot be solved separately. The differences between natural and forced convection make the analytical and experimental study of processes involving natural convection much more complicated than those involving forced convection. A special technique must be developed to handle the coupling between the flow and heat transfer. To understand the physical nature of natural convection can be considered the heat transfer from a heated vertical flat plate placed in a quiescent fluid at a uniform temperature. The surface temperature of the plate, T_w, is higher than the temperature of the quiescent fluid, T_∞. The fluid adjacent to the heated vertical plate becomes lighter due to a decreasing density and rises $\partial\rho/\partial T < 0$. The heated fluid flows up and the fluid from the neighbor moves in due to the generated pressure differences taking the place of this rising fluid. The densities of most liquids and gases decrease with increasing temperature with a few exceptions, such as water between 0 °C and 4 °C.

In a thin layer of fluid heated to the vertical plate, the temperature is higher than the quiescent fluid temperature T_∞ and a thermal boundary layer is formed.

Consequently, as the fluid near the heated vertical plate rises, a velocity boundary layer also forms. Depending on the Prandtl number of the fluid:

- if $Pr > 1$ the velocity boundary layer is thicker than the thermal boundary layer (see fig. 1.1[1]);
- if $Pr < 1$ the velocity boundary layer is thinner than the thermal boundary layer.

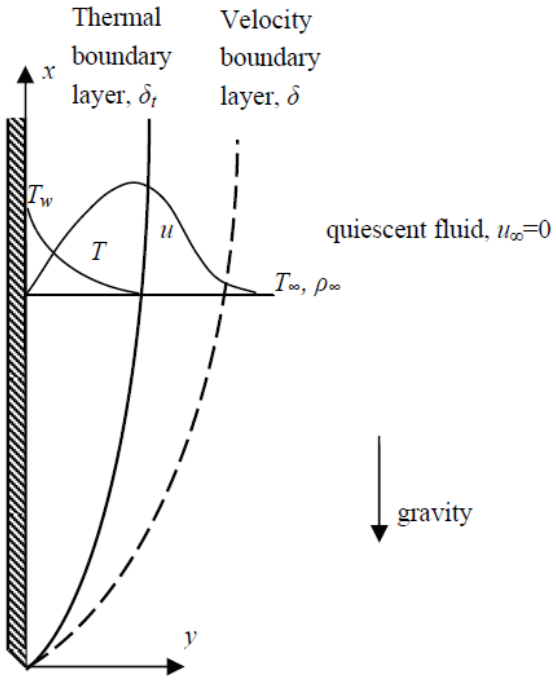

Figure 1.1: Natural convection over a vertical flat plate ($Pr > 1$)

Heat transfer from the vertical surface can be described using Newton's law of cooling which gives the relationship between the heat transfer rate q and the temperature difference between the surface and the ambient as

$$q'' = h_x(T_w - T_\infty) \tag{1.1}$$

where h_x is the average convective heat transfer coefficient, which depends on flow configurations and the properties of the fluid. It usually also depends on the temperature difference, $T_w - T_\infty$, which means that the heat flux is not a linear function of the temperature difference. At the surface of the heated plate, the velocity of the fluid is zero due to the no-slip condition. Therefore, conduction is the mechanism of heat transfer from the heated plate to the fluid in its immediate vicinity so the heat transfer can be described by Fourier's law of conduction:

$$q'' = \lambda \left(\frac{\partial T}{\partial y} \right)_{y=0} \tag{1.2}$$

[1]Y. Zhang, A. Faghri, J. R. Howell, 2010. Advanced heat and mass transfer. Global Digital Press, Columbia, MO 65203, USA.

Here the temperature gradient is evaluated at the surface, $y = 0$, in the fluid and λ is the thermal conductivity of the fluid. Combining equations. 1.1 and 1.2 yields:

$$h_x = -\frac{\lambda}{T_w - T_\infty}\left(\frac{\partial T}{\partial y}\right)_{y=0} \tag{1.3}$$

This equation can be used to determine the local heat transfer coefficient. It reveals that the temperature profile in the thermal boundary layer is required to determine the heat transfer coefficient. The term h_x is generally given in terms of a nondimensional parameter called Nusselt number Nu. It is defined as:

$$Nu_x = \frac{h_x x}{\lambda} \tag{1.4}$$

When natural convection mechanism occurs in an enclosure it is named internal convection. In this case the development of the boundary layer is restricted by the wall of the enclosure. Internal natural convection differs from the cases of external convection, where a heated or cooled wall is in contact with the quiescent fluid and the boundary layer can be developed without any restriction. For this reason, internal convection usually cannot be treated using simple boundary layer theory because the entire fluid in the enclosure takes part in the convection.

1.2 Square and rectangular cavity with internal baffle

In many engineering applications, mainly motivated by the design of modern electronic packages, the cavity is partitioned by attaching baffle to its vertical and (or) horizontal walls. The size and position of these kind of obstructions would change the characteristics of flow and heat transfer in the horizontal and vertical enclosures. Electronic devices are generally modeled as a cavity with heat sources and internal dividers; the analysis of internal obstacles is used to better understand the phenomenon in these conditions. In order to meet the growing demand of engineering applications, a considerable effort was made to understand heat dissipation in enclosures caused by heat sources with the intention of decreasing hot-spot temperatures in the enclosure. A review of scientific literature shows that several researchers confirmed the significant impact of both the size and the position of the internal baffle on natural convective heat transfer.

A wide number of obstacles geometry, material and position within the cavity were studied numerically and experimentally but the most interesting applications from the industrial point of view are rectangular baffles (horizontally and vertically placed).

Duxbury [8] at first conducted experimental tests in a centrally divided air-filled cavity through a holographic interferometric system. He investigated a lot of baffle height for a range of Rayleigh number of $8 \times 10^4 < Ra < 5 \times 10^6$ and noted a tendency of the flow to separate behind the obstacle. Using the finite element method, Winters [9] numerically investigated natural convection in a rectangular cavity with one projecting upwards or downwards divider. The obstacle was centrally located and the effect of the baffle height was studied for $10^4 < Ra < 10^6$. Assuming adiabatic end walls, the researcher obtained a series of flow patterns that were qualitatively similar to the ones described by Duxbury; although the numerical model was not able to predict the flow separation behind the divider experimentally observed in previous works. Moreover, due to the considerable heat loss through the walls of the cavity

during experimental test, quantitative differences between numerical and experimental results were found. Nansteel and Greif [10], performed experimental investigation with water and for high Rayleigh number between 2.3×10^{10} and 1.1×10^{11}. Using both conducting and non-conducting partition materials in a rectangular cavity with aspect ratio of $1/2$, researchers found that partial divisions have a significant effect on the heat transfer, especially when dividers are adiabatic. Nansteel and Greif [11] attached a thin flat on the upper wall of a rectangular enclosure with aspect ratio of $1/2$ and performed an experimental investigation for $10^{10} < Ra < 10^{11}$ using water. They demonstrated that the flow pattern and the temperature field remain qualitatively unaltered even when the partition is moved along the top of the cavity. The cross-cavity heat transfer was showed to be only dependent on the partition location. In the same paper researchers also analyzed the case of a vertical obstacle placed at the floor of the cavity for $Ra = 10^{10}$ and results were in direct contrast to the study of Duxbury [8] and Winters [9]. Nansteel and Greif observed that the flow separation occurs in front of the divider instead of behind it. Lin and Bejan [12] carried out an experimental and analytical study of a rectangular enclosure (aspect ratio=$1/2$) filled with water and fitted with an incomplete internal partition. For a Rayleigh number range of $10^9 - 10^{10}$ it was demonstrated that the height of the partition has a strong effect on both the heat transfer rate and the flow pattern. Flow patterns similar to those noted by Nansteel and Greif [10] were observed but experimental Nusselt numbers obtained were appreciably lower than Nansteel and Greif's results. Winters [13] numerically investigated the effect of the divider height, the divider conductivity, the fluid Prandtl number (Pr) and the cavity aspect ratio on natural convection mechanism in a rectangular cavity for Rayleigh numbers between $10^6 - 10^{11}$. Results show that all these factors influence the heat transfer rate and velocity field inside the cavity. In direct contrast to the studies of Duxbury [8] and in accordance with Nansteel and Greif [11] and Lin and Bejan [12] results, Winters noted that the flow separation occurred in front of the divider instead of behind it. Kirkpatrick *et al.* [14] performed a numerical study of natural convection of air in a vertical enclosure with a centrally located divider. Results were obtained at lower Rayleigh numbers, and no flow separation in front of the partial divider was noted. The heat transfer results of Kirkpatrick agreed within 10% to Nansteel and Greifs [11] data, but differed substantially from Lin and Bejan's [12] values. Also Zimmerman and Acharya [15] performed a numerical study of natural convection in an enclosure with a finitely conducting vertical baffle. In agreement with experimental correlation of Lin and Bejan [12] they found that the baffle strongly influences the hot wall Nusselt number distribution, but it has a weaker effect on the cold wall Nusselt number profile. Jetli and Acharya [16, 17] numerically investigated the effect of baffle height and position on the flow and heat transfer characteristics in a differentially heated cavity. The used divider was thin, poorly conducting and projecting upwards from the floor of the square enclosure; three baffle height and position were considered. Authors compared numerical results with previous experimental and numerical studies and found that the enclosure heat transfer is strongly influenced by the aperture ratio A_p. However, the divider position has a rather small effect on the overall heat transfer from the enclosure. They especially investigated the area between the divider and the cold wall; at lower Rayleigh numbers ($10^5 - 10^6$) the flow is weak in this zone and researchers noted a tendency of the flow to separate behind the divider. At higher Rayleigh numbers ($> 10^9$) the stratification is significant in this region and causes the flow detaching directly from the cold wall causing a separation in front of the divider. More recently steady-state natural convection in a rectangular enclosure containing R114 gas was studied by Olson *et al.* [18].

In addition to the aforementioned studies, a wide number of authors analyzed the effect of multiple upwards and downwards partitions of a rectangular and square cavity on the heat transfer across the enclosure. Probert and Ward [19] and Janikowski *et al.* [20] at first analyzed a rectangular cavity with high aspect ratio and either inline or offset dividers. Interesting experimental tests were conducted by Bajorek and Lloyd [21] using a Mach-Zehnder interferometer in a partitioned square enclosure. Their results were compared with computational results obtained by Zimmerman and Acharya [15] and Jetli *et al.* [16, 22, 23]. Recently Han and Baek [24] introduced in their numerical study the effect of radiative heat exchange in a rectangular enclosure with two incomplete partitions for high Rayleigh numbers. Results showed that with radiation, the temperature at the region between the baffle and the hot wall is more uniform and the region near the cold wall is more thermally affected. Moreover the radiation is the main heat transfer mode near the hot wall, however, since the presence of partitions, convective heat transfer is more influent near the cold wall. Bilgen [25] investigated laminar and turbulent natural convection in enclosures with partial divisions. He numerically studied the effect of various geometrical parameters as aspect ratio of the cavity ($A = 0.3$ to 0.4), divider position ($D = 0.5 - 0.6$) and height of the partitions ($C = 0$ to 0.15) for a wide range of Rayleigh number (10^4 to 10^{11}). The results showed that the flow regime was laminar for Ra up to 10^8 and turbulent thereafter. The heat transfer was reduced when two partitions were used instead of one, when the aspect ratio was made smaller and when the position of partitions was farther away from the hot wall. Ambarita *et al.* [26] performed numerical simulations of a square cavity modifying both the baffles height and distance in a range of Ra between $10^4 - 10^8$. Depending on the baffles position and Ra, two different flow patterns were noted. The first pattern is characterized by two different vortices separated by a trapped fluid between the obstacles and the second pattern shows a primary vortex strangled by two trapped fluids. Recently, an interesting application to reduce the natural convection in the voids of hollow blocks was numerically investigated by Alhazmy [4]. Costa [27] numerically studied the overall heat transfer performance of a partitioned square cavity filled with air. The researcher considered two partitions of finite thickness placed in the enclosure following an ordered arrangement. The position, length and thermal conductivity of the baffle vary for some values of Rayleigh number and for different thermal boundary conditions. The most important result was that some combinations of the placement and length of the dividers could lead to the same thermal performance of the enclosure.

Jani *et al.* [28] performed numerical simulation of a divided square cavity heated from below and cooled from sides. The effects of the Rayleigh number and of the divider length on the velocity map and Nusselt number inside the enclosure were investigated. Results showed the presence of two competing mechanisms that are responsible for the flow and thermal modifications: the resistance effect of the fin due to the friction losses which directly depends on the length of the fin, and the extra heating of the fluid that is offered by the fin. Researchers observed that placing a hot fin in the middle of the bottom wall, for high Rayleigh numbers, it has a more remarkable effect on the flow field and heat transfer inside the cavity. Sun and Emery [29] numerically and experimentally examined an air-filled enclosure containing an internal baffle for a wide range of Rayleigh number and baffle heights. The effect of Rayleigh numbers, number of partition and height of divider on the Nusselt number and fluid flow are numerically investigated by Yucel and Ozdem [30]. They observed that the Nusselt number increases when the Rayleigh number increases and decreases as the number of partitions increases. However, Nu reduction is less at low Rayleigh numbers. Furthermore, increasing

partition height, the average Nusselt number decreases. Buoyancy-driven convection in a square cavity induced by two mutually orthogonal and arbitrarily located thin baffles was studied numerically by Kandaswamy *et al.* [31, 32] and Abdul Hakeem *et al.* [33, 34]. Results showed that buoyancy force plays a key role in the thermal exchange and overall heat transfer in the cavity is enhanced for higher values of both baffle and cavity ratios. Flow inhibition emerges as a deciding factor and diminishes the heat transfer when the horizontal baffle is located above the center of the cavity. Corvaro and Paroncini [35] presented an experimental study using Particle Image Velocimetry (PIV) to investigate the effect of the position of an active divider with a height of $H/2$. They found that the central position of the vertical baffle is the best for the heat transfer and observed the presence of small vortical structures on the upper surface of the divider generated by the flow separation in proximity to its corner. Experimental and numerical analysis of natural convection in a square cavity with two vertical baffles were performed by Corvaro *et al.* [36]. PIV method was used to analyze the effect of baffles height for a Rayleigh number range from 10^4 to 10^5. Results confirmed that the increase of the height of the obstacles causes a reduction in convective heat transfer rate up to 27%. Laminar natural convection heat transfer in a differentially heated cavity with two thin porous fins attached to the hot wall was studied numerically by Alshuraiaan and Khanafer [37] for various Richardson number, Darcy number (Da), thermal conductivity ratio, and location of the porous fin. Results showed that the presence of a horizontal porous fin increases the average Nusselt number (Nu) when compared with the differentially heated cavity for various Richardson numbers and thermal conductivity ratios. However, a vertical porous fin attached to the bottom insulated surface exhibited a lower average Nusselt number than the no-fin case. A numerical analysis comparing steady natural convection of water and air in a two dimensional, partially divided, rectangular enclosure was presented by Khan and Guang-Fa [38]. Four opening ratios were investigated for a Rayleigh number field from 10^6 to 10^8; also the effect of opened partitions was observed. The study demonstrates that the use of water to model air convection in partitioned enclosures gives reasonable heat transfer results. The average Nusselt number obtained for water is only 2 - 5% larger than the Nusselt number for air under the same conditions. The flow configuration and exchange flow rates for water and air are, however, different. The exchange flow rate of water was found to be 10 - 20% larger than the case with air. The presence of an opening in the partition reduces the exchange volume flow rates by 5.68 - 15.2% for water and 1 - 11 .4% for air, depending on the Rayleigh number and the opening ratio. Hanjalic *et al.* [39] studied numerically natural convection in rectangular enclosures having different aspect ratios ($A = 0.33$, 0.5 and 0.67). They studied the empty enclosure with the bottom and the side heating and a partially divided enclosure with side heating. The latter corresponded to the experimentally studied case by Nansteel and Greif [10] in which a partition was hanging from the top of the enclosure having an aspect ratio of 0.5 and a partition length of $0.25 - 0.75$. The main interest of this study was to investigate the transition phenomenon from laminar to turbulent flow.

1.3 Variables affecting natural convection in cavity

In case of axial-symmetric flow, the phenomenon can be studied in 2D and a limited number of variables affect the fluid flow and the heat transfer mechanism. These variables are the thermal boundary conditions, the geometry of the cavity, the Rayleigh

number (Ra) and the direction of the gravity vector (cavity inclination). An extensive review of researches on natural convection in cavities was performed by Bairi *et al.* [7]. Studies about the position relative to the vertical direction of the active sources found a practical use in electronic devices contained in airborne enclosure in which the correct thermal regulation must be maintained for all configurations. This aspect was experimentally and numerically evaluated by several authors. Bairi *et al.* [40, 41], Beya and Lili [42], Biswal *et al.* [43], Cianfrini et al. [44], Corvaro *et al.* [45], Elsherbiny and Ismail [46] And Ozoe *et al.* [47] for square and rectangular non-partitioned cavities. Chao *at al.* [48] first experimentally investigated the possibility of reducing heat transfer by natural convection in a differentially heated and partitioned enclosure. The Nusselt number and velocity pattern of six baffle configurations for a wide number of inclination angles were studied. Results showed that the heat transfer was closely related to the flow pattern within the cavity and the presence of the baffle reduced the overall rate of heat transfer at all angles of inclination because of the reduction of the rate of circulation. Ghassemi *et al.* [49] performed numerical simulations to study the effect of inclination angle on flow field and heat transfer in a differentially heated square cavity with two insulated baffles attached to its isothermal walls. Also, the baffle lengths and the relative position of the baffles were changed. They confirmed that the presence of the baffles reduces the heat exchange and Nusselt number reaches the minimum value at an inclination angle of $\frac{\pi}{2}$ for all baffle configurations. Also the baffles position and length affect Nu. Altac and Kurtol [50] numerically studied the thermal performances of a rectangular cavity with a thin internal vertically situated hot plate for an enclosure aspect ratio of $A = 1$ and $A = 2$. The Rayleigh number and the tilt angle of the enclosure are ranged from 10^5 to 10^7 and from 0 to $\frac{\pi}{2}$, respectively. Depending on the aspect ratio, they found two different trends of the mean Nusselt number that for the square cavity reaches its maximum value at $\frac{\pi}{8}$. With increasing aspect ratio, heat transfer rate increases for all tilt angles and Ra.

Moreover, the contribution of radiation is important in the thermal exchanges in cavity because thermal radiation is omnipresent in applications and its effect must usually be investigated (Liu and Phan-Thien [51], Bouali *et al.* [52], Sun *et al.* [53], Saravanan and Sivaraj [54], Sivaraj and Sheremet [55]). Yucel and Acharya [56] numerically investigated combined natural convection and radiation thermal exchange in a differentially heated and partially divided square enclosure. The effect of thermal radiation on the heat transfer and flow patterns in partially or fully divided enclosures is examined for a Rayleigh number of 10^5; Discrete Ordinates Method (DOM) was used for both radiating and non-radiating fluid. Results revealed that radiation is the dominant mode of heat transfer and leads to significant increases in the velocity values and the total heat transfer rate. The radiative interaction between the hot sidewall and the divider surface has a strong influence on the flow pattern and can lead to separation of flow behind the divider at small divider heights. The Discrete Transfer, the Discrete Ordinates and the Finite Volume Methods were employed by Coelho *et al.* [57] to numerically investigate radiation in an enclosure containing obstacles of very small thickness. All models predict similar flow patterns and thermal behaviors of the cavity but the computational requirements are different; the Discrete Ordinates and the Finite Volume Method are the most economical ones. The predicted influence of the baffles on the distribution of the heat fluxes exhibits the expected trends: a reduction of the heat transfer rate.

Chapter 2

Materials and methods

2.1 Experimental technique

Experimental analysis of the effect of an internal baffle on the flow pattern in a differentially heated square cavity was performed through Particle Image Velocimetry (PIV). PIV is an optical technique used to detect the instantaneous velocity field of a fluid in the plane of the motion. In most applications, the fluid flow has to be inseminated with particles suitable to follow the path. These particles are illuminated at least twice within a short time interval by a laser beam. A digital camera, placed perpendicularly on the plane of the light, registers the position of lighted particles. The displacement of the particle images between the light pulses is determined through evaluation of PIV recordings. The digital PIV recording is divided into small subareas called *interrogation areas*. Available algorithms, usually cross-correlation algorithms, are able to determine the projection of the vector of the local flow velocity into the plane of the light sheet considering the time delay between the two illuminations and the displacement of the particle, in an area of thousands of elements. With particle PIV it is possible to detect other motion properties, such as vortices and deformation velocities, and to study the details of turbulence. The main features that make the PIV suitable for studying natural convection are:

- **non-intrusive velocity measurement.** PIV, contrarily to techniques for the measurement of flow velocity employing probes such as hot wires or pressure tubes, is an optical and, consequence, non-intrusive technique that does not alter the motion of the flow subjected to study.

- **Indirect velocity measurement.** PIV technique (as Laser Doppler Velocimetry for example) measures the velocity of a fluid element indirectly by means of the measurement of the velocity of tracer particles within the flow.

2.1.1 PIV set-up

Experimental measurements were carried out in the laboratory of the Industrial Engineering and Mathematical Sciences Department (DIISM) of the Università Politecnica delle Marche. The test bench in figure 2.1 has been developed to measure the velocity field with 2D PIV system and it is composed of several components that are used for different functions:

- square cavity;
- cavity support and tilting angle mechanism;
- laser;
- CCD camera;
- acquisition system;
- oil nebulizer device;
- two thermostatic baths, a thermal circuit and a temperature control system.

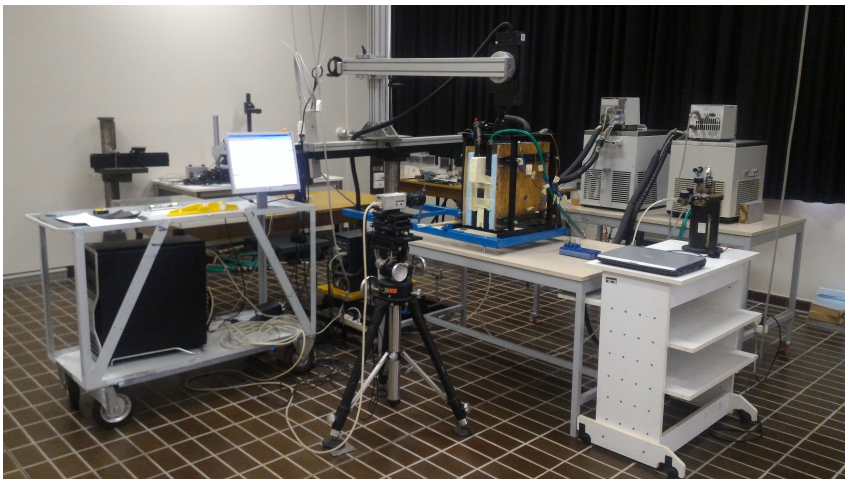

Figure 2.1: Experimental test bench.

The test cell where natural convection of air has been evaluated is a closed box with a square cross-section of height $L = 0.05$ m. The inner space of the cavity is confined to four different volumes. The 0.03 m thick upper and lower surfaces of the enclosure are made of Plexiglas®(PMMA); this material ensures a good agreement between transparency to laser radiation and thermal insulation properties for realizing the cell walls; table 2.1 summarize its characteristics. Since the cavity's length in the longitudinal direction, $s = 0.41$ m is much greater than the transversal length, a 2D model can be used for a cross-sectional area positioned in the middle of the cavity as in figure 2.2. This condition limits the motion along the z-axis that is perpendicular to the laser beam and allows neglecting end effects. The two long vertical walls, that are the "active" walls, are made of aluminum and are the sides of two heat exchangers connected to the thermostatic baths, which maintain the plates at a constant temperature of T_h and T_c. There are also two square vertical walls at the two ends of the cavity: one of them, being on the side where the camera was positioned, was made of glass, while the other one was made of black-painted wood. Also, all the other internal surfaces of the PIV system were painted with a black, low-reflection paint. Only the upper wall was not painted because it is crossed by the 532 nm wavelength laser radiation. The support of the cavity and the tilting angle mechanism are integrated into a single steel structure as in figure 2.3. An open box allows the housing of all the volumes forming the test cell and the rotation is allowed manually through an endless screw.

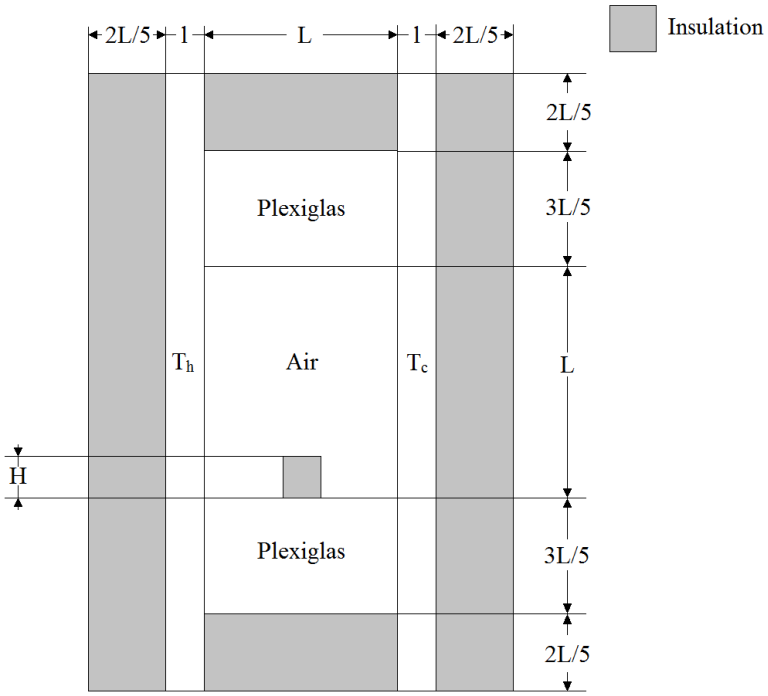

Figure 2.2: Experimental cross-section.

The thermal circuit is composed of two thermostatic baths model Proline RP 1840 and RC20 (see the table 2.2 for more details), manufactured by Lauda Corporation, the two sidewalls and the corresponding connecting pipes. The thermal fluid was a mixture of 75% water and 25% glycol (percentages are on the volumetric basis at 195.16 K). To limit the heat exchange from the fluid to the environment, pipes have been coated with a 0.02 m thick neoprene skin.

Temperature acquisition apparatus is made up of 8 copper-constantan T-type thermocouples connected with a TC-08 data-logger produced by PicoLog Recorder. A Toshiba SM40X-122 PC is used to measure and store the temperatures of the thermocouples obtained by data-logger for the entire duration of each trial. Six thermocouples are used to measure the temperature of the sidewall: three on the black surface of the hot wall and other three on the cold one. The last two thermocouples are used for measuring the environmental temperature in the PIV room. During tests, room temperature is set at 298.16 K and relative humidity is kept at 50% through

Table 2.1: Characteristics of Plexiglas® used for experimental tests and numerical simulations.

Physical characteristics of Plexiglas®		
ρ	1190	kgm^{-3}
c_p	1470	$Jkg^{-1}K^{-1}$
λ	0.157	$Wm^{-1}K^{-1}$

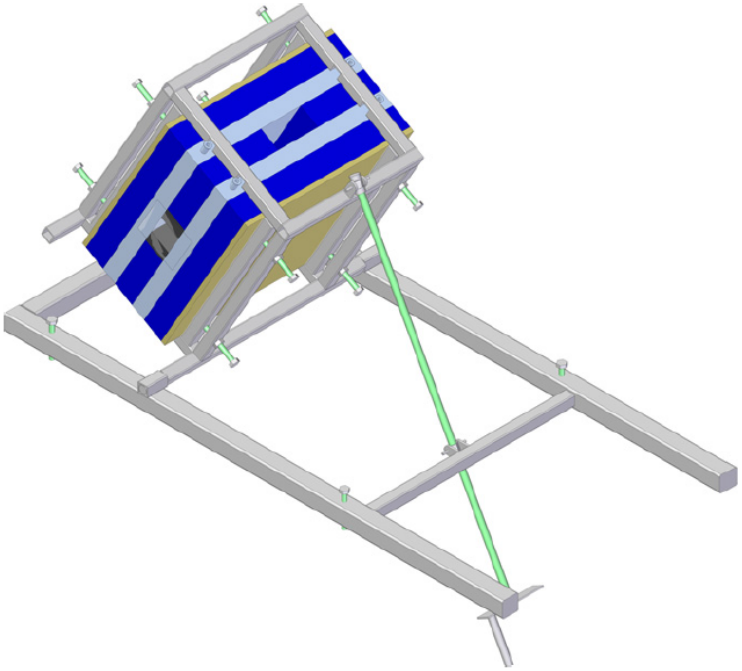

Figure 2.3: Cavity support and tilting angle mechanism.

an air-conditioning system. The temperature of the cold thermostatic bath (T_c) is maintained at 303 K; meanwhile, the temperature (T_h) of the hot wall has been set at different values (308 K, 313 K, 323 K, 333 K and 343 K). Sunflower oil is used as seeding: it is nebulized by a compressed air device, creating particles with a diameter of about 1 μm. The rear part of the top wall of the cavity has been pierced with three holes to facilitate the sprinkle of the oil in the enclosure 2.4.

(a) Front view. **(b)** Rear view.

Figure 2.4: Seeding injection system.

The PIV system used in these experiments consists of a double head Nd:YAG

Table 2.2: Main characteristics of thermostatic baths.

Model		**RP1840**
Manufacturer		Lauda
EMC standard class		B according to EN6126-1
Operating temperature	°C	-40 ÷ 200
Temperature accuracy	°C	0.01
Bath volume	l	18
Model		**RC20**
Manufacturer		Lauda
EMC standard class		-
Operating temperature	°C	-35 ÷ 150
Temperature accuracy	°C	0.05
Bath volume	l	14

pulsed laser light beam Solo II model, manufactured by New Wave Research. It is operated with a double Q-switch trigger; in this way, it was possible to produce a double laser pulse that delivers the energy of 100 mJ per pulse at a wavelength of 532 nm. The main adjustable variables concerning laser firing are the *time between pulses* and the *double pulse frequency*. The time between pulses influences the length of the particles path between the first and the second image recorded and has to be adjusted with the mean velocity in the field. In this work, the time between pulses was set in the range of 5500 ÷ 31900 μs. Double pulse frequency is the inverse of the time between the double pulses sequences. This frequency was always kept equal to 6.1 Hz. Because in the present study streamlines and flow maps are an average of a fixed number of couples of images, this variable also has an important influence. With a frequency of 6.1 Hz, the time for recording 200 couples of images was about 30 s. As will be explained later, for our study only 50 of 200 couples were usually employed. One Hisense MkII C8484–05C model CCD camera manufactured by Hammatsu with 1.3 Mega pixel resolution (1344 x1024) and dynamic range of 12 bit output was used for image capturing. The 50 mm Nikon lens is covered by a filter with a wavelength of 532 nm, in order to record only light from the laser source.

To investigate the effect of the divider presence, height and position, four different baffles have been made in Plexiglas® and covered with black paint; a total of 60 cases were analyzed. The effect of the direction of the gravity vector has been tested for 4 different angles of the cavity ($\theta = 0; \frac{\pi}{6}; \frac{\pi}{3}; \frac{\pi}{2}$) at five different temperature conditions of the hot wall, for a total of 20 cases.

2.1.2 Measurement procedure

Preliminary controls of the cavity sealing and of the environmental conditions were performed before starting each measurement session; then the thermostatic baths were set at the desired temperatures and switched on. When the thermostatic fluids inside each bath reached the target temperature the valves were opened to let the fluid circulate. Through the acquisition system, it was possible to determine the time in which isothermal conditions were reached by the hot and cold walls and then to check the flow to assess its steady state condition.

The achievement and the maintenance during the test of the steady state were very

important because the velocity field in small cavities was highly influenced by even a very low variation of temperature. In our study, acquisitions were performed only when the temperature measured by the thermocouples remained within the ±0.1 K interval for about 1 hour. Moreover, since the oil particles that have to be sprinkled inside the cavity before starting the images acquisition caused a perturbation in the motion of the air inside, it was necessary to wait until the perturbation had disappeared and a new steady state condition was reached. The time required for this perturbation to dissipate was variable and depended mainly on the intensity of convective forces. For high *Ra* values about 20 s after the sprinkling was enough for the PIV system to dissipate the initial perturbation. For very low *Ra* until 30 minutes were necessary to reach steady state conditions.

One of the main parameters that have to be carefully chosen is the time between pulses since it determines the length of the particles path between the first and the second recorded image, and it has to be adjusted with the mean velocity in the field. In fact, if this parameter is not correct the time between two different frames is either too short or too long to allow the correct displacement of each particle to be recorded. Consequently, it is impossible to evaluate the velocity field of the flow analyzed. Table 2.3 shows the time between pulses used in this work for each run; in particular, smaller time intervals were used for faster fields and larger ones in slower velocity fields. In a recent work [45], Corvaro *et al.* pointed out that while considering non-intrusive PIV technique, laser power and acquisition time affected the measurement by causing localized heating of the surfaces (upper and lower) to be stricken by the laser. To reduce this effect, in our study the chosen frequency was 6.1 Hz and in a relative time record of about 30 s, 200 couples of images were acquired. Moreover, no preview mode was used for ten minutes before the acquisition.

Table 2.3: Time between pulses values used for each experimental test. Rayleigh number is the ideal value calculated through equation 2.2.

Position	**Ra**	**Time [μs]**			
		($A_p = 4/5$)	($A_p = 3/5$)	($A_p = 2/5$)	($A_p = 1/5$)
Position 1	6.2×10^4	19400	21900	22600	21800
	1.2×10^5	13600	15500	16900	15800
	2.2×10^5	9600	10900	12600	12000
	3.1×10^5	7800	8700	10400	10200
	3.8×10^5	6700	7350	9000	9150
Position 2	6.2×10^4	18600	20000	22600	31900
	1.2×10^5	12600	12850	13000	19650
	2.2×10^5	8800	8700	8200	13000
	3.1×10^5	7250	7050	6500	10500
	3.8×10^5	6300	6100	5500	9150
Position 3	6.2×10^4	17450	17400	16950	22150
	1.2×10^5	12200	12100	11200	15900
	2.2×10^5	8650	8550	7800	11950
	3.1×10^5	7000	7050	6450	10050
	3.8×10^5	6100	6200	5700	8850

The repeatability of the experiment is a relevant indicator of the quality of measurements. For each case, the same test was repeated with the same initial boundary

conditions; additionally, 200 image couples were acquired every 10 min in 1 hour and a created database was used to evaluate the magnitude of the average and maximum velocity. Table 2.4 shows for each case the standard deviation σ of repeated measurements; standard deviation was calculated for the maximum and average value of the velocity field.

Table 2.4: Standard deviation of repeated measurements for each case study.

		$(A_p = 4/5)$		$(A_p = 3/5)$		$(A_p = 2/5)$		$(A_p = 1/5)$	
Position	**Ra**	V_{max}	V_{ave}	V_{max}	V_{ave}	V_{max}	V_{ave}	V_{max}	V_{ave}
Position 1	6.2×10^4	3.0	1.5	2.7	0.9	3.8	2.2	1.1	1.6
	1.2×10^5	0.2	0.4	0.6	0.6	1.5	0.8	3.8	1.1
	2.2×10^5	0.8	0.1	0.4	0.3	0.6	0.3	0.6	0.7
	3.1×10^5	0.6	0.4	2.8	0.5	0.2	0.3	0.4	0.1
	3.8×10^5	0.4	0.2	0.8	0.5	0.3	0.2	0.1	0.1
Position 2	6.2×10^4	0.4	0.2	3.8	1.5	4.9	2.0	6.5	1.0
	1.2×10^5	0.5	0.3	0.9	0.4	1.0	0.3	0.8	0.2
	2.2×10^5	0.9	0.8	0.5	0.4	1.0	0.3	0.7	0.6
	3.1×10^5	0.6	0.9	0.9	0.4	0.5	0.2	0.5	0.3
	3.8×10^5	1.0	0.6	0.9	0.5	0.8	0.5	0.8	0.3
Position 3	6.2×10^4	0.9	0.6	1.8	2.2	1.4	0.9	6.3	6.6
	1.2×10^5	0.2	0.2	0.4	0.4	1.0	0.5	0.8	0.8
	2.2×10^5	0.4	0.2	0.9	0.7	0.8	0.9	0.9	0.3
	3.1×10^5	0.6	0.5	0.8	0.3	0.6	0.9	0.8	0.4
	3.8×10^5	0.4	0.8	0.9	0.4	0.3	0.6	0.7	0.3

2.1.3 Data analysis

A wide number of acquired images was processed to obtain velocity maps. The size of the images was 1344x1024 pixels with an interrogation area of 32x32 pixels. Images were masked to analyze only the area within the cavity where the seeding is present. Signals were processed by using an adaptive cross-correlation function provided in the Dantec Dynamic software of the PIV system, and also a moving-average validation method was used to accept or reject vectors from the cross-correlation process. A 50% overlap of the areas was used both in the horizontal and vertical directions. The algorithms used for post-processing are described in order to their application. Enhanced information about the used algorithm can be found in Dantec Dynamics user's guide [58].

- **Image arithmetic:** this method enables arithmetic on pixel values. Addition, subtraction, multiplication and division operations can be executed between two set of images. In our case, an image of the empty cavity was acquired before the entering of the seeding and subtracted to the 200 images performing the measurement. In this way, it is possible to eliminate the reflections on the edges of the cavity and on the surfaces of the obstacle. Figure 2.5 shows an example of the output file.

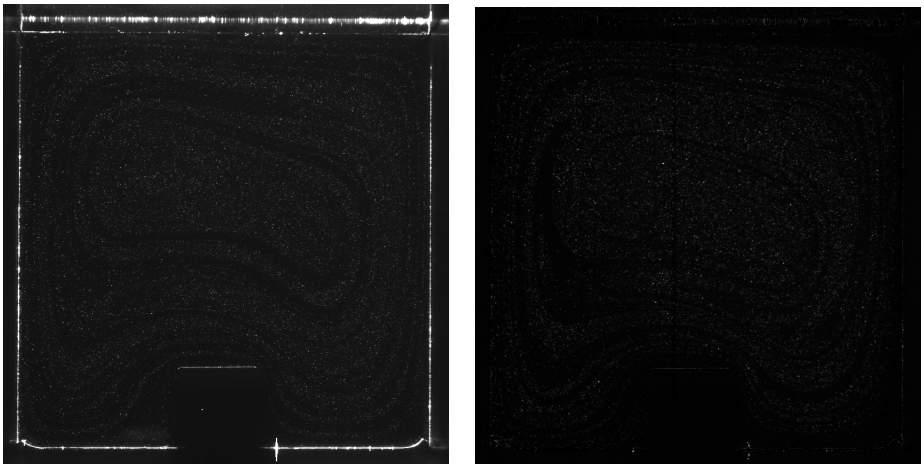

(a) Single image acquires through PIV run.

(b) Image obtained applying the image arithmetic method.

Figure 2.5: Experimental images.

- **Define mask and image masking:** the size of the image is 1344x1024 pixel but the enclosure covers an area of about 800x800 pixel when the CCD camera is positioned at a distance of 0.5 m from the test cell. To elaborate only the interesting area within the cavity a mask was applied. The mask can be composed of three types of shapes (rectangles, polygons and ellipses) and the shape location and size can be specified. Figure 2.6 shows the five rectangular shapes that were used to cover the surfaces outside the enclosure and the baffle, only the area interested by the seeding is processed through following algorithms as in figure 2.6.

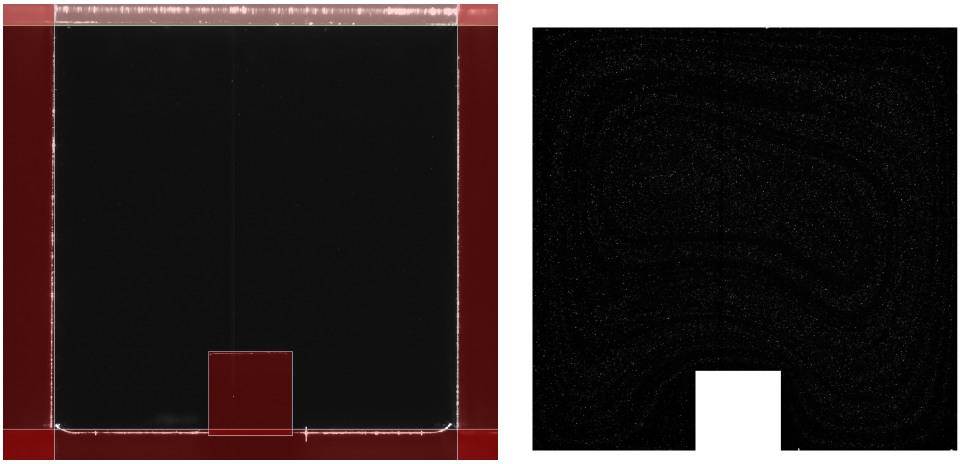

(a) Mask definition.

(b) Output image obtained appling the image masking method.

Figure 2.6: Processed images.

- **Adaptive cross-correlation:** the adaptive correlation method calculates velocity vectors with an initial interrogation area (IA) of the size N time the size of the final IA and uses the intermediary results as information for the next IA of smaller size until the final IA size is reached. In our study three refinement steps were performed; the starting interrogation area was 128x128 pixel until to an IA of 32x32 pixel. To compensate the loss of vector field resolution during the processing, an overlap of 50% IA was used both in horizontal and vertical directions. A moving-average validation method was used to accept or reject vectors from the cross-correlation process. Based on this validation method, individual vectors are compared to the local vectors in the neighborhood vector area. If a vector differs too much in intensity from its neighbors, it is removed and replaced by a vector, which is calculated by local interpolation of the vectors present in the surrounding. Velocity vectors are estimated from mean particle displacement inside interrogation areas (IA). Mathematically, $D(\overrightarrow{X}; t_0, t_{+1}) \approx \int_{t_0}^{t_{+1}} u\left[\overrightarrow{X}(t), t\right] \cdot dt$, where D is the displacement and u is the velocity, is the main formula used to calculate velocity vectors. This formula is transformed into an algebraic equation using a Central Difference Scheme. This scheme is equivalent to a three-point symmetric algorithm for the evaluation of $d(\overrightarrow{X})/dt$, with a reference 'point' created at the time t_{+1} (See figure 2.7).

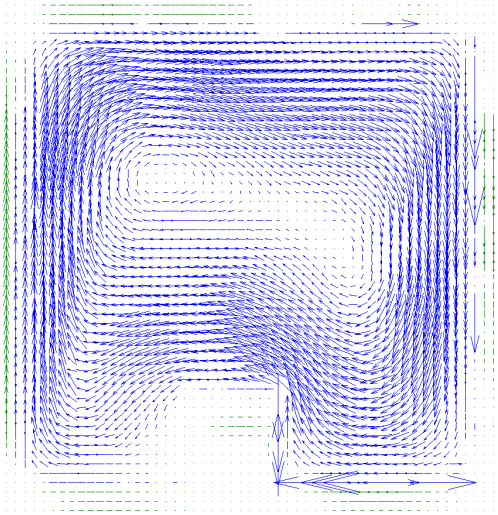

Figure 2.7: Vector velocity map obtained through the application of the adaptive cross-correlation method; green vectors are external to the cavity domain and were not considered during the post-processing.

- **Coherence filter:** feature trackers and cross-correlation may occasionally yield completely wrong velocity vectors. To enhance the result of measurement, coherence-based post-processing is applied to the *raw* velocity field obtained. The coherence filter modifies a velocity vector if it is inconsistent with the dominant surrounding vectors. All vectors within the radius of 30 pixels are used for validation. Figure 2.8 shows an output image.

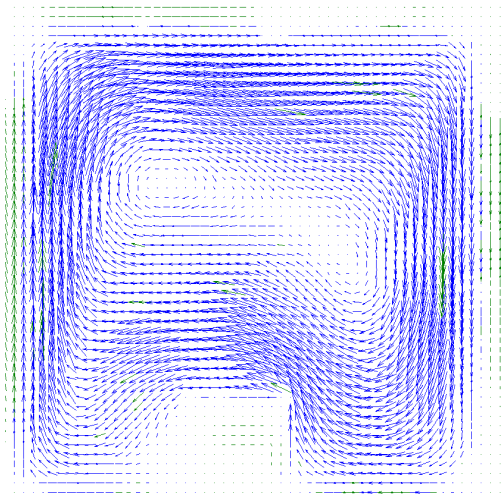

Figure 2.8: Vector velocity map obtained through the application of the coherence filter method. Some green vectors are external to the cavity domain and they are not considered during the post-processing. However, a few number of green vectors is within the cavity and represent the result of the algorithm.

- **Vector statistics:** this method calculates statistics from multiple velocity vector maps. Only the valid vectors included in an interrogation area are used to calculate velocity map; bad vectors are discarded. Graphically speaking, results are presented as a vector map of mean velocity vectors as in figure 2.9. A lot of other statistical quantities are calculated as well (position in pixel and mm, horizontal and vertical velocity components displacement, standard deviation and sum of variances, correlation coefficient, number of samples and vector length).

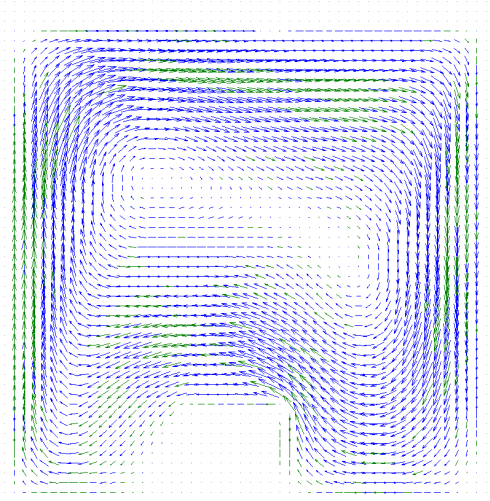

Figure 2.9: Vector velocity map obtained as result of the statistical analysis of 50 image couples.

The result of the post-processing is represented by two velocity maps: scalar map and streamlines (see figure 2.10). Through this two couple of images, a qualitative comparison of experimental and numerical results was possible.

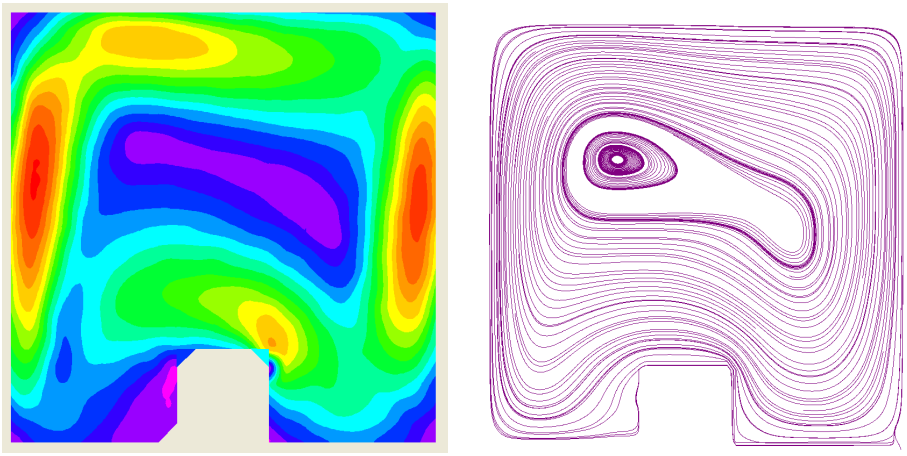

(a) Velocity scalar map. **(b)** Streamlines.

Figure 2.10: Results of the experimental post-processing.

2.1.4 Two-dimensionality of the flow

Previous numerical studies [11, 12] confirmed the supposition of two-dimensionality of the flow. In accordance with those authors, to ensure the absence of end effects, the experimental test was performed at the central plane of the enclosure. However, to experimentally verify the 2D behavior of the flow, the velocity fields were investigated at two other different square cross-sections. Figures 2.11, 2.12 and 2.13 show the velocity profile of the horizontal and vertical components measured in three parallel vertical planes at 1/2 of the cavity height: the measurement central plane and two other planes at a distance of 5 cm to the front and to the back. The cases with an aperture ratio of $A_p = 1/5$ and Ra of 3.8×10^5 were considered for all divider positions. The x-position has been normalized by the cavity width ($L = 0.05$m). The value 0 corresponds to the position of the hot wall and the value 1 coincides with the cold one. The good concordance of the velocity profile can be seen for all cases and confirms the supposition of 2-dimensionality of the flow at the central plane. A small discordance of values is present near the hot wall and at the left side of the baffle when the obstacle is positioned in the middle of the cavity.

2.1.5 PIV measurements convergence

To ensure that stochastic phenomena did not affect the measure of the velocity field, a PIV measurement convergence was performed in two areas of the flow for three different cases. The aperture ratio of $A_p = 1/5$ for all the positions of the baffle was analyzed at Ra of 3.8×10^5 (corresponding at $\Delta T = 40\,^{\circ}$C). Figures 2.14, 2.15 show the variation of the average velocity in two specific positions when adding a further image for the calculation of the velocity field. In figure 2.16 the maximum value of velocity within the cavity was plotted. The x-axis represents accumulated PIV

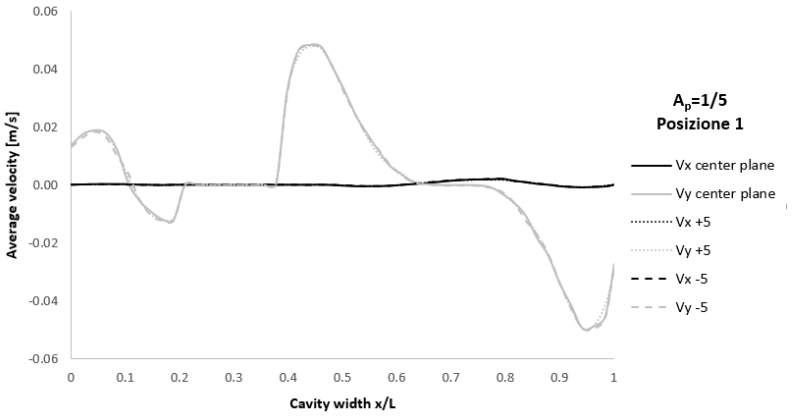

Figure 2.11: Average velocity profile at H/2 for $A_p = 1/5$, $p = 3L/10$ and $Ra = 3.8 \times 10^5$.

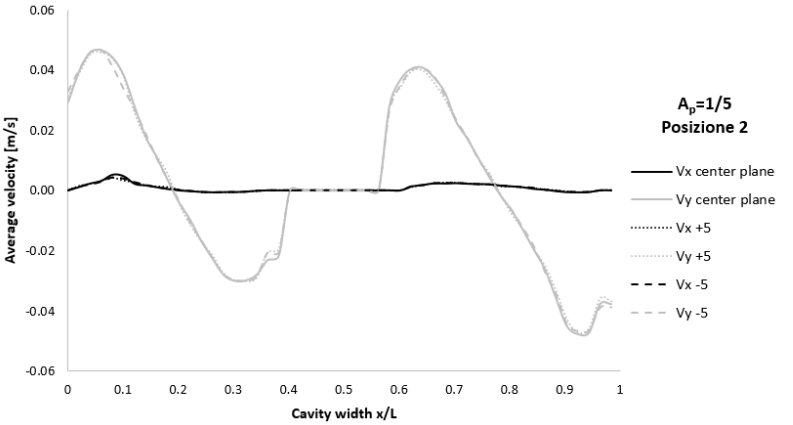

Figure 2.12: Average velocity profile at H/2 for $A_p = 1/5$, $p = L/2$ and $Ra = 3.8 \times 10^5$.

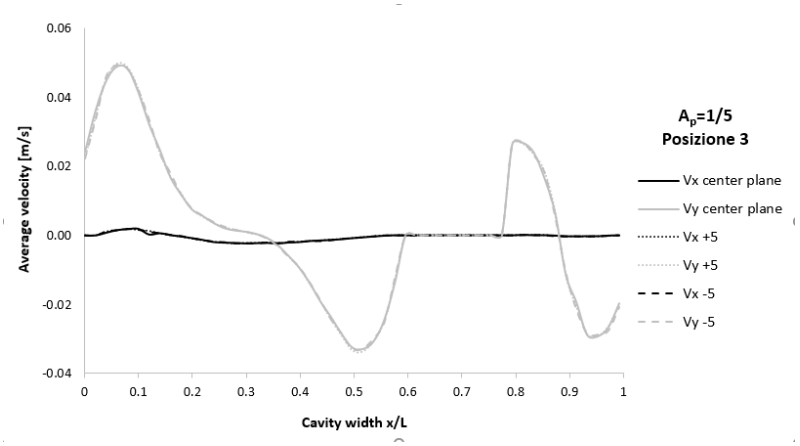

Figure 2.13: Average velocity profile at H/2 for $A_p = 1/5$, $p = 7L/10$ and $Ra = 3.8 \times 10^5$.

snapshot. The coordinates of the interesting areas have been normalized by the cavity height: $x/L = 0$ corresponds to the hot wall while the value 1 coincides with cold ones. $y/L = 0$ locates the lower cavity wall and the value 1 the cavity top. The first position is located in the middle of the cross-section near the hot wall and the second one on the opposite side (next to the cold wall). Results seem to guarantee that 50 images were enough to reach the average velocity convergence during experimental analysis. For the first 20 images, stochastic errors produced very high variable results, especially for the maximum velocity and for the average value near the hot wall.

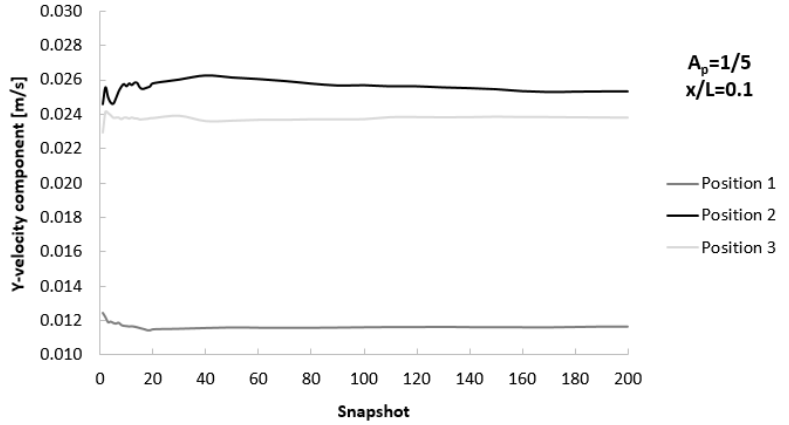

Figure 2.14: PIV realization convergence at H/2 and $x/L = 0.1$ for $A_p = 1/5$ and $Ra = 3.8 \times 10^5$.

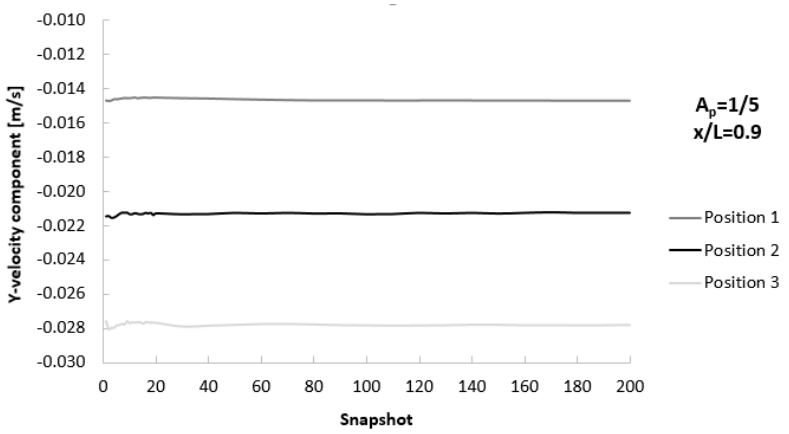

Figure 2.15: PIV realization convergence at H/2 and $x/L = 0.9$ for $A_p = 1/5$ and $Ra = 3.8 \times 10^5$.

2.2 Numerical technique

Natural convection in a square cavity with an inner vertical baffle was numerically studied through a Computational Fluid Dynamic (CFD) software. The governing

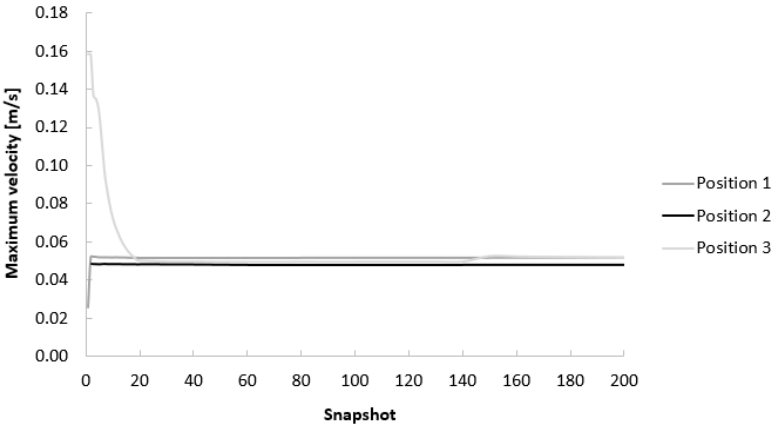

Figure 2.16: PIV realization convergence for $Ra = 3.8 \times 10^5$.

equations for a fluid include the conservation of mass, momentum and energy. These equations are presented in integral or differential (PDE) form to partial derivatives, whose resolution leads to the knowledge of all variables of the problem (velocity field, pressure range, etc.). However, they cannot be solved analytically in most engineering problems, except for a limited number of cases; CFD allows the resolution of such equations in all cases by admitting several approximations, and hence with a known error. By determining the numeric values of interesting variables in discrete spaces of space and time (grid of calculation, or mesh), CFD technique allows substituting partial integrals and derivatives with a set of discrete algebraic expressions, leading to a numerical and non-analytical resolution of the problem.

After the identification of the domain, the followed CFD procedure consists of three steps:

- **Pre-processing**
  1. Geometry
  2. Mesh
  3. Physics
  4. Solver setting
- **Solve**
  1. Compute solution
- **Post-Processing**
  1. Examining results

The reproduction of the geometry of the physical problem, the definition of boundary types and the application of the grid to the interested areas were achieved with Gambit 2.3.16 software. The modeling of the physical problem, the definition of the boundary conditions and all simulations were performed using ANSYS Fluent 12.1.4. Finally, the isotherms with the relative Nusselt number were evaluated and stream functions and velocity maps obtained were compared to the experimental data to validate the numerical results and the adopted model.

The definition and discretization of the physical model (geometry representation and grid generation) is the first step of the process. Usually, for scientific purposes, simple, easily modellable but detailed geometries were used. Then, the problem is transferred from its continuous domain to a discrete representation of the geometry through the application of a mesh or a grid. In the continuous domain, each flow variable is defined at every point in the domain. For instance, the pressure p in the continuous 1D domain shown in the figure below would be given as

$$p = p(x) \qquad 0 < x < 1 \tag{2.1}$$

In the discrete domain, each flow variable is defined only at the grid points. So, in the discrete domain shown in figure 2.17, the pressure would be defined only at the N grid points: $p_i = p(x_i); i = 1, 2, ..., N$.

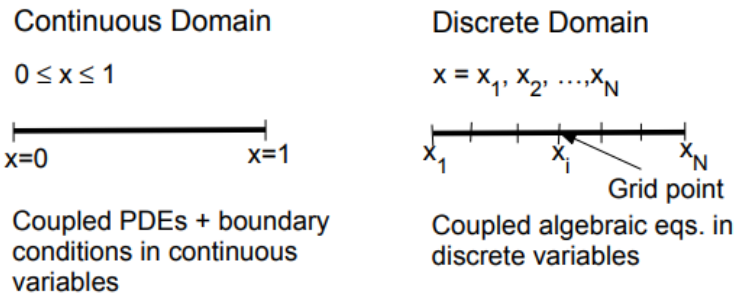

Figure 2.17: Visualization of the differences between continuous and discrete domain.

In a CFD solution, it can be directly solved for the relevant flow variables only at the grid points. The values at other locations are determined by interpolating the values at the grid points. The governing partial differential equations and boundary conditions are defined in terms of the continuous variables. These can be approximated in the discrete domain in terms of the discrete variables. The discrete system is a large set of coupled, algebraic equations in the discrete variables. Setting up the discrete system and solving it (which is a matrix inversion problem) involves a very large number of repetitive (iterative) calculations performed by computers. ANSYS Fluent uses the finite-volume method for discretization, based on the mesh cells. In the finite-volume approach, the integral form of the conservation equations is applied to the control volume defined by a cell to get the discrete equations for the cell. The code directly solves for values of the flow variables at the cell centers; values at other locations are obtained by suitable interpolation.

2.2.1 Geometry and mesh

The physical phenomenon of natural convection in a differentially heated cavity with a vertical baffle was experimentally studied in a parallelepipedal enclosure built with a certain number of external volumes. These volumes have to be considered in the modeling of the physical domain because they took part in the thermal interaction between air and active walls. Some simplifications can be performed:

- as described in Chapter 1, the inner flow was assumed to be 2-dimensional so the considered computational domain was a cross-section of the entire 3D

experimental geometry;

- since the configuration of the experimental cell, in which no axial symmetries have been identified, the entire cross-section of the cavity had to be generated;
- lateral hot and cold volumes were considered at a uniform temperature. To reduce the size of the domain and the computational resources, these volumes were substituted by appropriate thermal boundary conditions.

The areas that have been described are the inner part of the cavity, the upper and lower volumes in Plexiglas®and the obstacle. An example of the computational domain can be seen in figure 2.18.

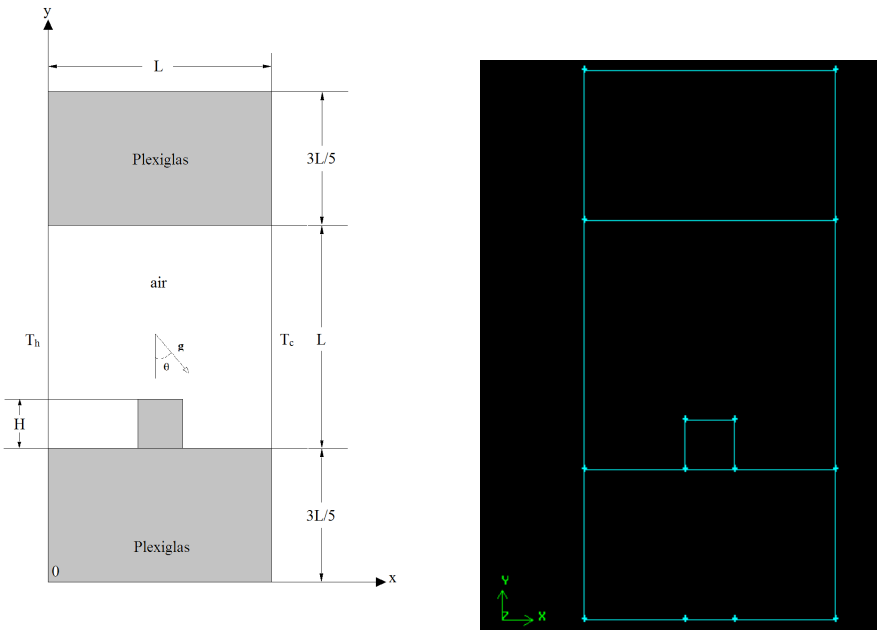

(a) Geometry model for numerical simulation.

(b) Computational geometry used during numerical simulation.

Figure 2.18: Computational geometry.

Once the geometry is completed, a discretization of the computational domain has to be performed. The choice of the mesh has a significant impact on the accuracy and stability of the computation as well as the computational time it takes for the solution to converge. Referring to the work of Paroncini [59] and Acharya and Jetli [17] a quadrilateral structured mesh was built. A fine mesh was chosen to cover the internal area of the cavity, where the solution has to be the most accurate. A sparse mesh covered the external geometry where the solution is less important and imprecise results (within certain limits) were deemed acceptable. Wall boundary type was imposed for all the edges of the geometry. Figure 2.19 shows the cavity with its mesh and relative material types. The influence of the mesh on the numerical results was observed. This study allowed to choose the number of cavity cells to achieve a

good compromise between the accuracy of the results and the computational times that are usually increasing as the number of cells increases.

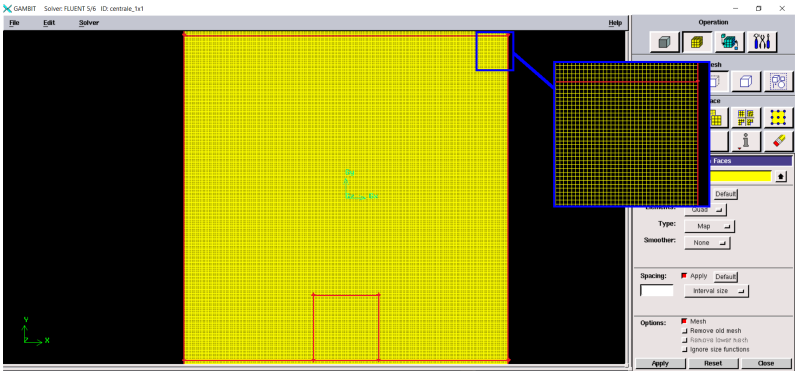

Figure 2.19: Computational grid.

2.2.2 Pure convection model

Once the meshed geometry is completed using Gambit software, it is exported into a file type compatible with the solver so that it may be imported into ANSYS Fluent where the problem is modeled. In order to solve heat transfer problems, the user must activate the relative physical models and supply both the relevant thermal boundary conditions and material properties.

In pure natural convection, the strength of the buoyancy-driven flow is measured by Rayleigh number:

$$Ra = \frac{g\beta\Delta T L^3}{\nu\alpha} \tag{2.2}$$

where g is the modulus of the gravity vector, β is the thermal expansion coefficient, ΔT is the temperature difference between hot and cold walls, L is the characteristic length of the problem domain, ρ is the fluid density, ν represents the dynamic viscosity and α is the thermal diffusivity. All these properties of air have been considered as a function of temperature at atmospheric pressure except for the density. For density description, ANSYS Fluent allows the user to apply the Boussinesq model to heat transfer problems. It ensures a faster convergence if the problem is formulated with fluid density as a function of temperature. This model treats density as a constant value in all solved equations, except for the buoyancy term in the momentum equation:

$$(\rho - \rho_0)g \approx -\rho_0\beta(T - T_0)g \tag{2.3}$$

where ρ_0 is the (constant) density of the flow and T_0 is the operating temperature. The equation above is obtained by applying the Boussinesq approximation $\rho = \rho_0(1 - \beta\Delta T)$ to eliminate ρ from the buoyancy term. This approximation is valid when $\beta(T - T_0) \ll 1$ (changes in density are small). The Boussinesq approximation can be used for the description of this problem because the temperature difference is little (as a consequence also the density variation is limited) and Rayleigh numbers are appreciably low than 10^8. This last condition about Ra indicates a buoyancy-induced laminar flow, with the transition to turbulence occurring over the range of $10^8 < Ra < 10^{10}$.

The governing equations (mass, momentum and energy) for the fluid phase can be written as:

$$\frac{\partial u}{\partial x} + \frac{\partial v}{\partial y} = 0 \tag{2.4}$$

$$u\frac{\partial u}{\partial x} + v\frac{\partial v}{\partial y} = \frac{1}{\rho}\left[\mu\left(\frac{\partial^2 u}{\partial x^2} + \frac{\partial^2 u}{\partial y^2}\right) - \frac{\partial p}{\partial x}\right] \tag{2.5}$$

$$u\frac{\partial u}{\partial x} + v\frac{\partial v}{\partial y} = \frac{1}{\rho}\left[\mu\left(\frac{\partial^2 v}{\partial x^2} + \frac{\partial^2 v}{\partial y^2}\right) - \frac{\partial p}{\partial y} + \rho\beta g(T - T_c)\right] \tag{2.6}$$

$$u\frac{\partial T}{\partial x} + v\frac{\partial T}{\partial y} = \alpha\left(\frac{\partial^2 T}{\partial x^2} + \frac{\partial^2 T}{\partial y^2}\right) \tag{2.7}$$

In the solid, only conduction heat exchange has been considered; the Plexiglas®characteristics (see table 2.1) have been introduced into the software library through an external input file. The temperature of the entire right and left walls were set respectively at $T = T_c$ and $T = T_h$. Since the dimension of the two Plexiglas®volumes can guarantee an adequate thermal insulation, the heat exchange was enabled on the external Plexiglas®walls. At the solid/fluid interface between the inner part of the cavity (air) and the solid volumes (upper and lower walls and baffle edges), Fluent automatically generates a "shadow" zone so that each side of the wall is a distinct wall zone with a distinct material. Here, a coupled boundary condition was set and no additional thermal boundary conditions are required because the solver will calculate heat transfer directly from the solution in the adjacent cells. Summarizing, the thermal boundary conditions can be written as:

$$\begin{aligned}\mathbf{u}\left(0, \frac{3L}{5} \le y \le \frac{8L}{5}\right) = \mathbf{u}\left(L, \frac{3L}{5} \le y \le \frac{8L}{5}\right) = \mathbf{u}\left(0 \le x \le p - \frac{d}{2}, \frac{3L}{5}\right) = \\ = \mathbf{u}\left(p - \frac{d}{2}, \frac{3L}{5} \le y \le \frac{3L}{5} + h\right) = \mathbf{u}\left(p - \frac{d}{2} \le x \le p + \frac{d}{2}, \frac{3L}{5} + h\right) = \\ = \mathbf{u}\left(p + \frac{d}{2}, \frac{3L}{5} \le y \le \frac{3L}{5} + h\right) = \mathbf{u}\left(p + \frac{d}{2} \le x \le L, \frac{3L}{5}\right) = \mathbf{u}\left(x, \frac{8L}{5}\right) = 0\end{aligned} \tag{2.8}$$

$$\nabla T(x, 0) = \nabla T\left(x, \frac{11L}{5}\right) = 0 \tag{2.9}$$

$$T(0, y) = T_h \tag{2.10}$$

$$T(L, y) = T_c \tag{2.11}$$

where the system reference and coordinates are in accordance with the figure 2.18.

Numerical results were obtained through pressure based segregate solvers. It was originally designed for incompressible and mildly compressible flow. The pressure-based solver uses a solution algorithm where the governing equations are solved sequentially. Because the governing equations are non-linear and coupled, the solution loop must be carried out iteratively in order to obtain a converged numerical solution. In the segregated algorithm, continuity, momentum and energy equations are solved sequentially segregated from one another and linearized implicitly with respect to the

equation's dependent variable. The segregated algorithm is memory-efficient since the discretized equations need only to be stored in the memory one at a time. However, the solution convergence is relatively slow, as much as the equations are solved in a decoupled manner. Using this solution method, the velocity field is obtained from the momentum equation and the pressure field is determined by solving a pressure equation which is itself obtained by manipulating the continuity and momentum equations in such a way that the velocity field, corrected by the pressure value satisfies continuity. The semi-implicit SIMPLE algorithm was employed for the pressure-velocity coupling. This scheme uses a relation between velocity and pressure corrections to enforce mass conservation and to obtain the pressure field. Three steps are necessary:

1. an approximation of the velocity field is obtained by solving the momentum equation. The pressure gradient term is calculated using the pressure distribution from the previous iteration or an initial guess;

2. the pressure equation is formulated and solved in order to obtain the new pressure distribution;

3. velocities are corrected and a new set of conservative fluxes is calculated.

The spatial discretization scheme applied is the Green-Gauss Cell-Based gradient. These gradients are needed to determine the scalar values at the cell faces, the secondary diffusion terms and the velocity derivatives. In this case, the Green-Gauss theorem is applied to each cell and the face value of the scalar is taken as the arithmetic average of the values of the neighboring cells.

The Body Force Weighted scheme is applied for pressure discretization. This scheme computes the face pressure by assuming that the normal gradient of the difference between pressure and body forces is constant. This works well with problems that involve buoyancy in which the body forces are known a priori in the momentum equations.

With regards to spatial discretization, a second-order upwind scheme is adopted for both the momentum and energy equations. By default, Fluent stores discrete values of the scalar at the cell centers. However, face values are required for the convection terms and must be interpolated from the cell center values. This is accomplished using an upwind scheme. The face value of the scalar is derived from quantities in the cell upstream, or "upwind", relative to the direction of the normal velocity. The Second Order scheme is chosen as the flow does not go always in one direction and this scheme offers a more accurate solution in such cases.

Under-relaxation factors are employed in numerical computing to stabilize numerical schemes involving iterative procedures. They are used to improve convergence of such numeric schemes, however, they come at the penalty of increasing time taken to the solution of the desired accuracy. The under-relaxation factors have no effect on the solution, though they will influence the number of iterations (and hence time) used to converge to the desired level of accuracy.

At the end of each solver iteration, the residual sum for each of the conserved variables is computed and stored. On a computer with infinite precision, these residuals will go to zero as the solution converges. On an actual computer, the solution has converged when all the residuals' values are lower than the residual monitor value. For single-precision computations (the default for workstations and most computers), residuals can drop as many as six orders of magnitude before hitting round-off. Double-precision residuals, used in the described simulations, can drop up to twelve orders of

magnitude. The applied convergence criteria are 10^{-6} for the continuity and momentum equations and 10^{-12} for the energy equation. Steady-state simulations were carried out for all cases.

Simulations started with the fluid at a uniform and constant temperature that is the average temperature of the hot and cold walls; in this way, it is possible to avert the formation of an anomalous convective flux before reaching steady conditions.

2.2.3 Combined Convective-radiative model

To evaluate the effect of the radiative heat transfer, simulations with a combined convective-radiative model were performed. Compared to the case with pure convection, a term related to radiation is added to the second member of the energy equation:

$$u\frac{\partial T}{\partial x} + v\frac{\partial T}{\partial y} = \alpha\left(\frac{\partial^2 T}{\partial x^2} + \frac{\partial^2 T}{\partial y^2}\right) - \frac{1}{\rho c_p}\nabla \cdot q_r \tag{2.12}$$

The local divergence of the radiative flux ($\nabla \cdot q_r$) in the energy equation is related to the local intensities by:

$$\nabla \cdot q_r = \kappa\left(4\pi I_b(r) - \int_{4\pi} I(r,\Omega)d\Omega\right) \tag{2.13}$$

To obtain the radiation intensity field and $\nabla \cdot q_r$ it is necessary to solve the Radiative Transfer Equation (RTE). This equation for an absorbing, emitting, and scattering medium at position $\mathbf{r}$ in the direction $\mathbf{s}$ is:

$$\frac{dI(\mathbf{r},\mathbf{s})}{ds} + (a+\sigma_s)I(\mathbf{r},\mathbf{s}) = an^2\frac{\sigma T^4}{\pi} + \frac{\sigma_s}{4\pi}\int_{4\pi} I(\mathbf{r}\cdot\mathbf{s}')\Phi(\mathbf{s},\mathbf{s}')d\Omega' \tag{2.14}$$

It is important to note that the RTE has to be solved in a 3D domain whereas the flow field is solved in 2-dimensional coordinates.

Of the five different radiation models available in ANSYS Fluent [60] the Discrete Ordinates (DO) model is the only that can deal with radiation problems with both semi-transparent walls and participating and non-participating media. Moreover, the DO radiation model can also be used to solve radiative heat transfer problems involving both grey and non-grey surfaces. Computational cost is moderate for typical angular discretizations and memory requirements are modest.

DO radiation model solves a finite number of radiative transport equations given by the amount of discrete defined solid angles. These solid angles, based on a control angles discretization, are used to discretize each octant of the angular space at any spatial location. In the two-dimensional calculation, four octants are discretized in $N_\theta \times N_\phi$ solid angles based on the polar (θ) and azimuthal (ϕ) angles respectively, making a total of $4N_\theta N_\phi$ directions altogether. These angles are measured with respect to the global Cartesian system (x, y, z).

Although this model can take into consideration the participating medium, air is considered as transparent in the present study. The Plexiglas® upper walls are assumed semi-transparent while all other surfaces have the following properties: grey diffuse. The emissivity of various walls is shown in table 2.5. The initial condition are the same of the pure natural convection case, $u = v = 0$, $p = 0$ and $T = T_{ave}$. For the velocity field within the cavity, the no-slip boundary condition is assumed. For the energy equation, the left wall is at T_h, the right wall is at T_c and the upper and lower surfaces of Plexiglas® have the adiabatic condition.

Table 2.5: Emissivity of cavity walls used in the combined convective-radiative numerical model.

Wall	Emissivity
Black painted walls	0.94
Top wall	0.86

Several numerical simulations with different angular discretization were performed in order to ensure that the number of solid angle subdivision did not influence the simulation results.

2.2.4 Data analysis

For numerical simulation, when the system of the described equation was solved, both the velocity and thermal fields were completely known. Streamlines and velocity and temperature maps were extracted; the complete definition of the thermal field within the cavity allows the calculation of Nusselt number to investigate the performances of the studied configuration.

The convective, radiative and overall Nusselt number at the hot wall was calculated from the heat fluxes as:

$$Nu_c = \frac{q_c L}{\lambda \Delta T} \tag{2.15}$$

$$Nu_r = \frac{q_r L}{\lambda \Delta T} \tag{2.16}$$

$$Nu_{ove} = Nu_c + Nu_h \tag{2.17}$$

The average Nusselt number ($\overline{Nu}$) on the wall is the line averaged value of Nu.

2.2.5 Numerical accuracy

A non-uniform structured mesh with $2.4 \cdot 10^5$ quadrilateral elements was developed with GAMBIT to describe the geometry of the cavity. A final grid size of 400×400 grid points was chosen for this study. Since the solution needs to be most accurate within the cavity, here the mesh is uniform and dense while a sparse mesh covers the Plexiglas®volumes. To study the effect of the grid size on the solution, a case with $A_p = 1/5$, baffle located at $x/L = 1/2$, $\Delta T = 40K$, tilt angle of $\theta = \frac{\pi}{2}$ and pure convection is considered. Table 2.6 shows the average Nusselt number for the left hot wall and maximum and average velocity values inside the cavity for five different meshes. Figures 2.20 and 2.21 representes the trend of these quantities at different mesh sizes. A comparison of solutions reveals that when the grid size is smaller than 400×400, it does not influence the numerical results.

Table 2.6: Mesh independence test results.

Mesh	$\overline{Nu}$ -	V_{max} m/s	V_{ave} m/s
100×100	2.1291	0.0506	0.0227
200×200	2.4312	0.0500	0.0218
300×300	2.4288	0.0499	0.0217
400×400	**2.4278**	**0.0499**	**0.0217**
500×500	2.4272	0.0499	0.0217
600×600	2.4269	0.0499	0.0217

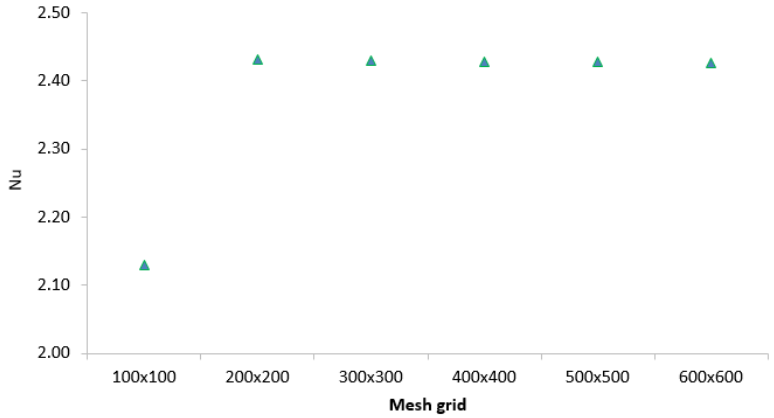

Figure 2.20: Average Nusselt number values by numerical simulation performed for $A_p = 1/5$ and $Ra = 3.8 \times 10^5$ with different grid sizes.

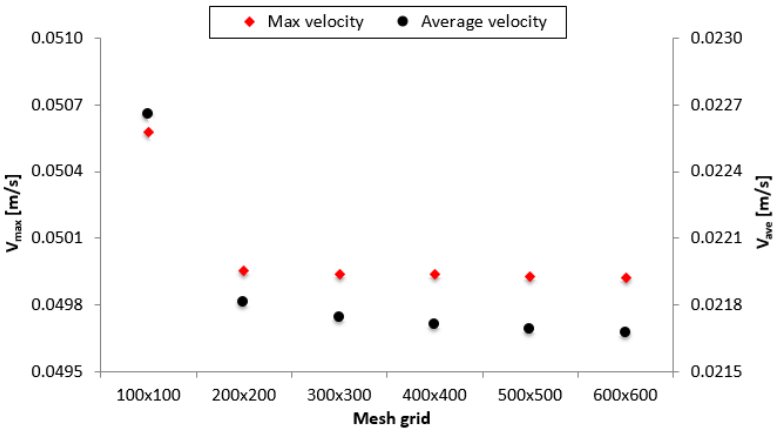

Figure 2.21: Maximum and average velocity values by numerical simulation performed for $A_p = 1/5$ and $Ra = 3.8 \times 10^5$ with different grid sizes.

Chapter 3

Effects of the baffle height and position

Both PIV analysis and numerical simulations were performed for three baffle positions from the hot wall $x/L = 3/10$, $1/2$ and $7/10$ and for a series of enclosure aperture opening ratio varying from $A_p = 4/5$, $3/5$, $2/5$ to $1/5$. Since the baffle was made in Plexiglas®, it ensures a low conductivity of the obstacle; moreover, the baffle thickness was kept at the constant value of $d = L/5$. Scalar velocity maps, streamlines and temperature maps were found for a Rayleigh number range of $6.2 \times 10^4 - 3.83 \times 10^5$.

In this chapter, results are presented in two sections. The first section studied the effect of the aperture ratio on a single centrally located obstacle; results are compared with previous studies. The next section will highlight the effect of the baffle position.

3.1 Effect of the aperture ratio for a central baffle

Numerical scalar temperature and velocity maps and streamline maps are represented in figures 3.1, 3.2 and 3.3. The twenty contour velocity maps with the central baffle are summarized with a unique scale that starts to zero and finishes with the global maximum velocity value for the considered configuration. At the lowest analyzed Rayleigh number, convective flow is relatively weak. The flow pattern and the temperature distribution seem to be symmetrical on both sides of the obstacle and the maximum velocity is reached near the side walls. For $A_p = 4/5$ there is a separation of the flow behind the obstacle; the downward cold stream encounters the divider and, by heating itself, it speeds up. Separation takes place after reaching the top of the baffle. As the Rayleigh number increases, relative velocities increase and the flow pattern significantly changes, in particular between the obstacle and the cold wall. In this region a weak flow can be seen; the colder air tends to stagnate in the lower part of the cavity, between the baffle and the right wall. Thermal profile results stratified and this tendency prevents the penetration of the warmer stream from the left side of the cavity. The higher velocities are visible close to the hot wall that heats the cold fluid flow and allows the air to rise upwards. The separation phenomenon behind the obstruction begins at higher values of aperture ratio ($A_p = 3/5$ from $Ra = 3.1 \times 10^5$).

Experimental results are shown in figures 3.4 and 3.5 and seems to confirm most of the considerations previously made. Qualitatively speaking the fluid flow patterns are similar for both experimental and numerical approaches. The only significative

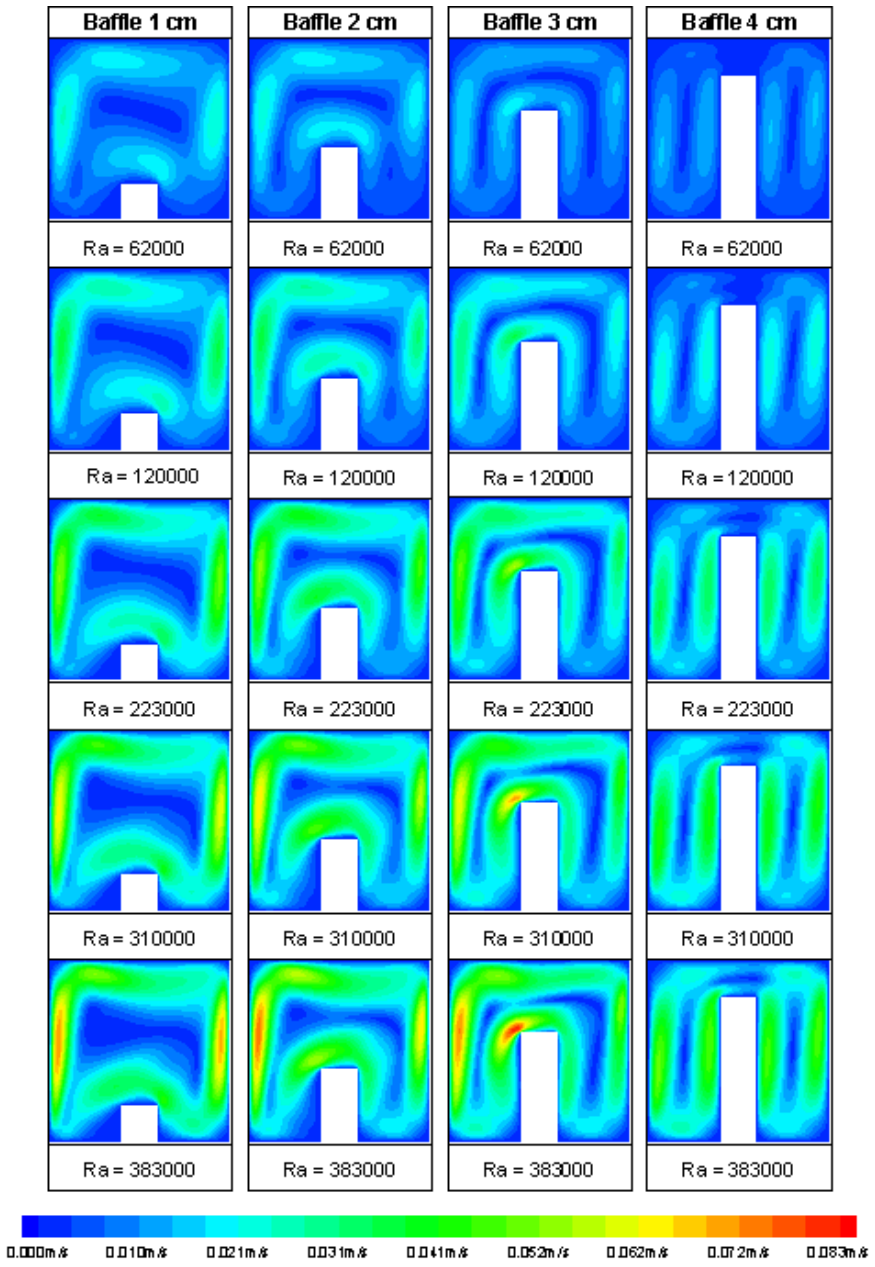

Figure 3.1: Numerical scalar velocity maps for the baffle located at $x/L = 1/2$.

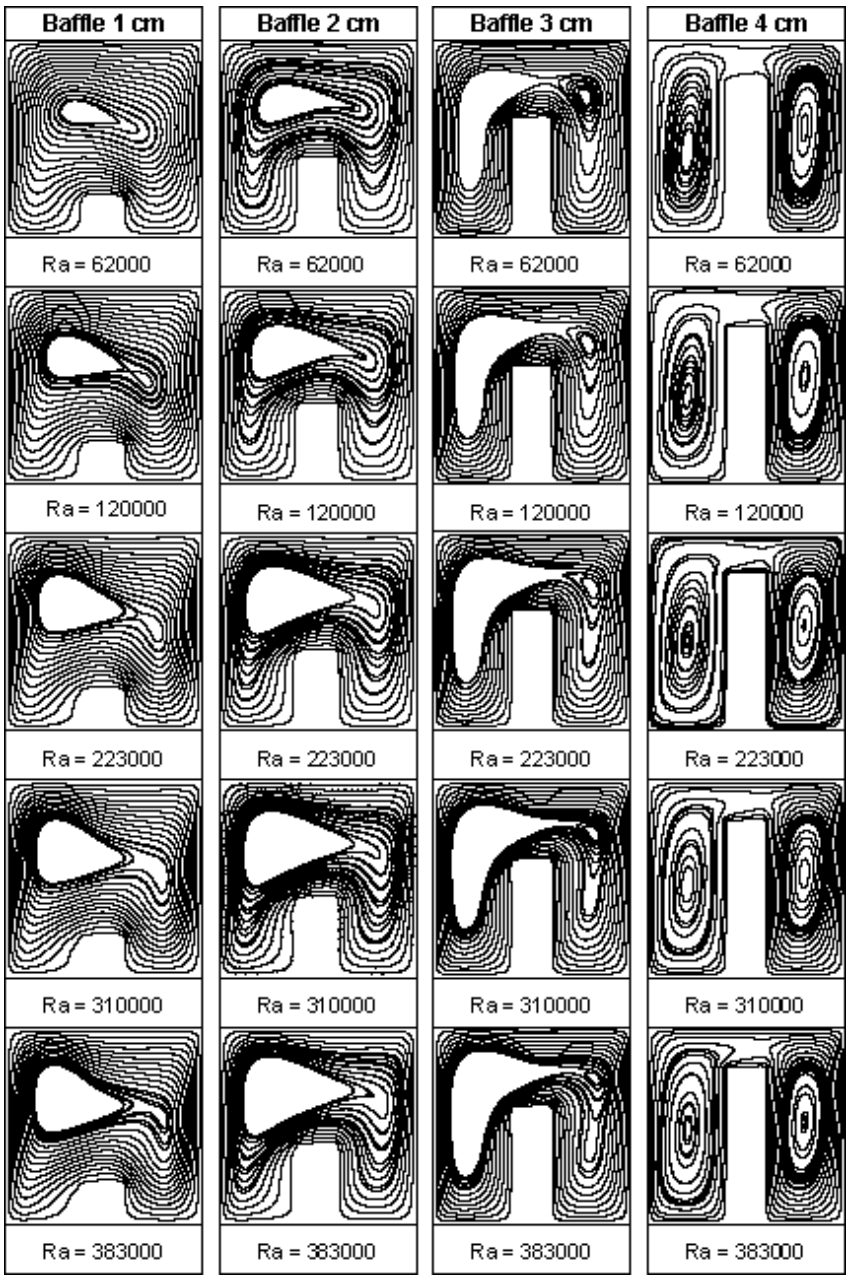

Figure 3.2: Numerical streamlines for the baffle located at $x/L = 1/2$.

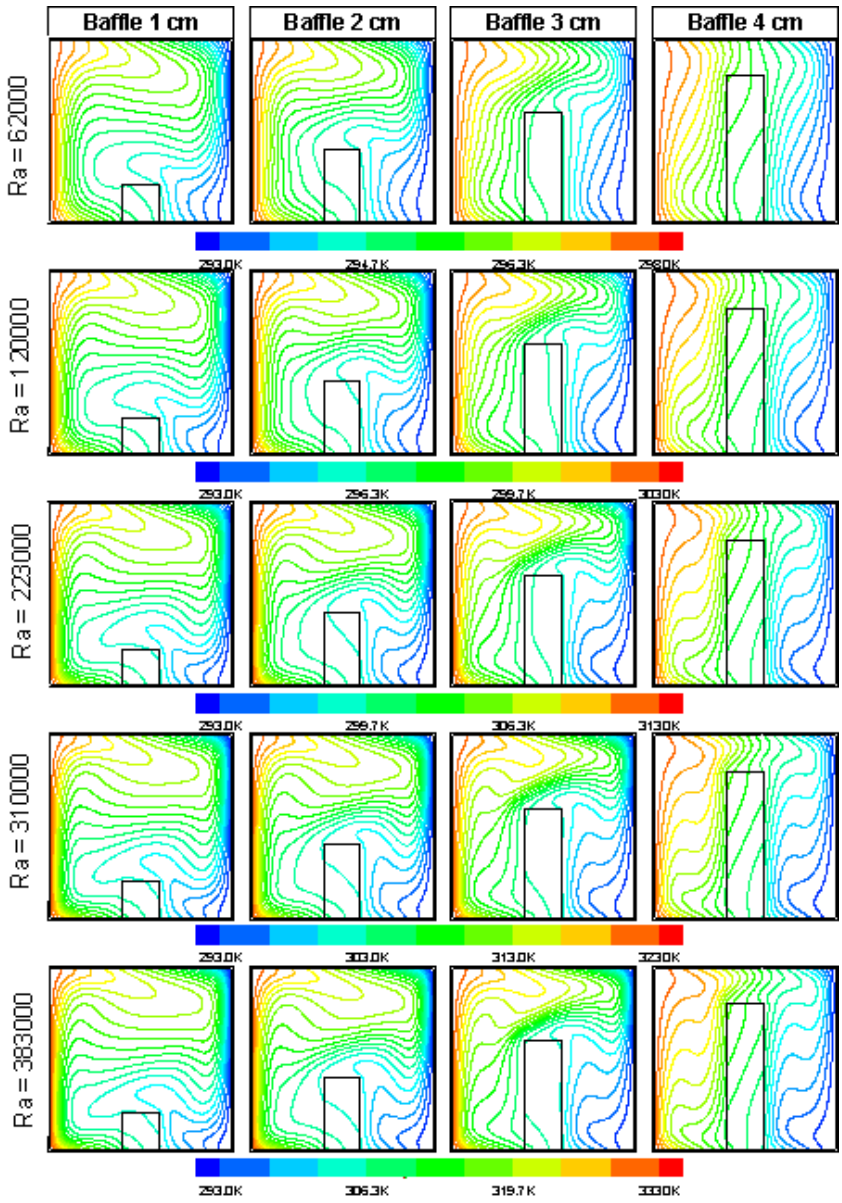

Figure 3.3: Numerical isotherms for the baffle located at $x/L = 1/2$.

Table 3.1: Predicted and measured maximum and average velocities for the baffle located at $x/L = 1/2$. Deviation between experimental and numerical values is calculated.

	Numerical			**Experimental**			**Deviation**		
A_p	Ra	V_{max} m/s	V_{ave} m/s	Ra	V_{max} m/s	V_{ave} m/s	Ra %	V_{max} %	V_{ave} %
1/5	6.25×10^4	0.0143	0.0066	6.33×10^4	0.0151	0.0068	1.32	4.97	1.70
	1.20×10^5	0.0232	0.0104	1.21×10^5	0.0226	0.0104	0.29	-2.60	0.10
	2.23×10^5	0.0350	0.0153	2.22×10^5	0.0338	0.0151	-0.38	-3.66	-1.10
	3.10×10^5	0.0434	0.0189	3.10×10^5	0.0413	0.0186	0.11	-4.95	-1.43
	3.83×10^5	0.0499	0.0217	3.83×10^5	0.0480	0.0211	0.06	-4.09	-2.71
2/5	6.25×10^4	0.0202	0.0079	6.19×10^4	0.0195	0.0079	-0.91	-3.48	-0.65
	1.20×10^5	0.0350	0.0124	1.20×10^5	0.0329	0.0125	-0.38	-6.28	1.32
	2.23×10^5	0.0555	0.0179	2.23×10^5	0.0514	0.0182	0.08	-7.88	1.63
	3.10×10^5	0.0705	0.0217	3.09×10^5	0.0660	0.0219	-0.16	-6.77	1.01
	3.83×10^5	0.0826	0.0248	3.83×10^5	0.0760	0.0246	-0.10	-8.59	-0.72
3/5	6.25×10^4	0.0228	0.0095	6.37×10^4	0.0214	0.0097	1.97	-6.66	2.24
	1.20×10^5	0.0355	0.0135	1.21×10^5	0.0344	0.0140	0.79	-3.44	3.69
	2.23×10^5	0.0525	0.0183	2.23×10^5	0.0500	0.0188	0.25	-5.07	2.20
	3.10×10^5	0.0647	0.0216	3.10×10^5	0.0606	0.0218	0.11	-6.80	0.91
	3.83×10^5	0.0745	0.0240	3.83×10^5	0.0691	0.0239	-0.17	-7.76	-0.39
4/5	6.25×10^4	0.0245	0.0102	6.32×10^4	0.0242	0.0106	1.22	-1.17	4.38
	1.20×10^5	0.0361	0.0135	1.21×10^5	0.0354	0.0139	0.59	-2.10	3.41
	2.23×10^5	0.0517	0.0174	2.24×10^5	0.0506	0.0180	0.46	-2.08	3.00
	3.10×10^5	0.0630	0.0201	3.10×10^5	0.0614	0.0204	0.28	-2.62	1.48
	3.83×10^5	0.0721	0.0221	3.83×10^5	0.0694	0.0223	-0.15	-3.88	0.66

difference can be seen for $A_p = 2/5$ and high Ra number where the numerical model fails to predict the flow separation: in these cases, experimental tests reveal that the flow separates behind the obstacle and then reattaches at the left side of the baffle before it reaches the floor of the cavity.

Table 3.1 presents the maximum and average velocities in the cavity for all cases with central baffle; the displacement between experimental and numerical values is also calculated to validate the numerical model. Results showed a maximum deviation of 8.59% and 4.38% for respectively V_{max} and V_{ave}. Looking at velocity values, some considerations can be made: in all cases velocities increase as Ra increases and the minimum value of velocity is reached when $A_p = 1/5$. For low Rayleigh numbers up to 1.20×10^5, velocities increase as aperture ratio increases while for higher values of Ra this tendency changes: the increase of the aperture ratio causes the reduction of the maximum velocity value. These trends are shown in figures 3.6 and 3.7 where it can be also seen that the increase in the maximum and average velocity is larger for $A_p = 2/5$. An interesting consideration with regard to the position of the maximum velocity within the enclosure: it changes when it moves from the left hot wall ($A_p = 4/5$, $3/5$) to the top of the baffle ($A_p = 2/5$) where a strong thermal stratification is present.

As described in Chapter 1, results of previous works showed different flow regimes for very similar configurations. Natural convection in an enclosure with a single centrally located thin baffle projecting downwards was both experimentally and numerically

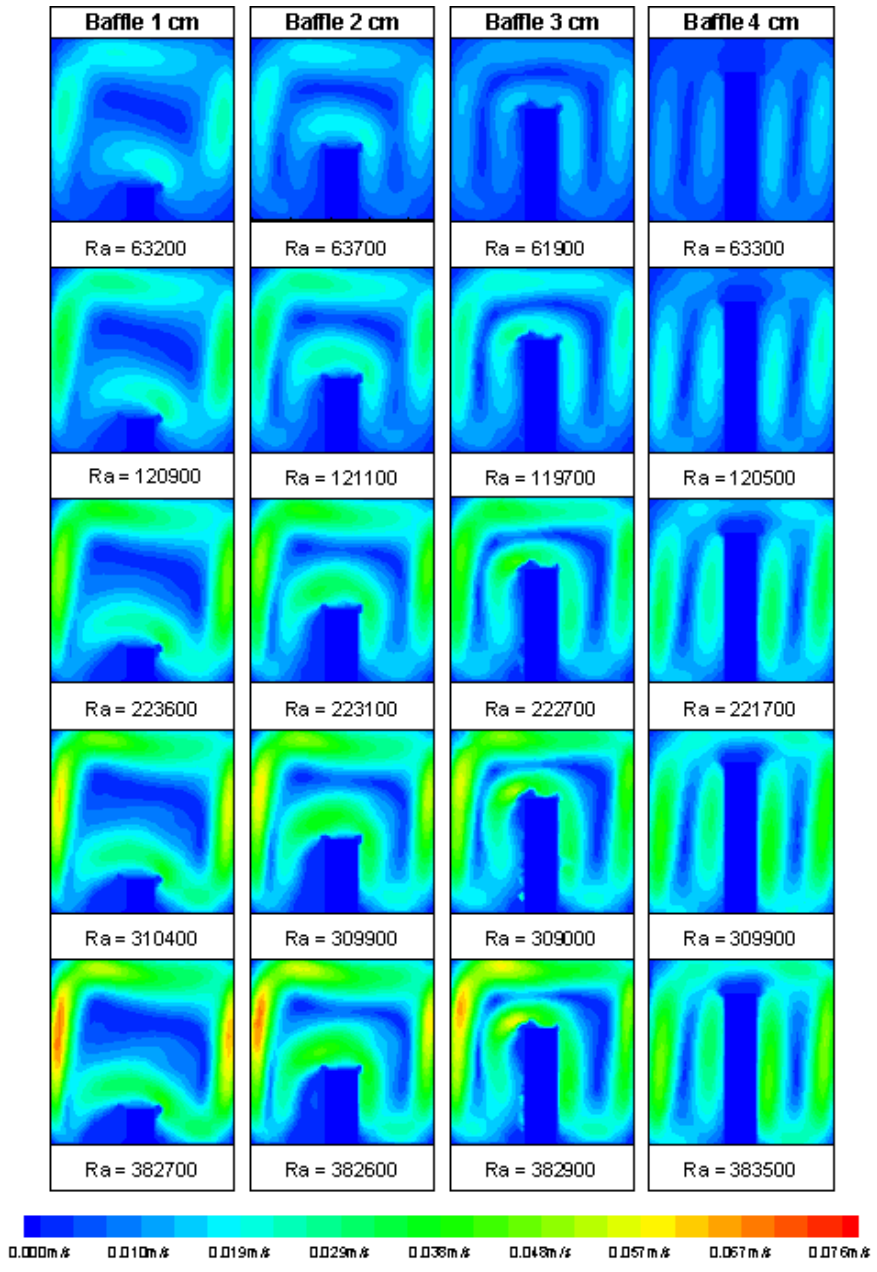

Figure 3.4: Experimental scalar velocity maps for the baffle located at $x/L = 1/2$.

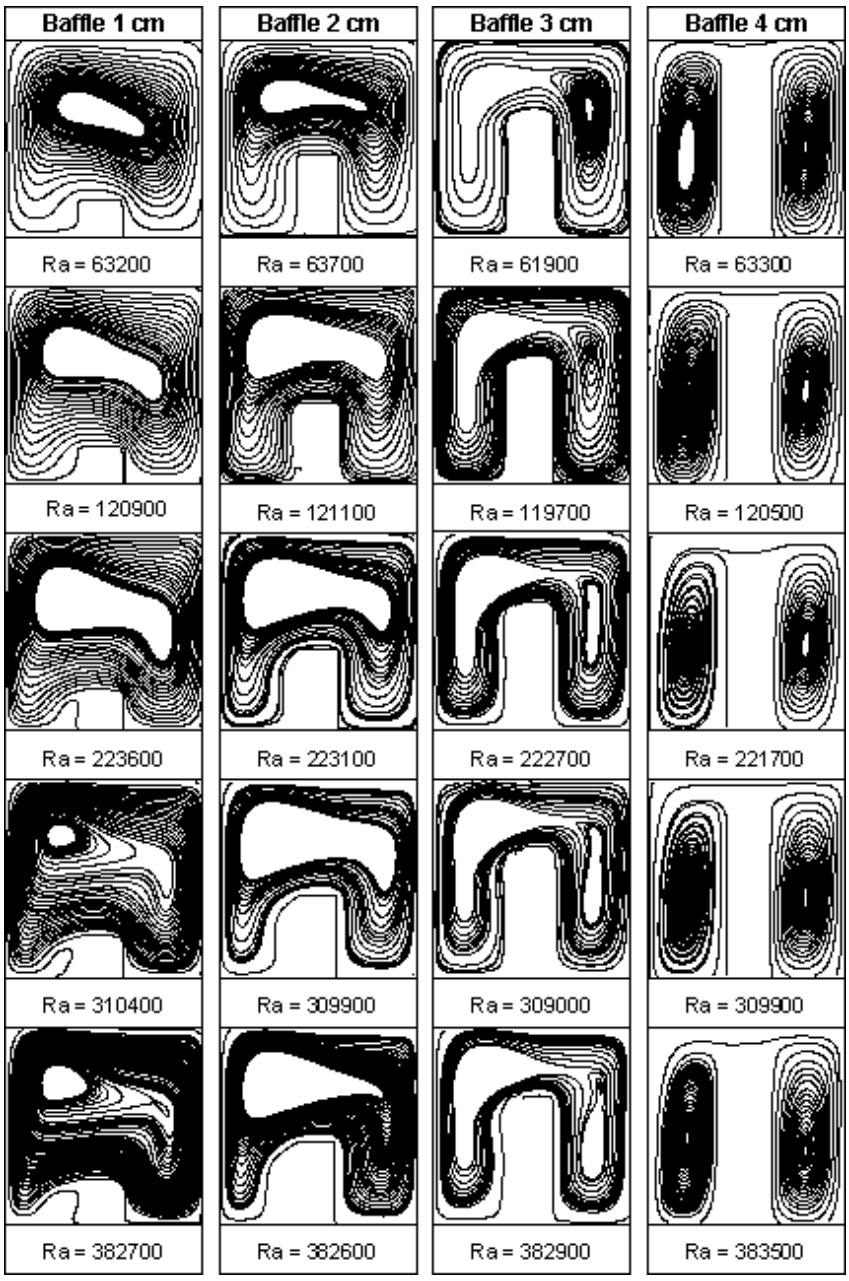

Figure 3.5: Experimental streamlines for the baffle located at $x/L = 1/2$.

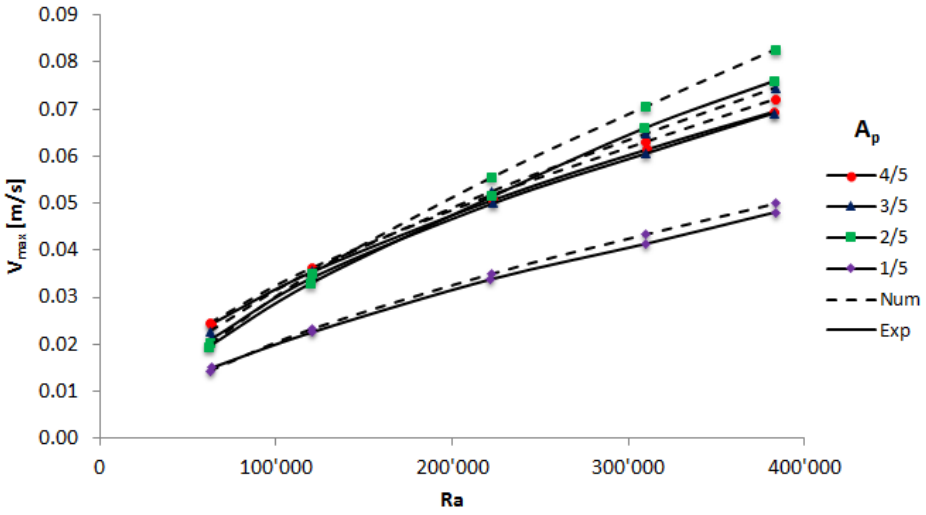

Figure 3.6: Maximum velocity for each case with the baffle located at $x/L = 1/2$.

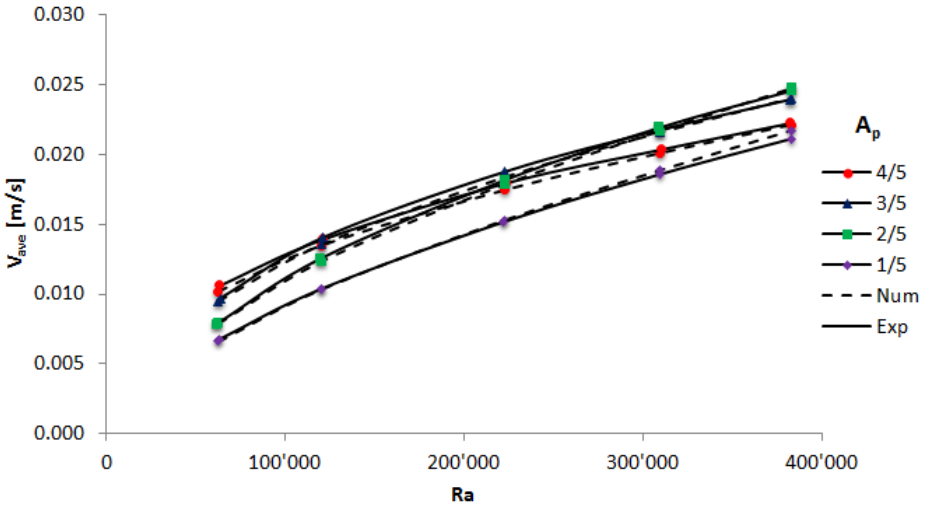

Figure 3.7: Average velocity for each case with the baffle located at $x/L = 1/2$.

investigated by Nansteel and Greif [11, 61] for high Rayleigh numbers ($2.3 \times 10^{10} \leq Ra \leq 1.1 \times 10^{11}$). The researchers also studied the case of upwards obstacle with an $A_p = 1/2$ to compare the two different cases. The obtained results showed a weak flow recirculation between the hot wall and the top of the baffle. Moreover, the flow separation occurred near the cold wall at the same height of the divider. In a successive work, Zimmermann and Acharya [15] numerically studied natural convection in a square enclosure using an obstacle with $A_p = 1/2$ and $d = 1/5$ for $10^4 \leq Ra \leq 3.55 \times 10^5$. Relying on the experimental results of Duxbury [8], researchers observed a little different flow pattern from the one described above with a strong stream along the hot vertical wall, the upper end-wall and the top half of the cold wall. A relatively weak flow was found between the cold wall and the obstacle. Their results also showed the separation of the flow behind the top divider (between the baffle and the hot wall) for the high conductive baffle. Acharia and Jetly [17] investigated the effect of varying the aperture ratios in a water-filled cavity for a Rayleigh number range of $10^4 - 3.55 \times 10^5$. The authors tried to summarize the results obtained by above-mentioned researchers; they showed the existence of three different flow patterns at different Rayleigh number ranges. For $Ra < 10^4$ the velocities are very low and the flow pattern is symmetrical. For medium Rayleigh number, the strong velocities are located near the hot wall and the top of the baffle; so the flow tends to be asymmetric and there is the possibility of separation behind the divider. Finally, at high Ra, recirculation takes place between the cold wall and the baffle while behind the divider the stream remains attached to the rear wall. Results of the present work seem to verify the pattern classification proposed by Acharya and Jetli, however comparing the experimental velocity field for $A_p > 1/2$ with numerical results, a separation zone at the top of the cavity can be found.

As far as thermal exchange is concerned, figure 3.8 shows the local Nusselt number profile along the hot wall for $Ra = 3.8 \times 10^5$ and the three different aperture ratios analyzed. Moreover, Nusselt number profile is reported for the entire range of Ra at $A_p = 3/5$.

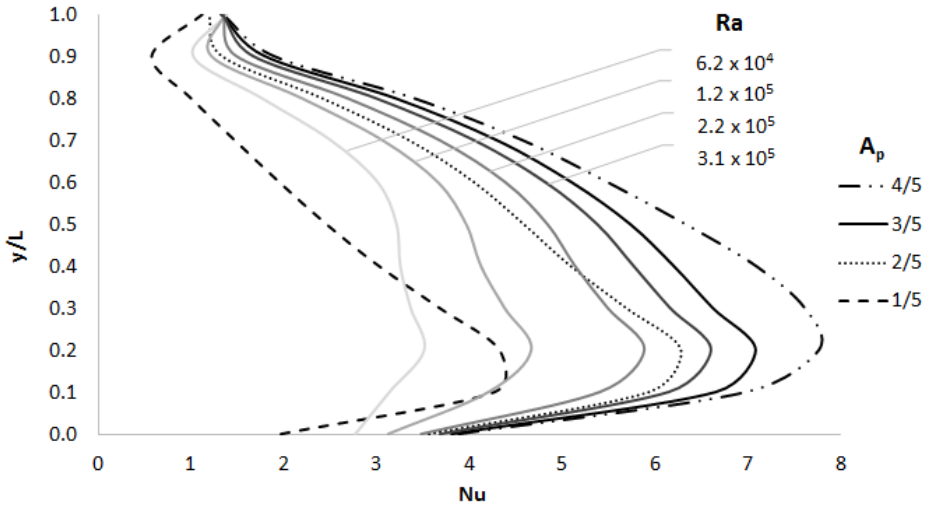

Figure 3.8: Local Nusselt number along with the vertical hot wall for an enclosure with the baffle located at $x/L = 1/2$.

Table 3.2: Average Nusselt number.

x/L	Ra	$A_p = 1$[5]	$A_p = 4/5$	$A_p = 3/5$	$A_p = 2/5$	$A_p = 1/5$
3/10	6.2×10^4	-	2.93	2.46	1.85	1.57
	1.2×10^5	-	3.56	3.02	2.29	1.69
	2.2×10^5	-	4.28	3.65	2.83	1.84
	3.1×10^5	-	4.73	4.06	3.18	1.96
	3.8×10^5	-	5.06	4.37	3.45	2.07
1/2	6.2×10^4	3.69	2.98	2.62	1.92	1.43
	1.2×10^5	4.46	3.67	3.31	2.60	1.72
	2.2×10^5	5.33	4.48	4.08	3.34	2.05
	3.1×10^5	5.87	4.98	4.55	3.78	2.27
	3.8×10^5	6.24	5.34	4.88	4.07	2.43
7/10	6.2×10^4	-	3.06	2.81	2.35	1.88
	1.2×10^5	-	3.72	3.40	2.90	2.16
	2.2×10^5	-	4.48	4.08	3.51	2.47
	3.1×10^5	-	4.96	4.49	3.88	2.67
	3.8×10^5	-	5.29	4.78	4.14	2.82

In each case it can be observed a sharp peak at the lower section of the wall ($0.1 \leq y/L \leq 0.3$) at the point where the warm stream reaches the hot surface while the minimum value of Nu is located in the higher part of the wall. Qualitatively the profile is the same varying the aperture ratio, even though a trend inversion develops at $y/L \approx 0.9$ when $A_p = 1/5$. For the lower value of Ra at $A_p = 3/5$, a second peak can be seen at $y/L \approx 0.6$ in correspondence of the maximum value of velocity. This trend disappears as Ra increases and the second peak is gradually substituted by a flatter profile.

Table 3.2 displays the average Nusselt number ($\overline{Nu}$) for the cavity. In order to analyze the effect of the presence of the baffle, experimental Nusselt number using Bairi [5]

$$\overline{Nu} = 0.15 Ra^{0.29} \tag{3.1}$$

was also given. Bairi experiment was conducted in an open square cavity ($A_p = 1$) for a range of Ra from 10 to 10^{10}. Results highlight that the presence of the obstacle strongly influences the Nusselt number reducing the heat transfer rate across the enclosure. The ratio between the average Nusselt numbers of the partially divided enclosure and ones of the cavity without internal baffle at the same Rayleigh numbers shows a percentage reduction of heat transfer from about 14% at $A_p = 4/5$ to 61% at $A_p = 1/5$ for the higher Ra.

In order to verify the accuracy of these numerical values, we chose to compare the results of this work with previous studies through the correlations produced by researchers (see figure 3.9). Kirkpatrick [14] presented a correlation for natural convection of air in a rectangular cavity with an aspect ratio of $H/L = 1/2$ divided in the center by a baffle. Their correlation is expressed as

$$\overline{Nu} = 0.081 Ra^{0.316} A_p^{0.309} \tag{3.2}$$

and it is valid for $1/8 \leq A_p \leq 3/4$, $0.9 \times 10^4 \leq Ra \leq 0.9 \times 10^9$, $Pr = 0.77$. The

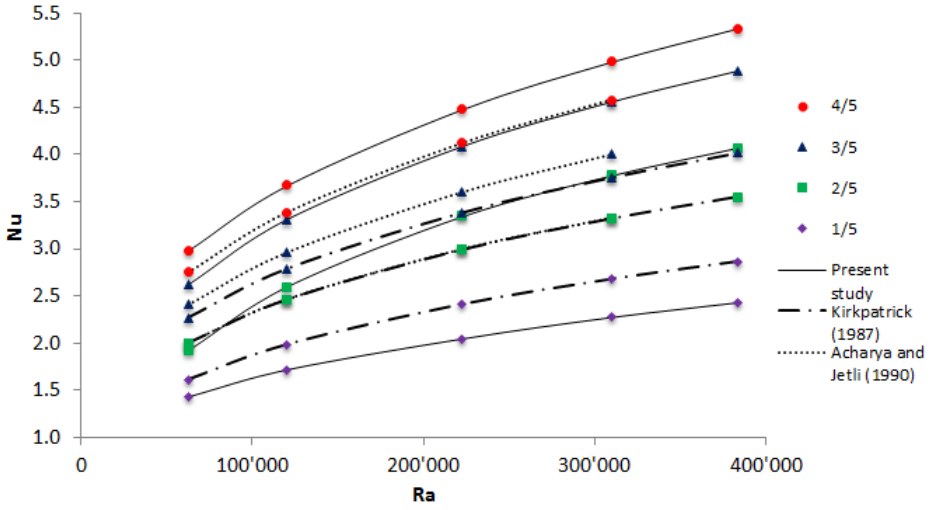

Figure 3.9: Average Nusselt number as a function of the Rayleigh number for a cavity with the baffle located at $x/L = 1/2$. Results are compared with correlations from Kirkpatrick [14] and Acharya and Jetli [17]

validity range of the previous correlation does not allow the comparison for $A_p = 1/5$. For all cases the percentage variation increases as Ra increases. Maximum deviation is 21% at $A_p = 3/5$, 15% at $A_p = 2/5$ and 15% at $A_p = 1/5$; these values are obtained for $Ra = 3.83 \times 10^5$. A good agreement can be seen for low Rayleigh numbers ($Ra \leq 1.20 \times 10^5$) at $A_p = 2/5$.

Acharya and Jetli [17] investigated natural convection in a square cavity with an internal obstacle at various aperture opening ratios. Correlation of the heat transfer results of the centrally located divider case yields the following equation:

$$\overline{Nu} = 0.091 Ra^{0.318} A_p^{0.462} \tag{3.3}$$

for $1/3 \leq A_p \leq 1$, $10^4 \leq Ra \leq 3.55 \times 10^5$ and $Pr = 0.71$. Since the range of validity of this correlation is limited, all the cases of the present study with $A_p = 1/5$ and $Ra = 3.83 \times 10^5$ can not be compared. Results show a good agreement and a reduced percentage variation; the maximum value for each aperture ratio is 9%, 14% and 14%, corresponding to $A_p = 4/5, 3/5$ and $2/5$. In all cases, the average Nusselt number variation increases as Ra increases.

3.2 Effect of the baffle position

Analyzing the left position of the obstacle, a similar temperature profile can be seen for all the investigated Rayleigh numbers and aperture ratio. Between the hot wall and the baffle there is a thermal stratification, clearly visible in figure 3.10, which gradually reduces its height as A_p increases. This thermal stratification impedes the cold stream to penetrate in the interested region descending along the zone behind the obstruction. The air flow that goes back the baffle is driven to the top of the hot wall and only a small part of the flow descends to the bottom of the cavity (see figure 3.11). At the right side of the enclosure a vertical thermally stratification that ensures the

convective flow is present. Since the cavity is strongly obstructed at the lowest value of the aperture ratio, the cold stream tends to create an isolated vortex visible in figure 3.12. At this baffle position, the maximum value of velocity is reached along the side walls for $A_p = 4/5$ and $Ra = 3.8 \times 10^5$. Reducing the aperture ratio, velocities reduce their values and the zone with strong flow moves to the right side of the baffle.

As the divider is moved from the left position $x/L = 3/10$ to the right position $x/L = 7/10$, thermal stratification in the baffle-hot wall region reduces. However, at the right side of the cavity a new thermal stratification takes place between the cold wall and the obstacle as in figure 3.13. This thermal profile blocks the entry of the stream; the air is forced to flow directly around the divider towards the hot wall as can be seen in fugure 3.14. The flow pattern is very similar to the one described in the previous section (streamlines can be observed in figure 3.15) and high velocities are located in the middle of both hot and cold walls and at the left corner of the baffle. For each Ra analyzed, the maximum value of velocity is reached at $A_p = 2/3$ by the stream descending from the top of the obstacle. Differently from the previous configuration (baffle position at $x/L = 3/10$) in which no separation occurred, here the flow separates from the top of the baffle at $A_p = 4/5$ and $3/5$ for all Ra and rejoins the hot wall.

Acharya and Jetli [17] in their works noted a similar flow pattern varying the baffle position. However, for a baffle placed near the cold wall and at high aperture ratio their numerical model was not able to predict flow separation behind the divider. This is probably caused by the different thickness of the used baffle, very thin in Acharya and Jetli's investigation and large in the present study. Also, Nansteel and Greif [11] examined the effect of divider position in a rectangular cavity at $10^{10} \leq Ra \leq 10^{11}$. No qualitative change in the flow was observed by the researchers moving the baffle from the hot wall to the cold ones; the flow pattern remains the same of the configuration with central baffle.

Experimental results shown in figures 3.16, 3.17, 3.18 and 3.19 seem to confirm numerical predictions. Qualitatively speaking, the flow patterns are identical, however, the experimental separation zone behind the baffle is larger than the numerical one for the cases with higher aperture ratio and Rayleigh numbers. The relative values of maximum and average velocity are summarized in table 3.3 and their comparison underlines a good agreement between calculated and measured results. If the agreement is expressed in terms of maximum velocities, the deviation is generally within 10% while in case of the average velocities it is a little smaller and it is within 8%.

A general trend, showed in figures 3.20, 3.21, 3.22 and 3.23, can be seen for velocities at all configurations: they increase as Ra increases. With respect to the cavity with baffle at $x/L = 3/10$, the flow is strongest at $A_p = 4/5$ and gradually reduces its value as the aperture ratio decreases. The trend changes passing to the configuration with the obstacle at $x/L = 7/10$ in which highest velocities can be found at $A_p = 2/5$ and the lower value at $A_p = 1/5$. At the other values of the opening ratio, the intensity of the streams is very similar. Comparing the maximum velocities for the same Ra and A_p (see figure 3.20 and 3.22), the maximum displacement takes place at an aperture ratio of 2/5 and right baffle for the highest Rayleigh number. Moreover, the minimum deviation can be seen in all cases with $A_p = 4/5$.

The distributions of the local Nusselt number along the hot wall for the left and right baffle positions are presented in figures 3.24 and 3.25. All the values of the aperture ratio are shown for a Rayleigh number value of 3.8×10^5. Moreover, for $A_p = 3/5$, the entire field of Ra is plotted. Considering the obstacle located at $x/L = 7/10$, the Nusselt number profile for the showed cases is characterized by a unique peak at

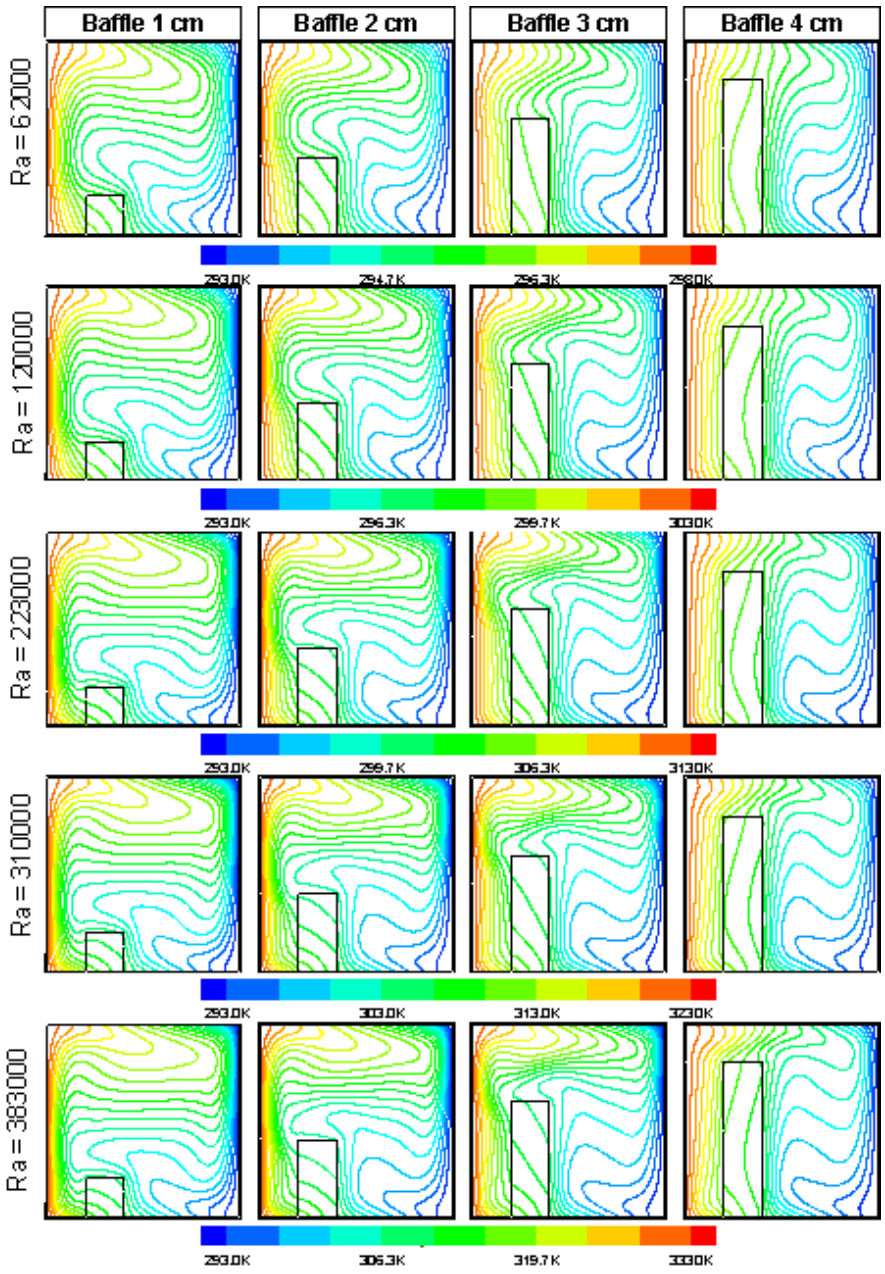

Figure 3.10: Numerical isotherms for the baffle located at $x/L = 3/10$.

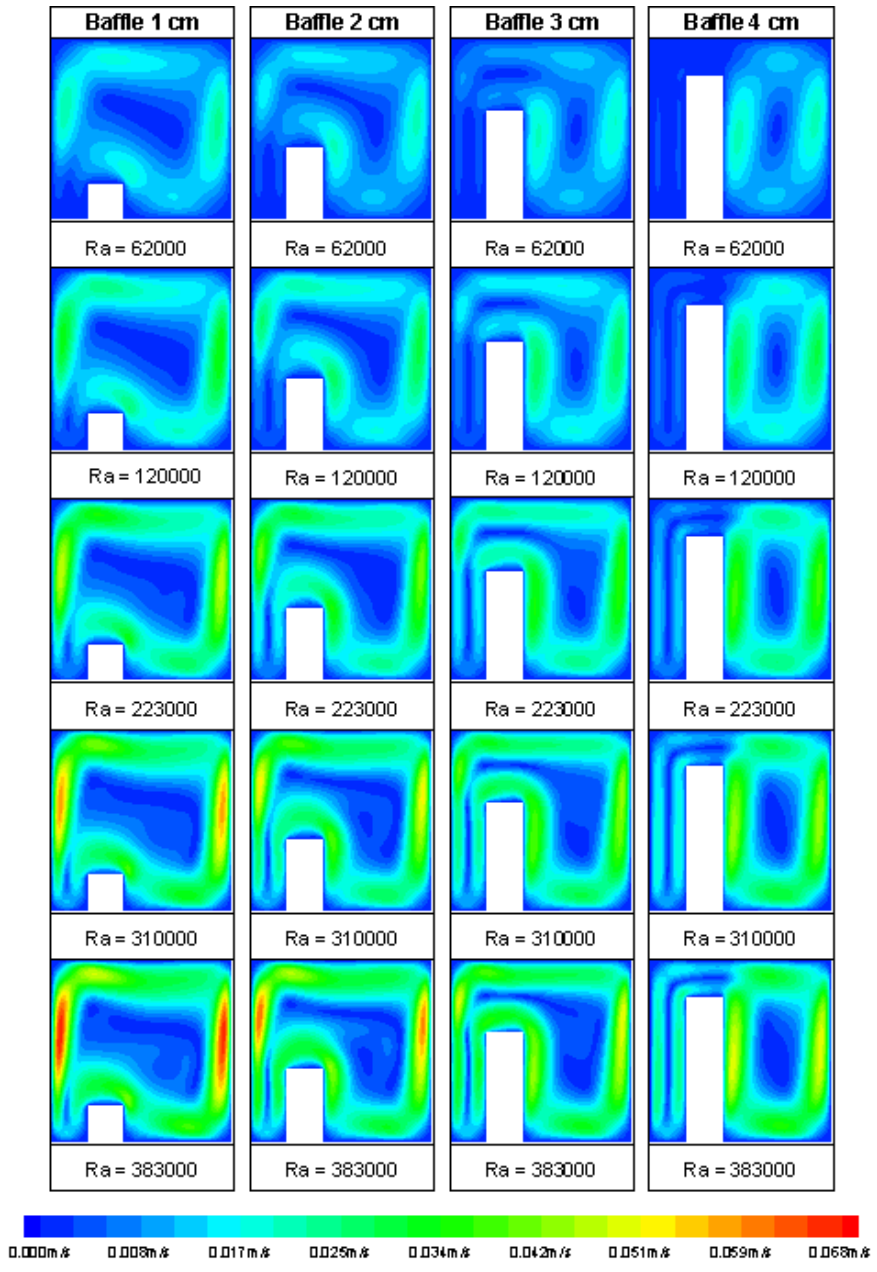

Figure 3.11: Numerical scalar velocity maps for the baffle located at $x/L = 3/10$.

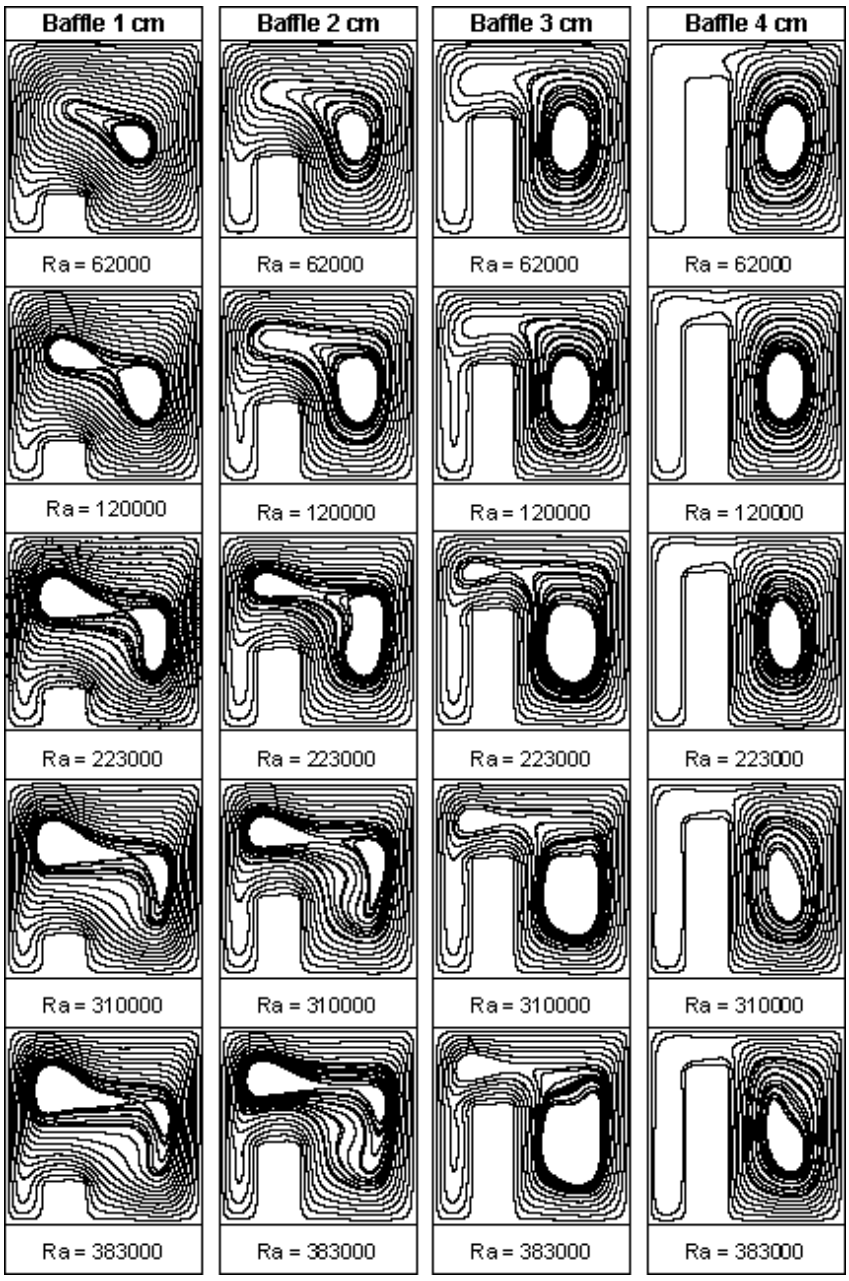

Figure 3.12: Numerical streamlines for the baffle located at $x/L = 3/10$.

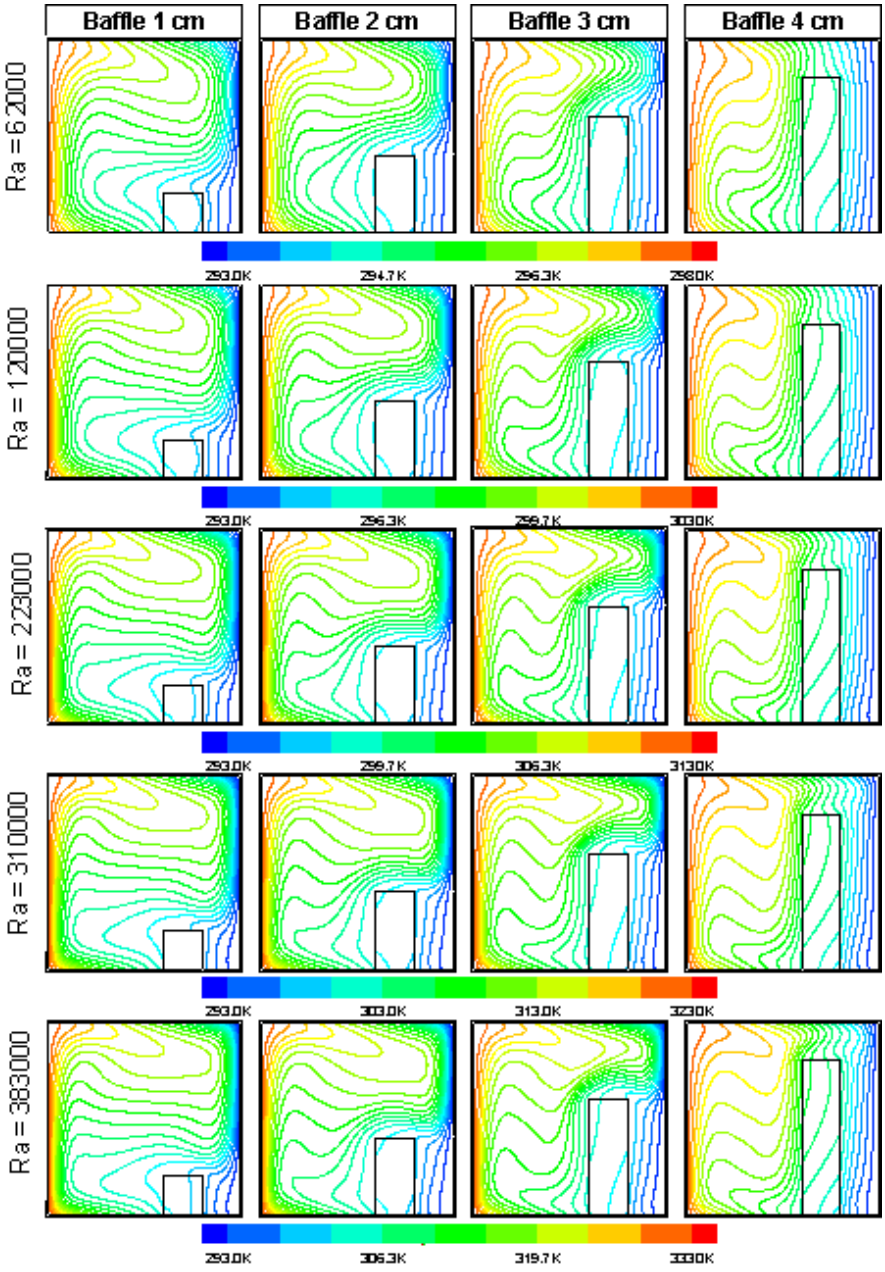

Figure 3.13: Numerical isotherms for the baffle located at $x/L = 7/10$.

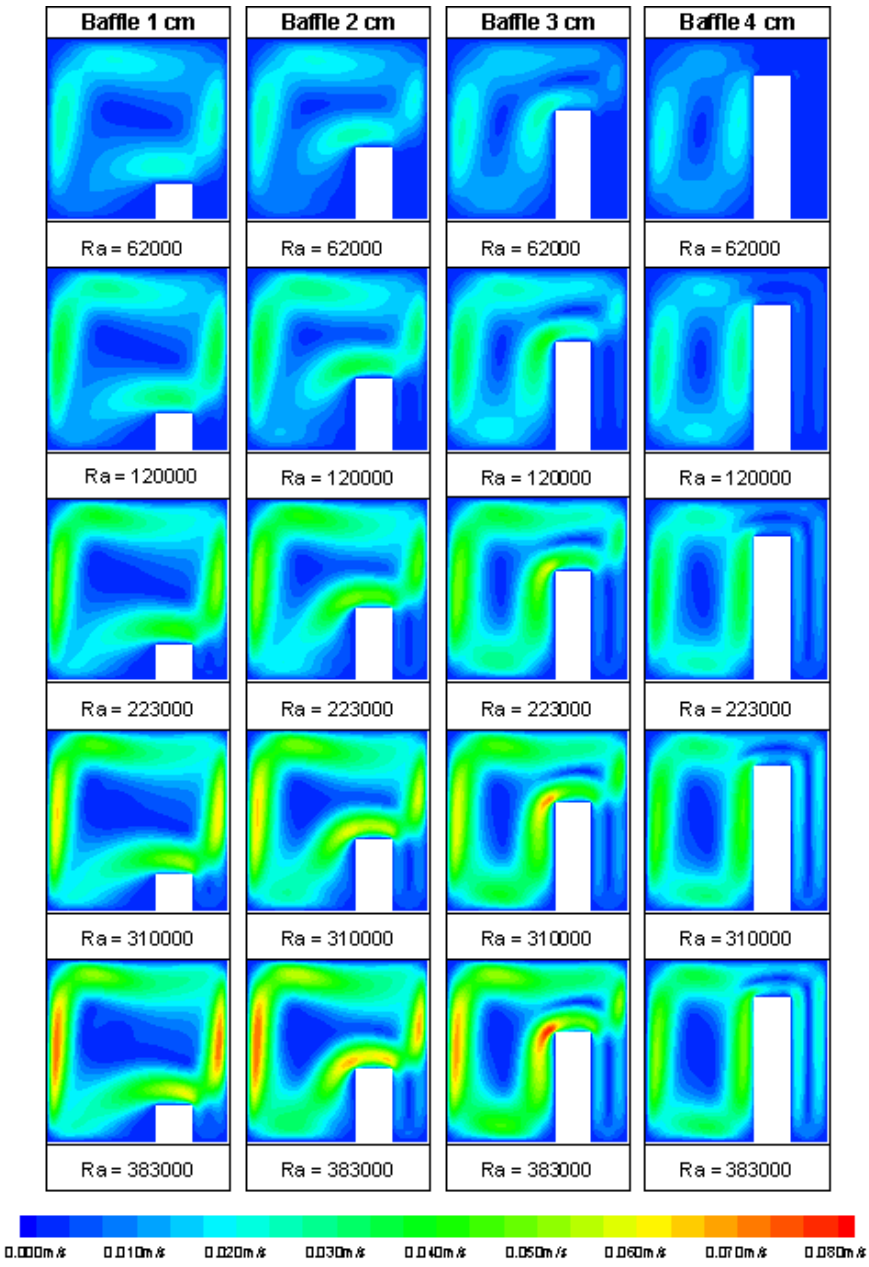

Figure 3.14: Numerical scalar velocity maps for the baffle located at $x/L = 7/10$.

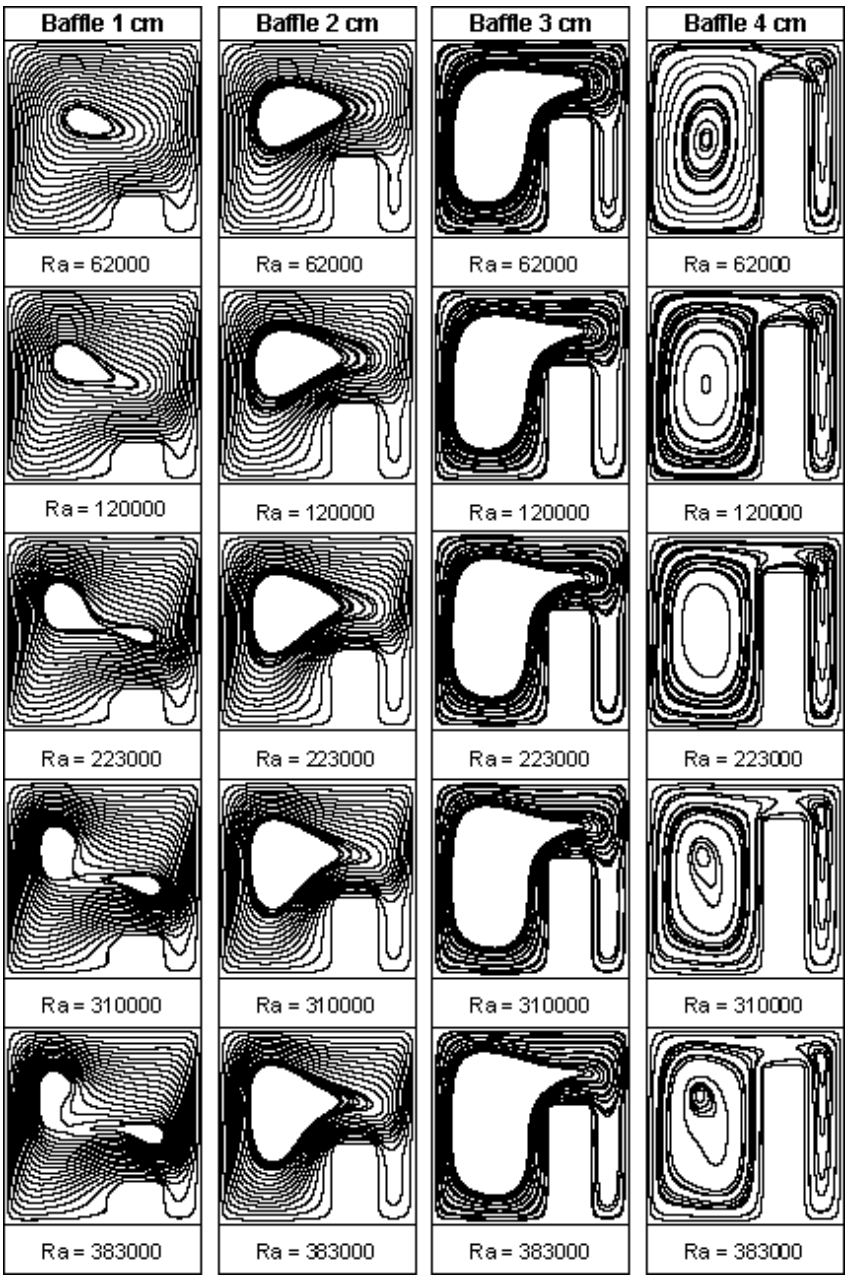

Figure 3.15: Numerical streamlines for the baffle located at $x/L = 7/10$.

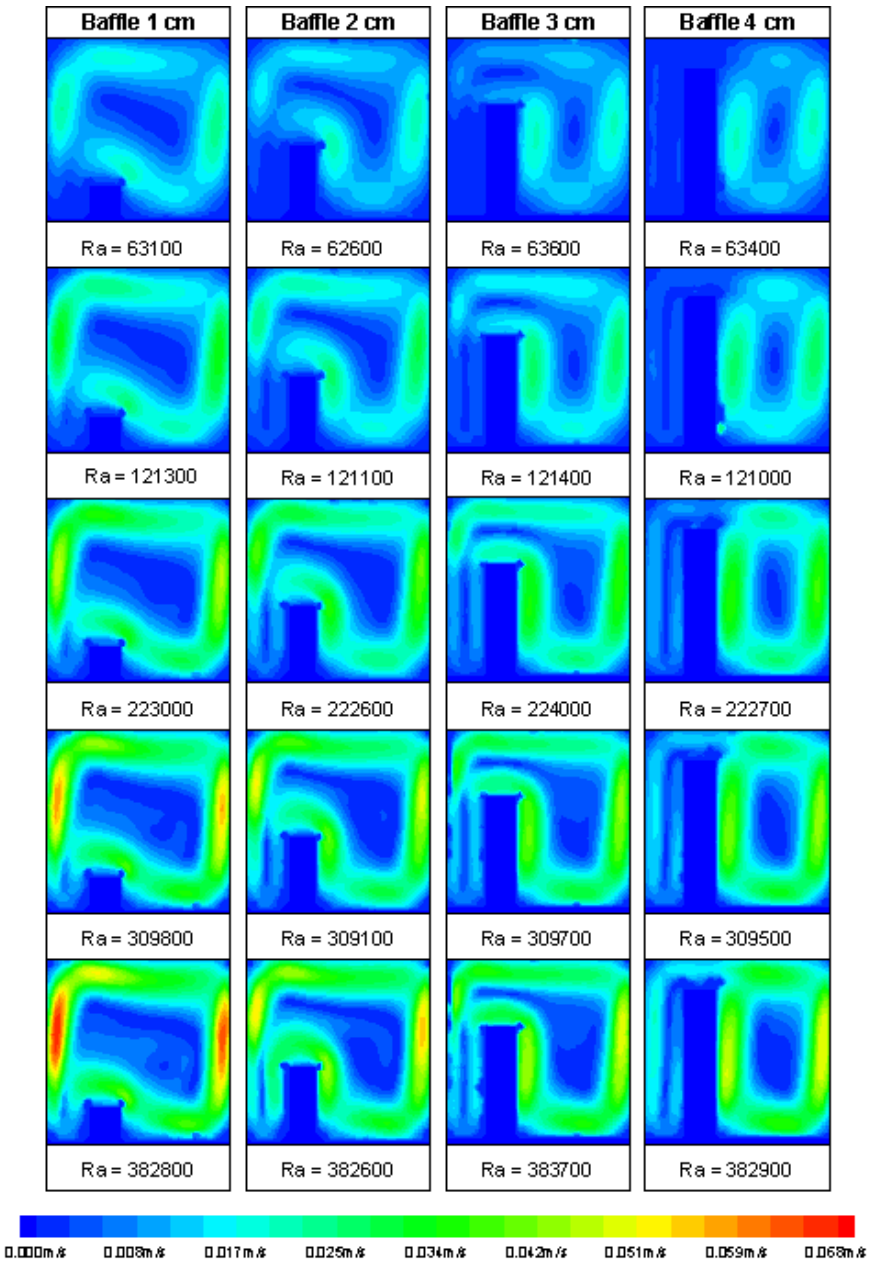

Figure 3.16: Experimental scalar velocity maps for the baffle located at $x/L = 3/10$.

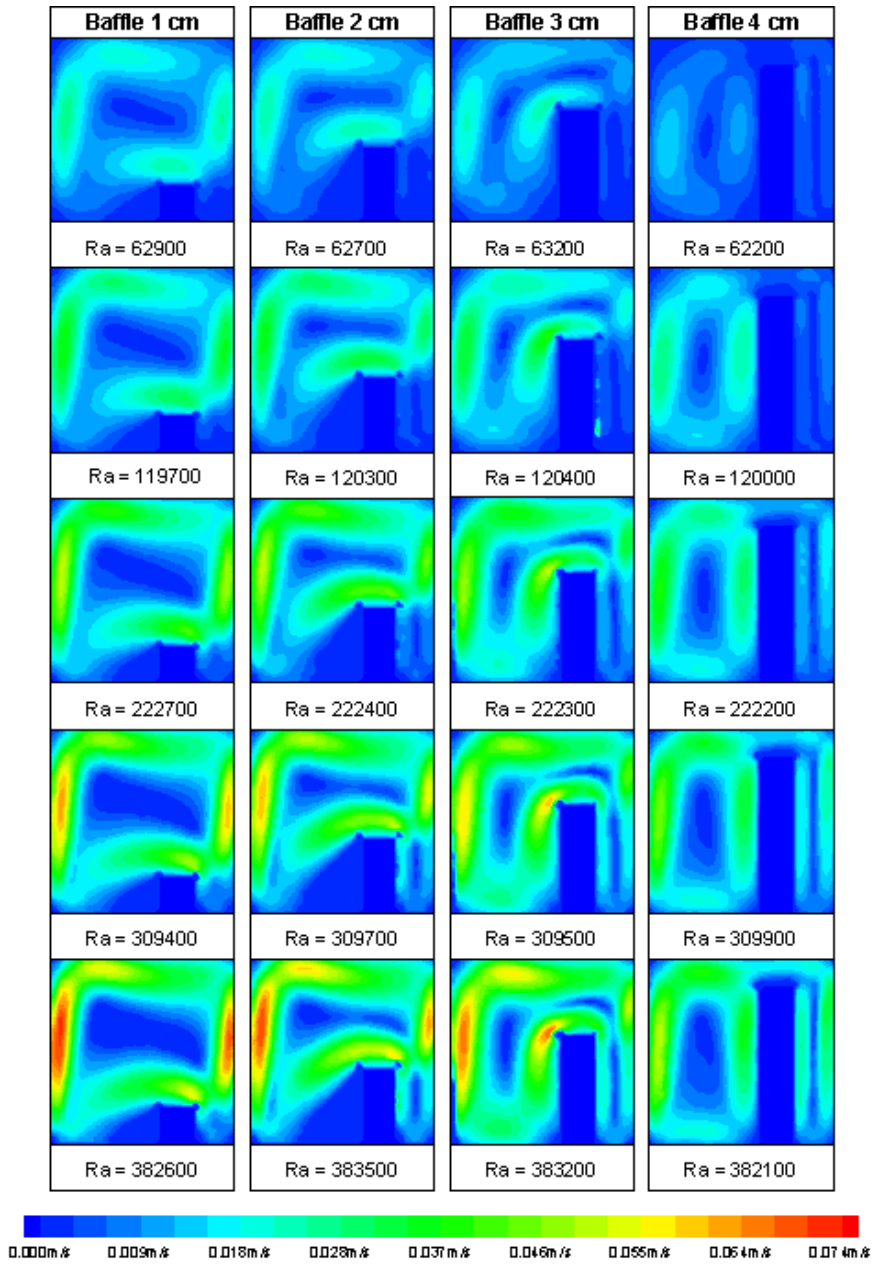

Figure 3.17: Experimental scalar velocity maps for the baffle located at $x/L = 7/10$.

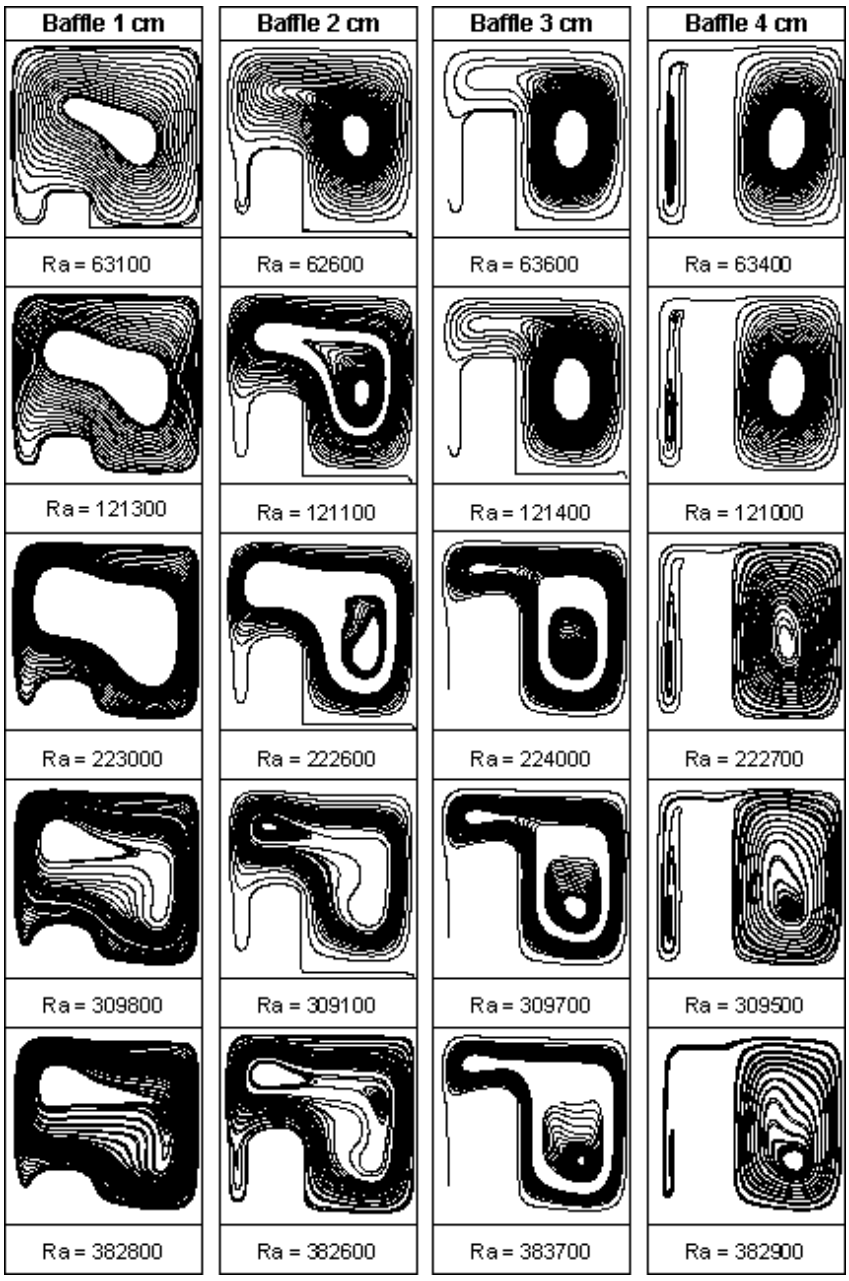

Figure 3.18: Experimental streamlines for the baffle located at $x/L = 3/10$.

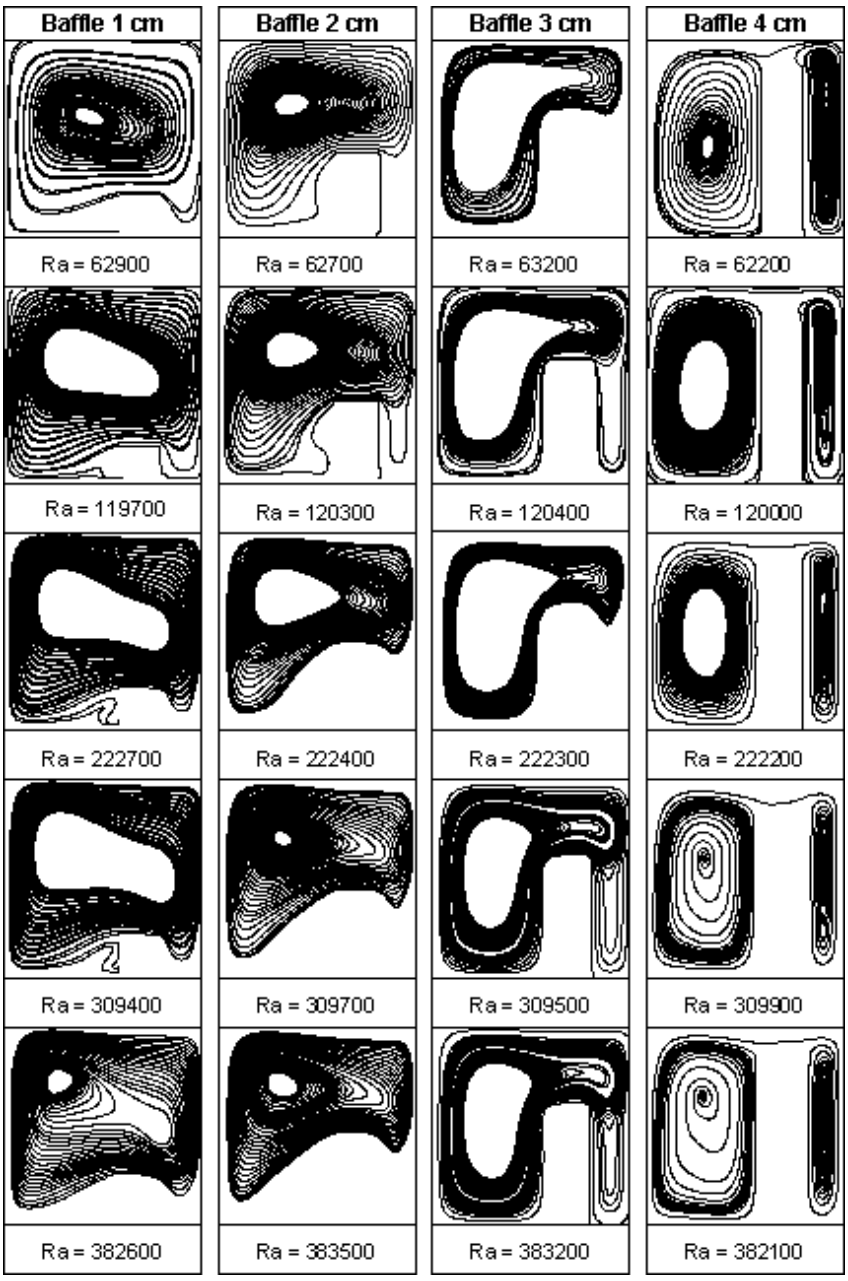

Figure 3.19: Experimental streamlines for the baffle located at $x/L = 7/10$.

Table 3.3: Predicted and measured maximum and average velocities for the baffle located at $x/L = 3/10$ and $7/10$. Deviation between experimental and numerical values is calculated.

		Numerical			**Experimental**			**Deviation**		
x/L	A_p	Ra	V_{max} m/s	V_{ave} m/s	Ra	V_{max} m/s	V_{ave} m/s	Ra %	V_{max} %	V_{ave} %
3/10	1/5	6.25×10^4	0.0209	0.0075	6.34×10^4	0.0209	0.0078	1.42	0.18	3.90
		1.20×10^5	0.0288	0.0106	1.21×10^5	0.0269	0.0105	0.66	-7.24	-0.83
		2.23×10^5	0.0381	0.0143	2.23×10^5	0.0373	0.0145	0.06	-2.07	1.82
		3.10×10^5	0.0445	0.0166	3.09×10^5	0.0443	0.0168	-0.03	-0.58	1.18
		3.83×10^5	0.0498	0.0185	3.83×10^5	0.0503	0.0189	-0.11	1.02	2.42
	2/5	6.25×10^4	0.0202	0.0078	6.36×10^4	0.0209	0.0084	1.76	3.41	7.38
		1.20×10^5	0.0270	0.0108	1.21×10^5	0.0263	0.0111	1.05	-2.50	2.31
		2.23×10^5	0.0363	0.0143	2.24×10^5	0.0358	0.0147	0.66	-1.40	2.69
		3.10×10^5	0.0439	0.0169	3.10×10^5	0.0436	0.0168	0.03	-0.67	-0.52
		3.83×10^5	0.0505	0.0190	3.83×10^5	0.0500	0.0185	-0.16	-1.00	-2.89
	3/5	6.25×10^4	0.0208	0.0078	6.27×10^4	0.0209	0.0084	0.31	7.78	4.32
		1.20×10^5	0.0294	0.0112	1.21×10^5	0.0289	0.0114	0.76	-1.87	1.94
		2.23×10^5	0.0420	0.0148	2.23×10^5	0.0408	0.0151	0.00	-2.87	2.37
		3.10×10^5	0.0523	0.0175	3.09×10^5	0.0520	0.0177	-0.16	-0.56	0.90
		3.83×10^5	0.0620	0.0198	3.83×10^5	0.0564	0.0196	-0.17	-9.82	-0.77
	4/5	6.25×10^4	0.0235	0.0095	6.31×10^4	0.0244	0.0101	1.05	3.77	5.57
		1.20×10^5	0.0335	0.0123	1.21×10^5	0.0333	0.0128	0.91	-0.52	4.32
		2.23×10^5	0.0475	0.0158	2.23×10^5	0.0471	0.0164	0.18	-0.96	4.03
		3.10×10^5	0.0586	0.0183	3.10×10^5	0.0581	0.0191	0.08	-0.97	3.92
		3.83×10^5	0.0678	0.0204	3.83×10^5	0.0677	0.0213	-0.12	-0.09	4.47
7/10	1/5	6.25×10^4	0.0206	0.0075	6.22×10^4	0.0188	0.0072	-0.36	-9.75	-3.41
		1.20×10^5	0.0286	0.0106	1.20×10^5	0.0270	0.0104	-0.12	-5.74	-1.39
		2.23×10^5	0.0383	0.0143	2.22×10^5	0.0369	0.0144	-0.16	-3.64	0.61
		3.10×10^5	0.0454	0.0167	3.10×10^5	0.0446	0.0168	0.12	-1.71	0.58
		3.83×10^5	0.0514	0.0187	3.82×10^5	0.0500	0.0185	-0.30	-2.87	-1.10
	2/5	6.25×10^4	0.0269	0.0094	6.32×10^4	0.0245	0.0088	1.21	-9.64	-6.91
		1.20×10^5	0.0407	0.0138	1.20×10^5	0.0372	0.0134	0.17	-9.29	-3.29
		2.23×10^5	0.0583	0.0191	2.22×10^5	0.0535	0.0189	-0.13	-9.05	-1.01
		3.10×10^5	0.0706	0.0225	3.10×10^5	0.0646	0.0229	-0.01	-9.16	1.79
		3.83×10^5	0.0804	0.0251	3.83×10^5	0.0735	0.0256	-0.02	-9.41	2.19
	3/5	6.25×10^4	0.0262	0.0103	6.27×10^4	0.0240	0.0096	0.43	8.20	-7.01
		1.20×10^5	0.0377	0.0142	1.20×10^5	0.0357	0.0137	0.16	-5.54	-3.40
		2.23×10^5	0.0535	0.0190	2.22×10^5	0.0510	0.0186	-0.10	-4.81	2.55
		3.10×10^5	0.0646	0.0223	3.10×10^5	0.0618	0.0214	0.04	-4.63	-4.20
		3.83×10^5	0.0737	0.0248	3.83×10^5	0.0707	0.0239	0.06	-4.17	-3.61
	4/5	6.25×10^4	0.0261	0.0108	6.29×10^4	0.0254	0.0111	0.72	-2.84	3.14
		1.20×10^5	0.0373	0.0138	1.20×10^5	0.0361	0.0143	-0.41	-3.41	3.53
		2.23×10^5	0.0526	0.0175	2.23×10^5	0.0506	0.0183	0.05	-4.06	4.18
		3.10×10^5	0.0640	0.0201	3.09×10^5	0.0627	0.0210	-0.04	-2.05	4.15
		3.83×10^5	0.0732	0.0222	3.83×10^5	0.0714	0.0231	-0.18	-2.60	3.86

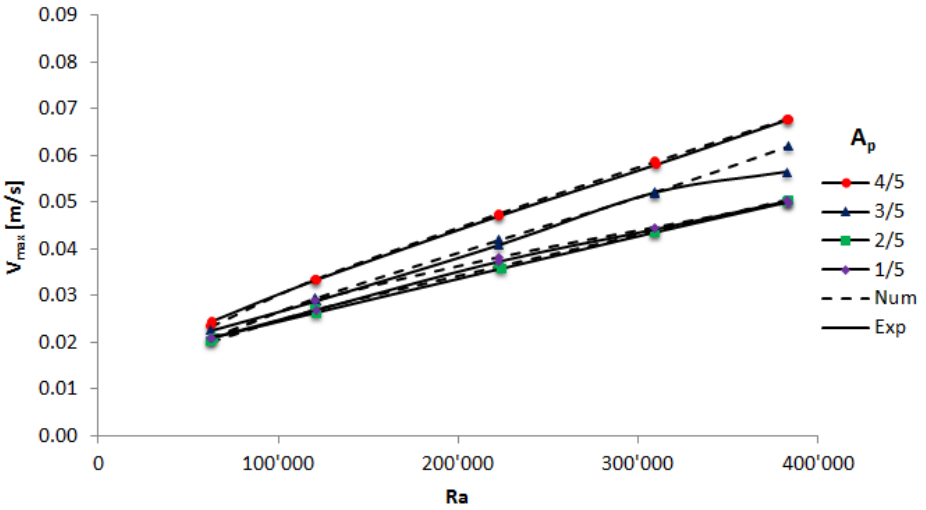

Figure 3.20: Maximum velocity for each case with the baffle located at $x/L = 3/10$.

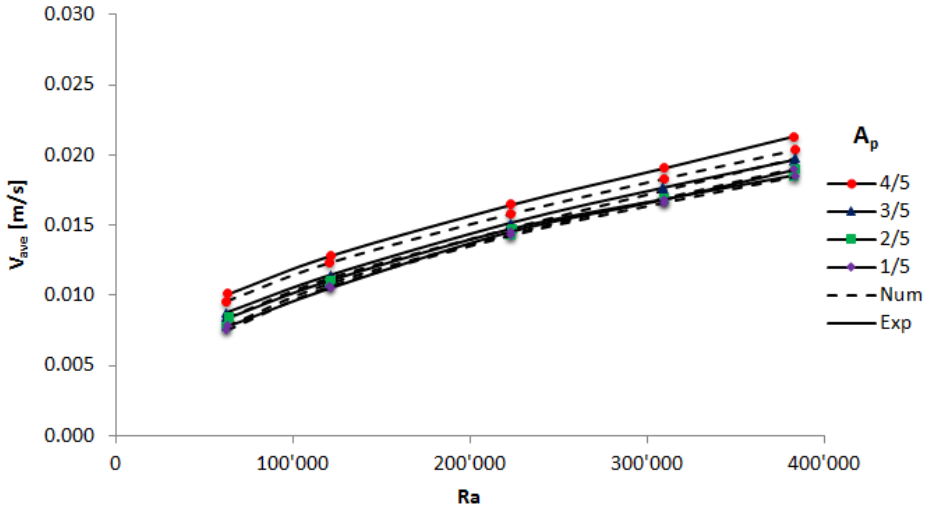

Figure 3.21: Average velocity for each case with the baffle located at $x/L = 3/10$.

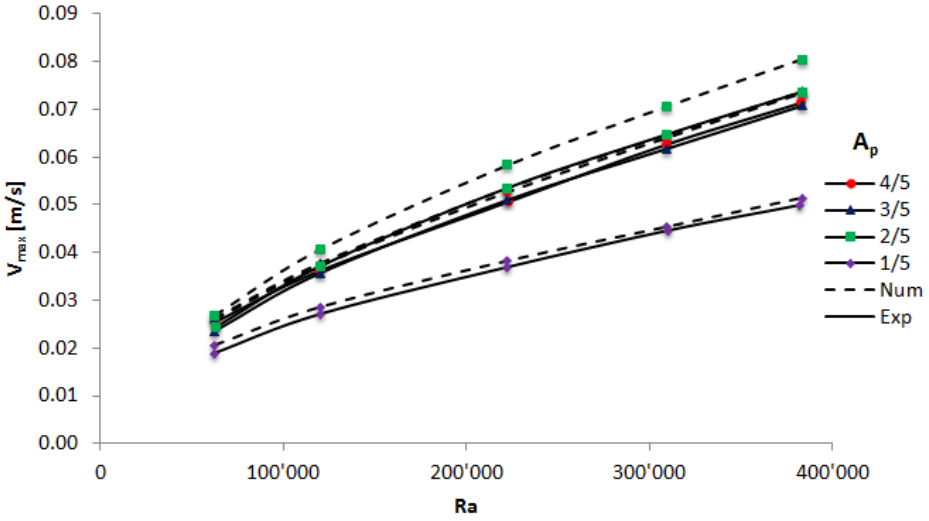

Figure 3.22: Maximum velocity for each case with the baffle located at $x/L = 7/10$.

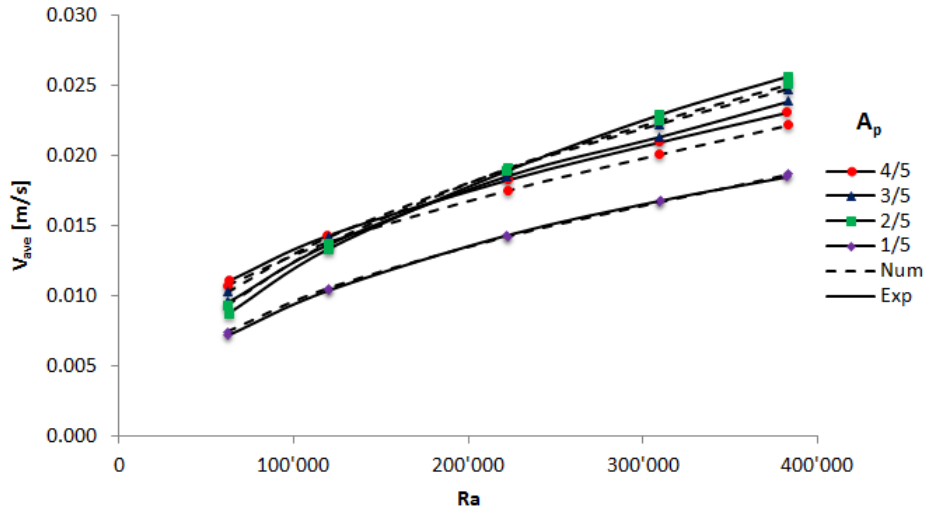

Figure 3.23: Average velocity for each case with the baffle located at $x/L = 7/10$.

$y/L = 0.2$ and this trend corresponds to the case with central baffle (figure 3.8). The sharp peak is followed by a relatively flatter profile in the higher section of the wall due to the gradual heating of the flow. Some cases show an inversion of a trend at $y/L = 0.9$ after the achievement of the minimum value of Nu; at the last zone of the wall the heat exchange tends to increase. A very different Nusselt number profile is displayed in figure 3.24 for the configuration of the baffle placed at $x/L = 3/10$. For the highest value of the Rayleigh number and at $2/5 \leq A_p \leq 3/5$, the Nu distribution along the hot wall shows two distinct peaks: the first peak is near the bottom of the cavity and reaches a moderate value of Nusselt number while the second peak is stronger than the first one and it is located higher than the top of the obstacle. The reason of this is because the cold air after rising the obstacle separates in two different streams; one of these impinges directly on the hot wall and causes the stronger peak and the other flow descends down to the bottom of the hot wall and than goes up to the side of the enclosure. As Ra decreases, these peaks are less evident because the stream along the hot wall is weaker. Therefore the profile near the first peak gradually changes concavity and the Nusselt number considerably reduces its value. The cases with the lowest and the highest aperture ratio present a different trend of Nu: the profile of the first one has a little peak at the bottom of the wall and the heat exchange is almost constant along the surface because the stream within the cavity is feeble. Since the flow encounters a small obstacle and the zone behind the baffle is limited, at $A_p = 4/5$ the Nusselt number profile shows a single strong peak at $y/L = 0.4$.

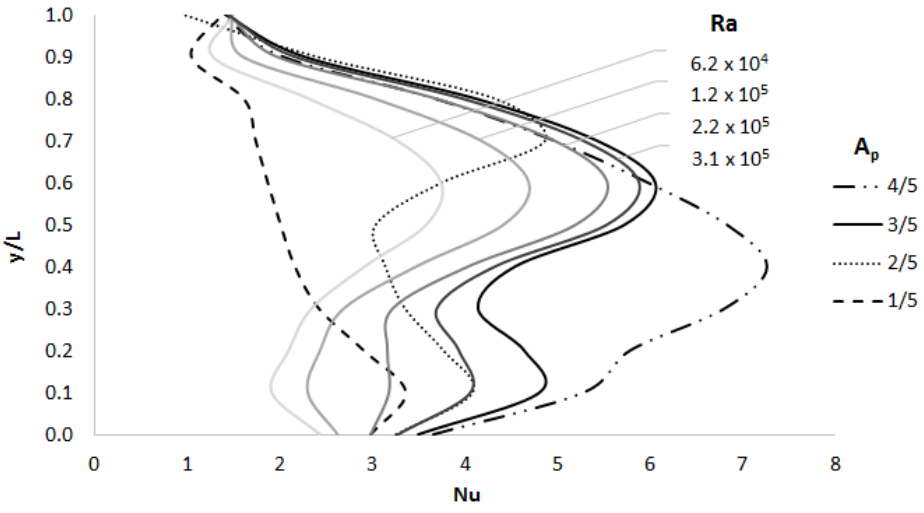

Figure 3.24: Local Nusselt number along the vertical hot wall for an enclosure with the baffle located at $x/L = 3/10$.

The average Nusselt number for the various baffle positions, aperture ratio and Rayleigh numbers are summarized in table 3.2 and plotted in figure 3.26. As a consequence of the previous considerations, Nu increases as Ra increases for all configurations. The reduction of heat exchange from undivided cavity values ranges from $15 - 21\%$ for $A_p = 4/5$ to $50 - 67\%$ for $A_p = 1/5$. The effect of the baffle position on the heat transfer rate is significant for low aperture ratio while for the higher value of A_p, the average Nusselt number values are very similar. In particular, the cases with $A_p = 4/5$ and $3/5$ show the same values of Nu for the central and right position

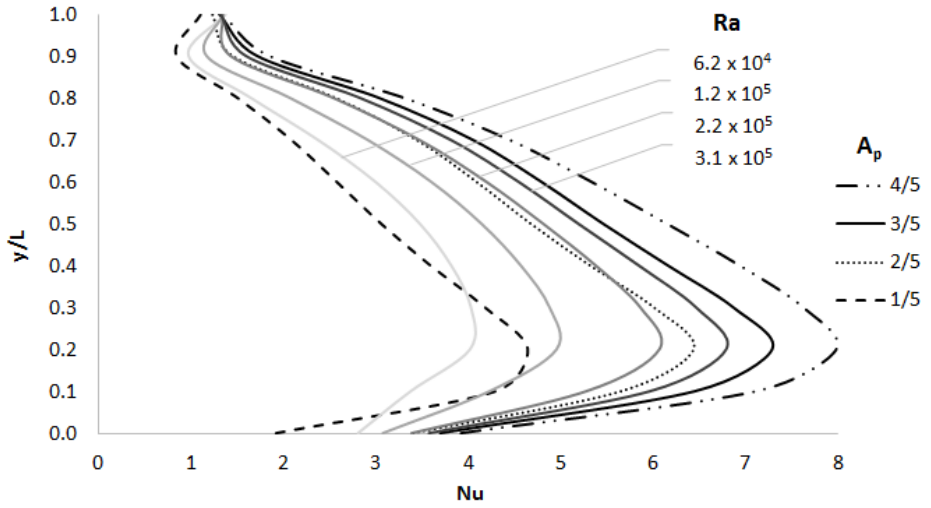

Figure 3.25: Local Nusselt number along the vertical hot wall for an enclosure with the baffle located at $x/L = 7/10$.

of the obstacle. This can be explained by the described temperature and flow fields of those configurations which showed the same trend near the hot wall. For a generic value of Ra within the investigated range and regardless of the baffle position, the highest value of the average Nusselt number is reached at the maximum aperture ratio and gradually decreases as A_p decreses. If the obstacle position is $x/L = 1/2$ and $7/10$ the average Nu depends on the temperature of the stream arriving from the cold wall. Since the flow descends down from the top of the cavity and it cools along the cold wall before reaching the hot surface, the stream temperature decreases as A_p increases because the obstacle deflects the air to the left side of the enclosure. The problem is different for the cases in which the divider is located at the left position; the flow arrives at the top of the baffle with the same temperature but the portion of the hot wall interested directly by the stream increases as the aperture ratio increases.

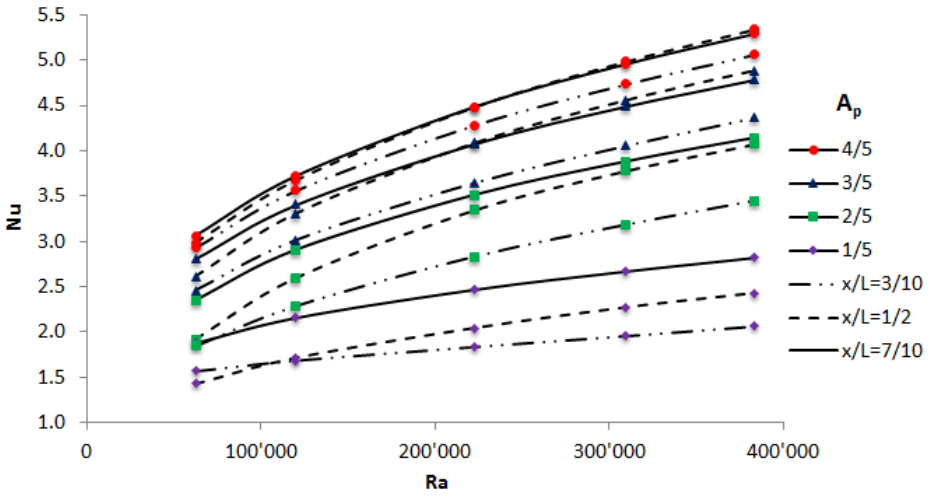

Figure 3.26: Average Nusselt number as a function of the Rayleigh number.

Chapter 4

Effect of the radiative heat transfer

In this section, the effect of the radiative heat transfer is numerically investigated for the same geometrical cavity described in the previous chapter 3. Results are presented as streamlines and velocity and temperature scalar maps; for each case, the maximum and average value of velocity are reported and the average Nusselt number at the hot wall is calculated varying the baffle height and position. Three divider positions along the bottom wall ($x/L = 3/10$, $1/2$ and $7/10$) and four aperture ratios ($A_p = 1/5$, $2/5$, $3/5$ and $4/5$) were considered and compared with the cases in which only pure convection heat transfer is enabled. The baffle thickness and the thermal conductivity ratio were kept at $L/5$ and 2 respectively to simulate an adiabatic obstacle. Air is the used working fluid and it is considered totally transparent to the radiation (nonparticipating medium). Numerical simulations were performed for a Rayleigh number range from 6.25×10^4 to 3.83×10^5 and $Pr = 0.71$.

Figures 4.1, 4.2, 4.3, 4.4, 4.5, 4.6, 4.7, 4.8 and 4.9 show the effect of the combinated convective-radiative heat transfer on the velocity contour map, streamlines and isotherms for all cases. Scalar velocities are plotted using a range which starts with the value zero to the maximum value of the specific configuration. As expected and similar to the trend found for pure convection, the flow field and the temperature distribution are asymmetric. The flow pattern presents the same features when the aperture ratio is larger than 1/5: the current is strong on both the hot and cold walls and next to the top of the baffle while a weak flow is located at the center of the cavity. The bottom part of the enclosure between the divider and the nearest side wall is characterized by a slow-moving fluid and this portion of cavity enlarges as the aperture ratio reduces. For aperture ratio lower than 1/5 main vortex is produced between the obstacle and the farther sidewall while the opposite zone is affected by a weaker flow. Those trends are emphasized for the cases in which the baffle is located at $x/L = 1/2$ and $7/10$. When the divider is located near the sidewalls, the thermal field displays the presence of two different zones linked with the airflow: in the largest area the isotherms are vertically stratified at the center and pressed against both the hot and the cold walls. This area exhibits a strong convective flow. In the smallest space between the baffle and the nearest vertical wall, the isotherms are horizontally stratified and this behavior prevents the flow inlet. A different pattern distinguishes the enclosure with central baffle where the thermal stratification is not present and the convective flow can reach all the entire inner cavity.

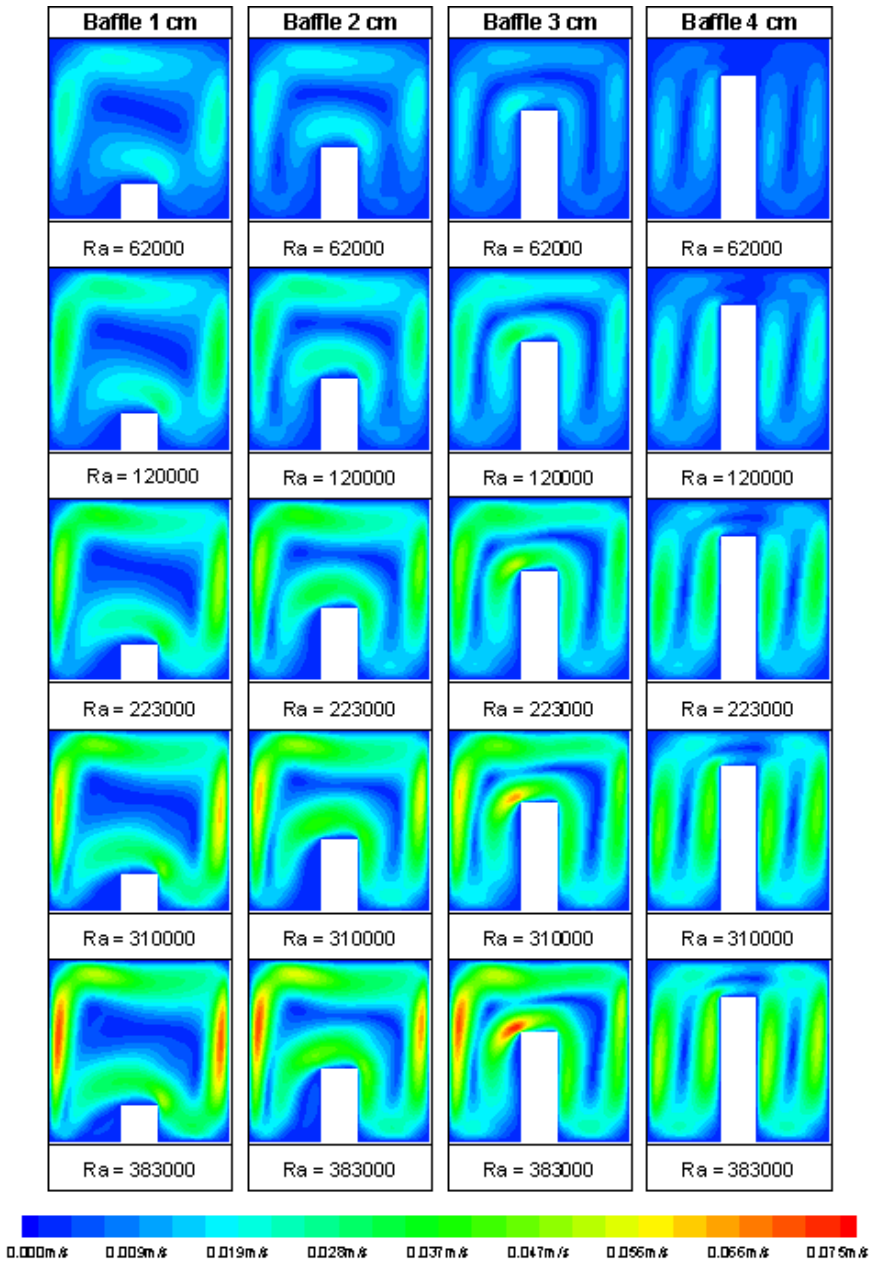

Figure 4.1: Numerical scalar velocity maps for the baffle located at $x/L = 1/2$.

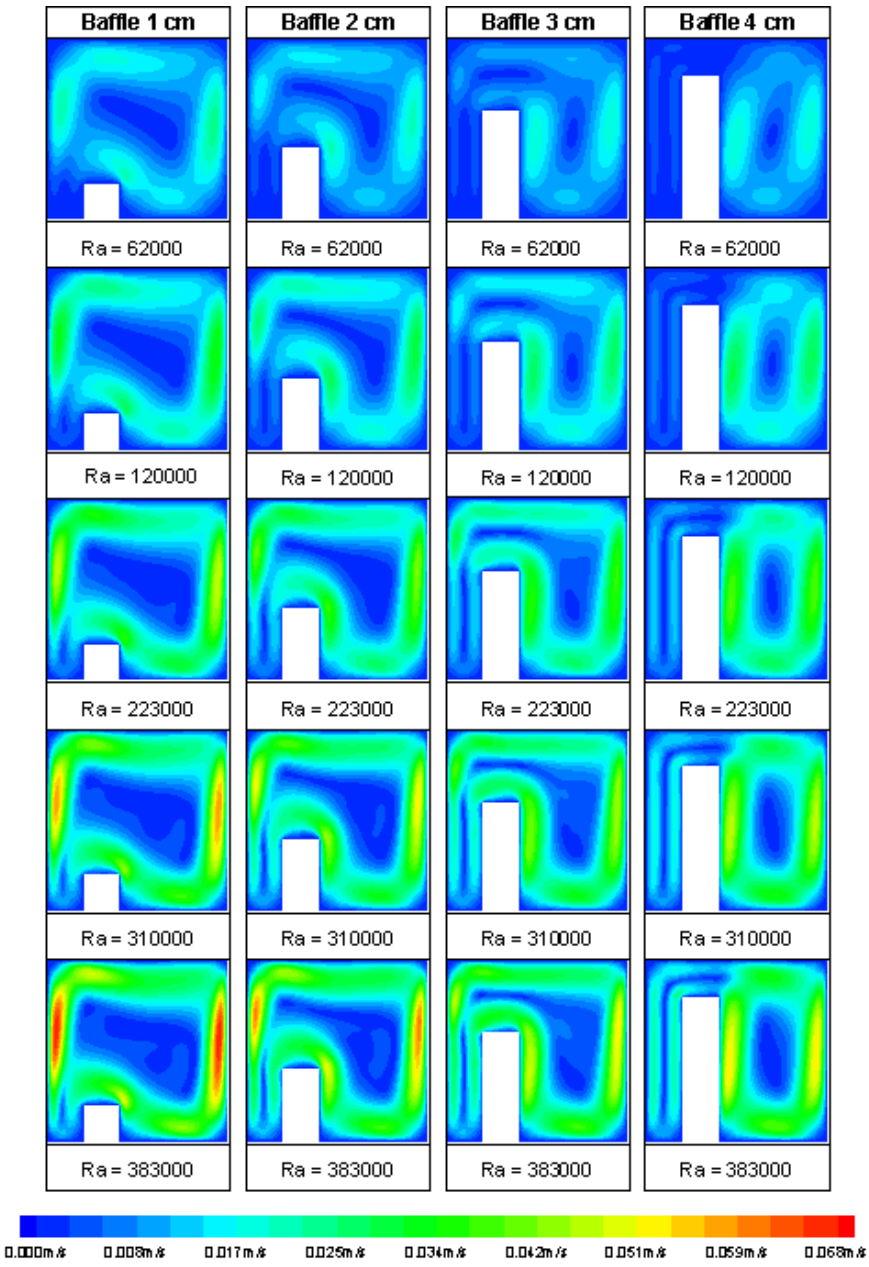

Figure 4.2: Numerical scalar velocity maps for the baffle located at $x/L = 3/10$.

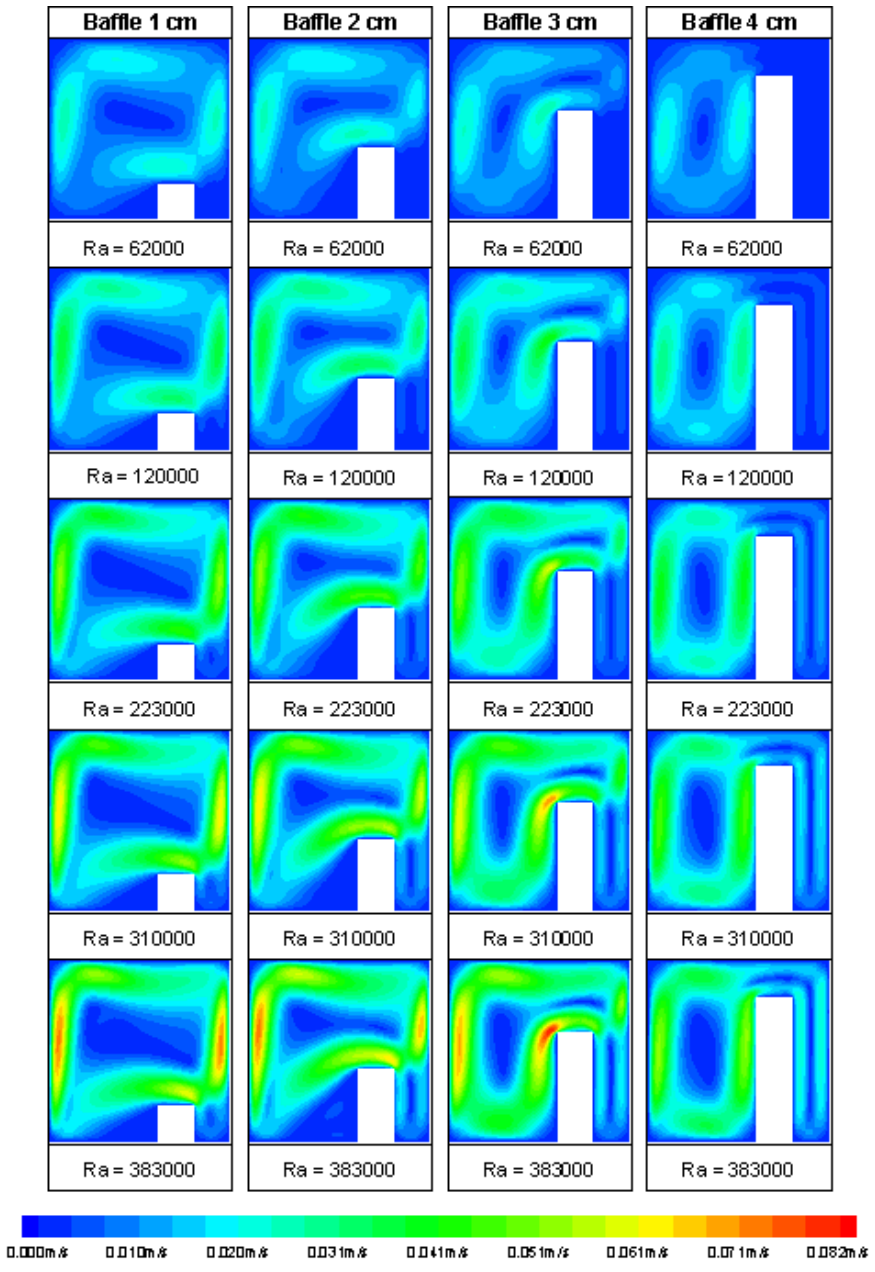

Figure 4.3: Numerical scalar velocity maps for the baffle located at $x/L = 7/10$.

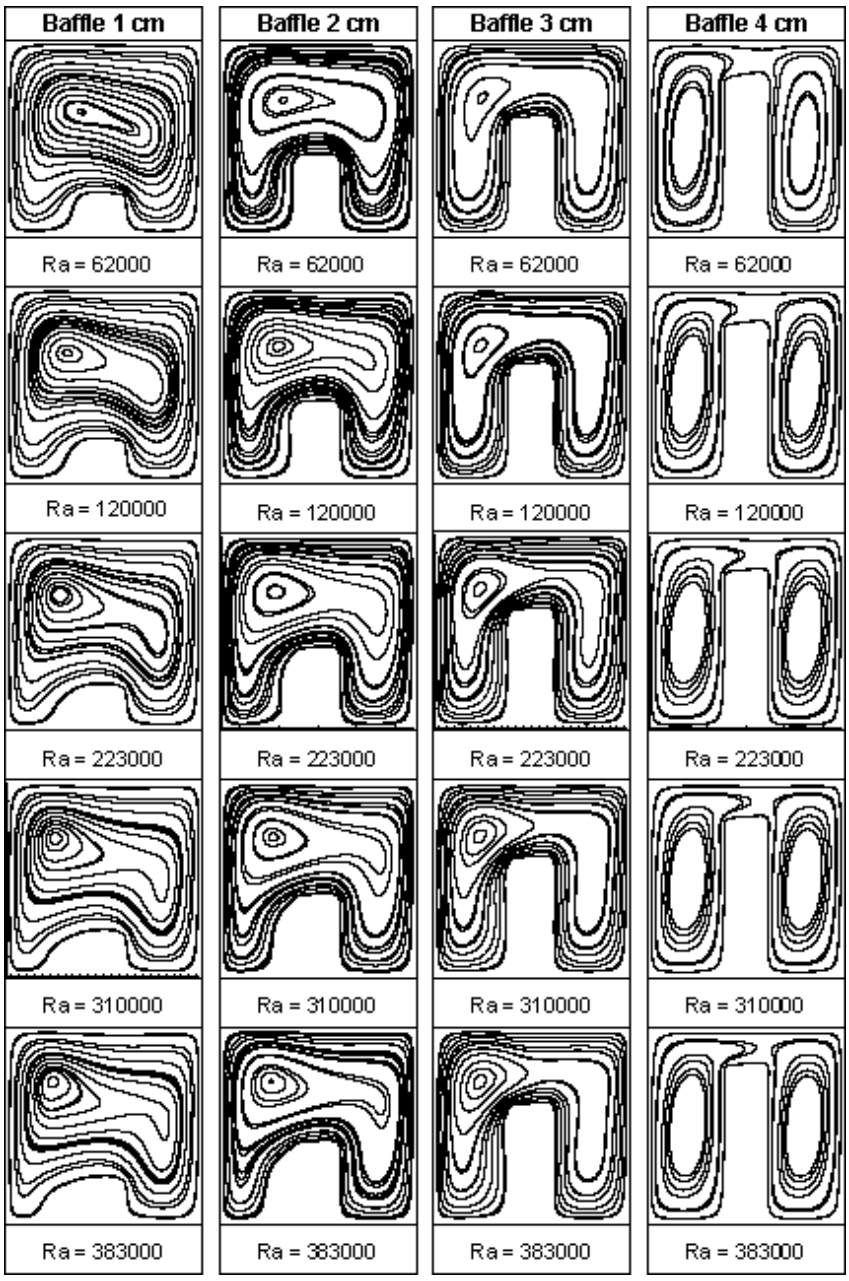

Figure 4.4: Numerical streamlines for the baffle located at $x/L = 1/2$.

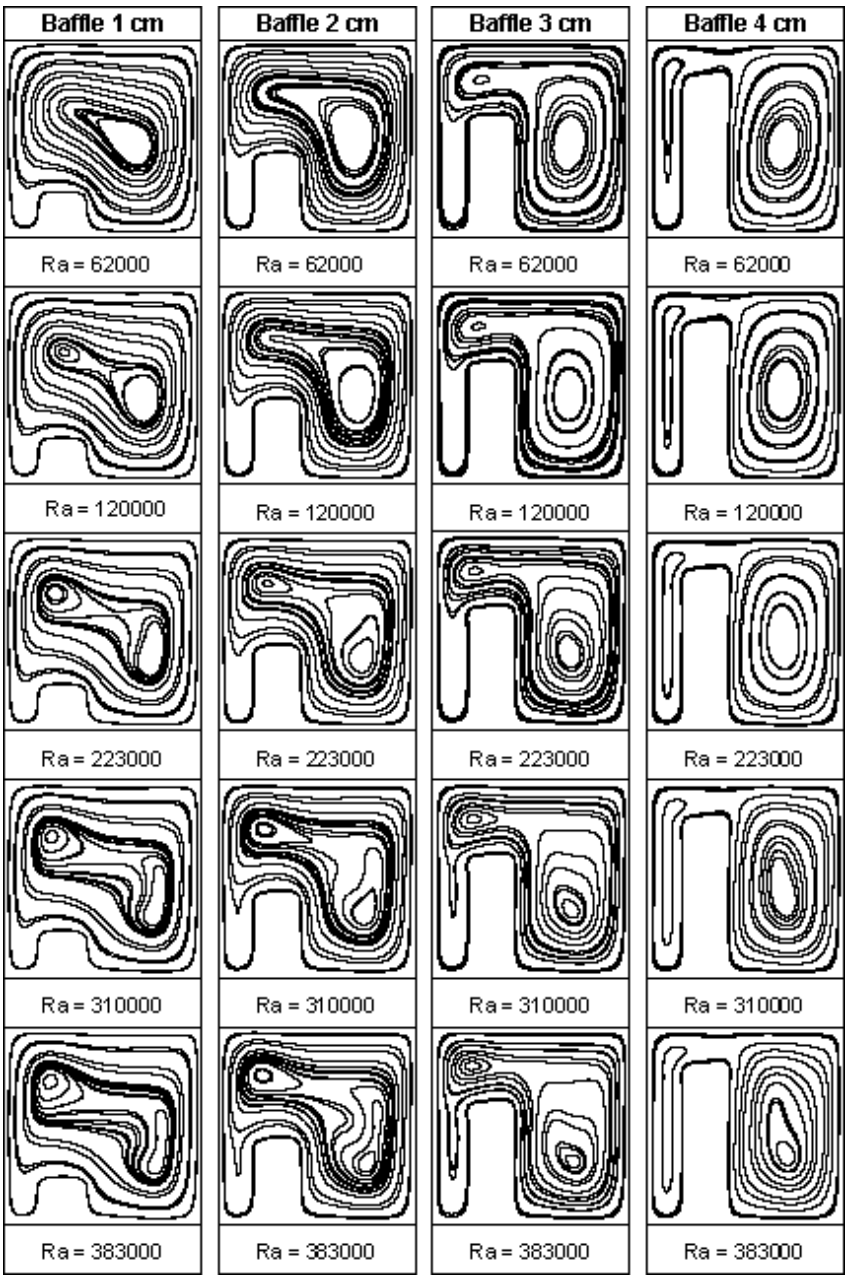

Figure 4.5: Numerical streamlines for the baffle located at $x/L = 3/10$.

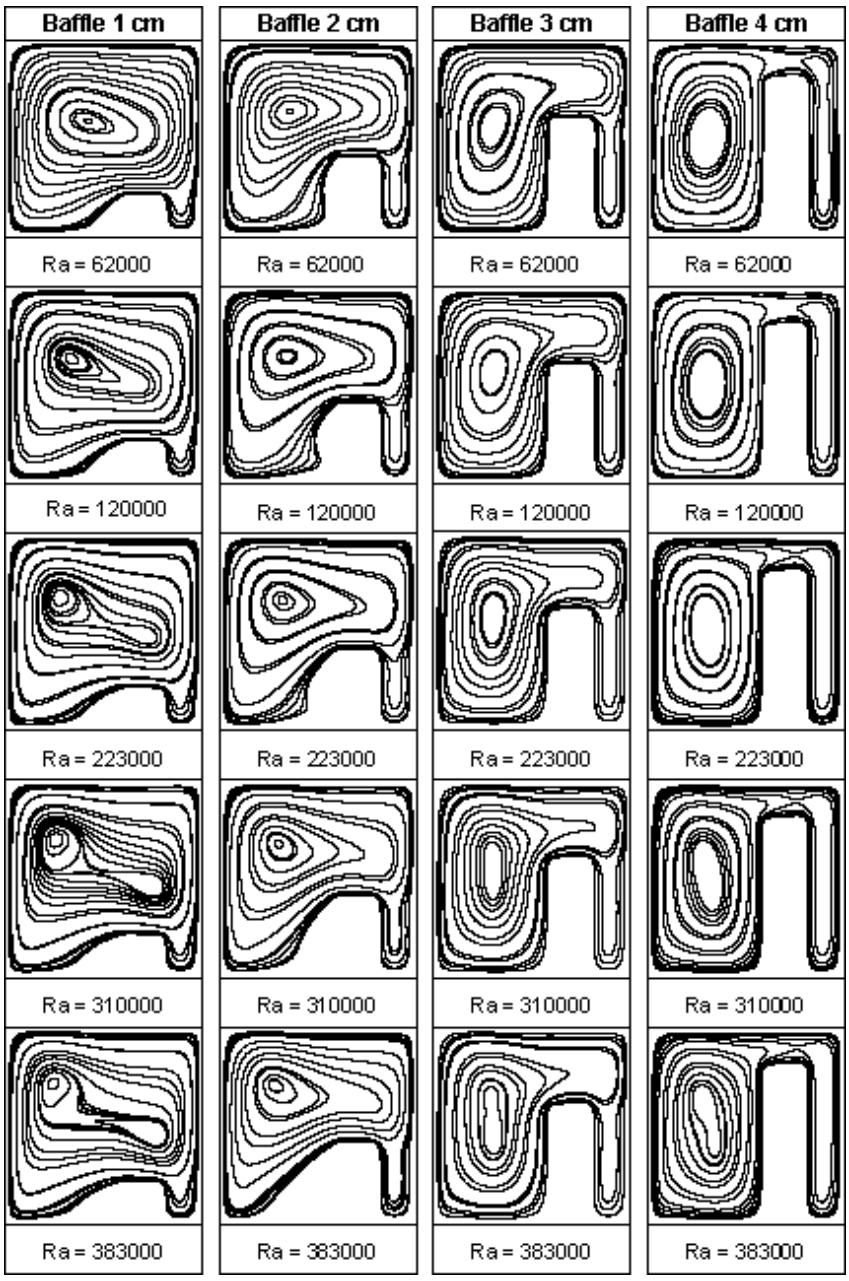

Figure 4.6: Numerical streamlines for the baffle located at $x/L = 7/10$.

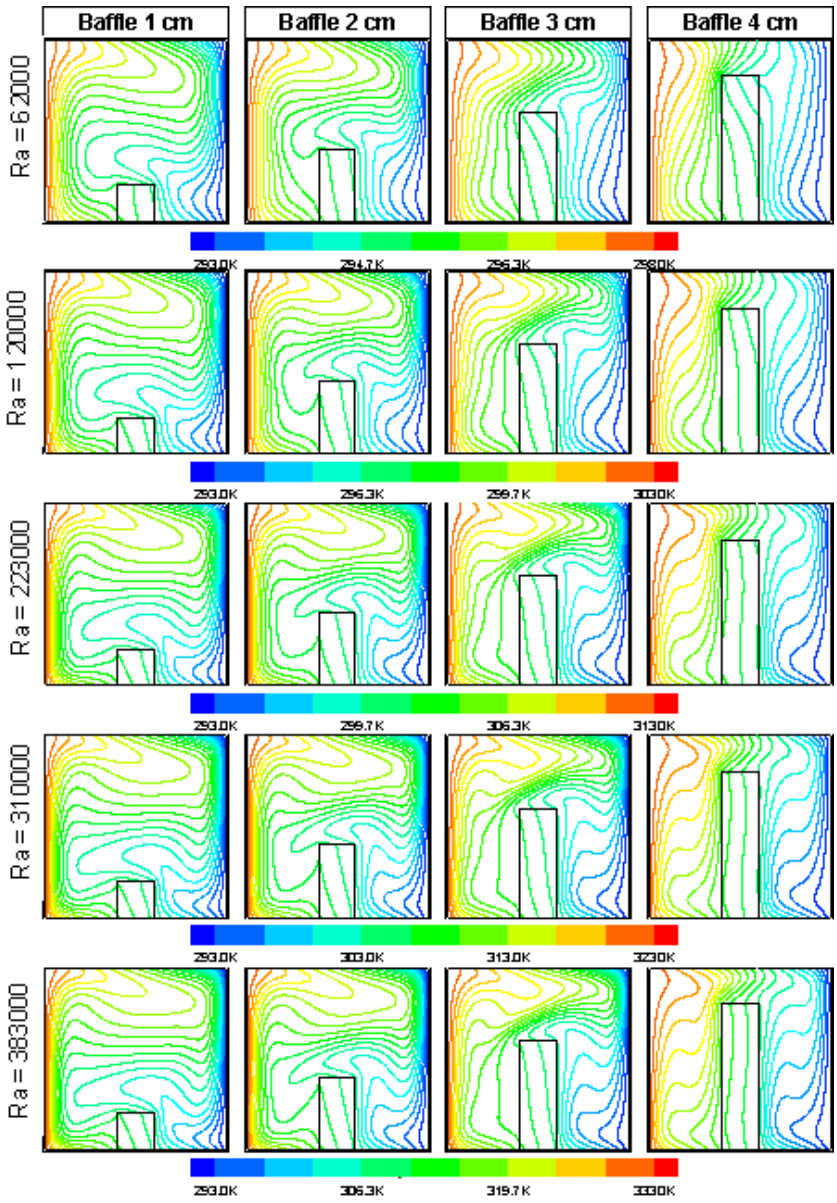

Figure 4.7: Numerical isotherms for the baffle located at $x/L = 1/2$.

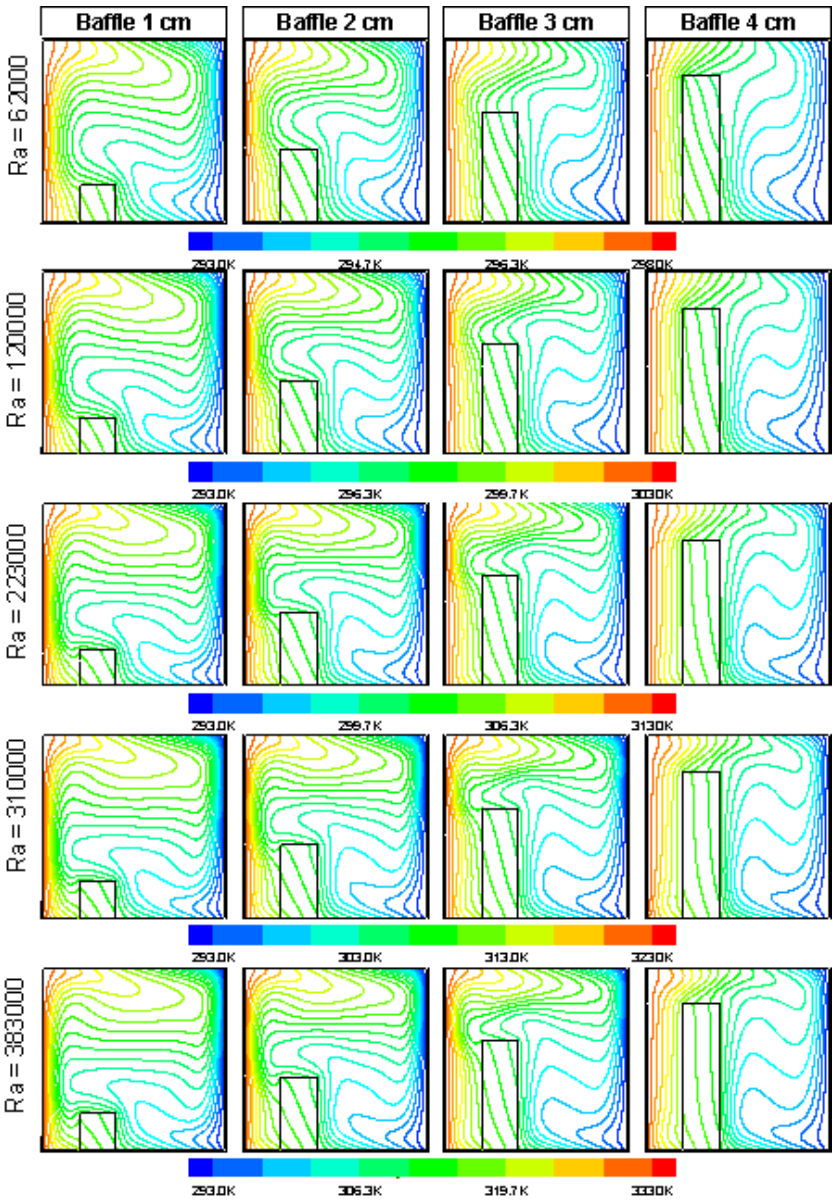

Figure 4.8: Numerical isotherms for the baffle located at $x/L = 3/10$.

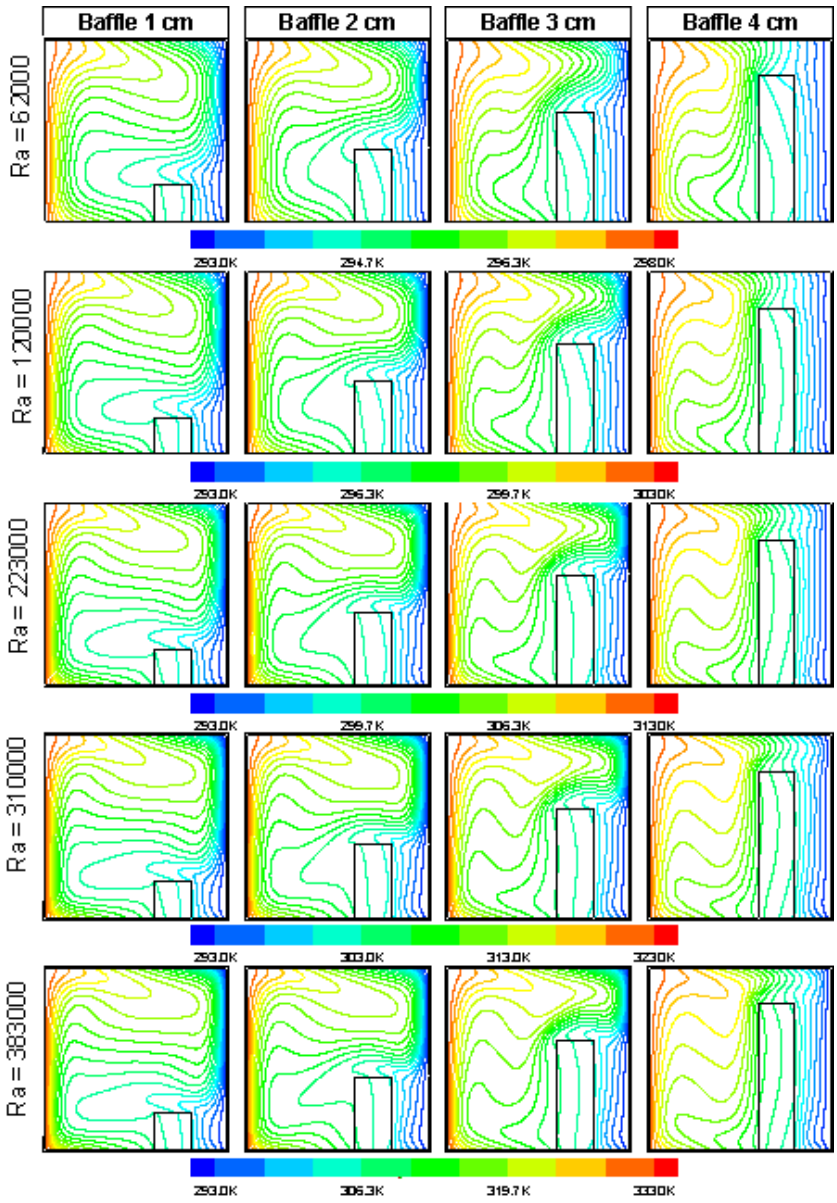

Figure 4.9: Numerical isotherms for the baffle located at $x/L = 7/10$.

For the entire field of Rayleigh number, $A_p = 3/5$ and $4/5$ and at the baffle position of $x/L = 1/2$ and $7/10$ the flow separation occurs behind the divider. The size of the separation zone increases as Ra increases and as the aperture ratio decreases. Separation is mainly caused by the temperature difference between the flow traversing the obstacle and the fluid presented in the divider/hot wall area. An increase of temperature difference provokes a smaller separation region since the flow is forced to descend. This tendency to separation decreases at an aperture ratio of $2/5$ and then completely disappears at the lowest A_p because the flow is constrained to divide into two different rolls.

Comparing these results with pure convection cases, we can see that the radiant heat exchange between the hot wall and the divider plays an important role in the flow pattern next to the baffle. The temperature distribution along the length of the divider is more uniform and overall the temperatures of the obstacle are higher than the nonradiating case. The different temperature of the baffle influences the thermal distribution of all the region around the divider: in front of the divider the thermal stratification tends to reduce and the cold air can easily penetrate the cold wall/baffle zone and then it quickly goes up along the obstacle. At the top of the baffle, the stream is warmer than the pure convection case and less likely to go down towards the bottom of the cavity; for this reason, the separation zone, when it is present, is larger than the nonradiating case. Moreover, the thermal distribution next to the back of the divider causes a recirculation zone with a weak counterclockwise flow. Qualitatively speaking, the results of the numerical simulations which take into account radiative heat transfer match better the experimental results than the pure convective data. In particular, this can be seen behind the obstacle where the region interested in the flow separation is the same for radiating calculation and experimental results.

Table 4.1 reports numerical maximum and average velocities within the cavity and the displacement of predicted values with the experimental data. Results are very similar in value to those described in the previous chapter; a general trend can be noted:

- in all cases velocities increase as Ra increases;
- for $Ra \leq 1.20 \times 10^5$, larger velocities are observed for the largest aperture ratio while for the other value of Rayleigh number the strongest flow occur at $A_p = 2/5$;
- for all Ra lower velocities develop for an aperture ratio of $1/5$;
- in each case, velocities increase as moving the baffle from the hot wall to the cold wall;
- the displacement of the maximum and average velocity ranged respectively $0 - 16\%$ and $0 - 8\%$;
- for the maximum velocity, the displacement between numerical (convection + radiation) and experimental results at higher aperture ratio is very low $(0 - 3\%)$. It is lower than the case in which only pure convection is considered. This trend is reversed for other values of A_p.

As regards the analyzed configuration, the radiative model improves the prediction of the velocity field within the cavity.

The thermal field definition is completed by the calculation of the local and average Nusselt number. Figures 4.10, 4.11 and 4.12 show the Nu for nonradiative simulations

Table 4.1: Predicted maximum and average velocities using combined radiative-convective model. Deviation between experimental and numerical values is calculated.

		x/L=3/10				**x/L=1/2**				**x/L=7/10**			
		Numerical		**Deviation**		**Numerical**		**Deviation**		**Numerical**		**Deviation**	
A_p	Ra	V_{max} m/s	V_{ave} m/s	V_{max} %	V_{ave} %	V_{max} m/s	V_{ave} m/s	V_{max} %	V_{ave} %	V_{max} m/s	V_{ave} m/s	V_{max} %	V_{ave} %
4/5	6.25×10^4	0.0239	0.0098	2.02	3.44	0.0244	0.0102	-0.58	4.37	0.0256	0.0107	-0.82	3.36
	1.20×10^5	0.0340	0.0125	-2.04	2.37	0.0354	0.0102	-0.19	4.01	0.0368	0.0138	-1.83	4.01
	2.23×10^5	0.0481	0.0160	-2.22	2.51	0.0508	0.0172	-0.23	4.15	0.0520	0.0174	-2.72	5.07
	3.10×10^5	0.0589	0.0185	-1.42	2.76	0.0618	0.0198	-0.66	2.86	0.0632	0.0199	-0.89	5.37
	3.83×10^5	0.0678	0.0206	-0.16	3.51	0.0706	0.0218	-1.68	2.18	0.0726	0.0218	-1.66	5.48
3/5	6.25×10^4	0.0207	0.0084	8.36	4.05	0.0215	0.0093	-0.70	4.12	0.0231	0.0099	2.36	-3.30
	1.20×10^5	0.0297	0.0114	-2.78	0.45	0.0340	0.0133	1.10	5.47	0.0365	0.0136	-2.10	-3.30
	2.23×10^5	0.0425	0.0151	-4.27	0.60	0.0503	0.0179	-0.66	4.53	0.0522	0.0181	-2.28	2.75
	3.10×10^5	0.0525	0.0177	-0.98	-0.37	0.0612	0.0209	-0.98	3.83	0.0635	0.0210	-2.84	1.48
	3.83×10^5	0.0609	0.0199	-7.86	-1.64	0.0707	0.0232	-2.26	2.95	0.0726	0.0231	-2.60	3.24
2/5	6.25×10^4	0.0191	0.0076	8.52	10.04	0.0203	0.0089	-4.33	-0.11	0.0268	0.0092	-9.50	-5.44
	1.20×10^5	0.0268	0.0109	-1.72	1.72	0.0337	0.0123	-2.46	1.96	0.0405	0.0136	-8.95	-1.74
	2.23×10^5	0.0370	0.0147	-3.48	0.35	0.0520	0.0178	-1.17	2.39	0.0587	0.0192	-9.81	-1.64
	3.10×10^5	0.0452	0.0174	-3.62	-3.29	0.0649	0.0215	1.63	2.14	0.0714	0.0230	-10.50	-0.43
	3.83×10^5	0.0523	0.0196	-4.47	-5.94	0.0749	0.0244	1.54	0.94	0.0816	0.0259	-10.97	-1.06
1/5	6.25×10^4	0.0196	0.0071	6.14	9.76	0.0160	0.0066	-5.78	1.66	0.0218	0.0078	-16.14	-7.50
	1.20×10^5	0.0288	0.0106	-7.13	-0.56	0.0245	0.0104	-8.15	-0.65	0.0296	0.0108	-9.38	-4.07
	2.23×10^5	0.0397	0.0149	-6.19	-2.43	0.0362	0.0155	-7.03	-2.50	0.0392	0.0147	-6.27	-2.48
	3.10×10^5	0.0471	0.0176	-6.25	-4.66	0.0444	0.0193	-7.37	-3.74	0.0462	0.0173	-3.58	-3.02
	3.83×10^5	0.0532	0.0197	-5.73	-3.87	0.0510	0.0224	-6.27	-5.77	0.0520	0.0194	-4.08	-5.11

along the hot wall; only the highest Ra is considered at different aperture ratio and divider position. Moreover, in the case of $A_p = 3/5$, the entire field of Rayleigh number is plotted. The heat flux levels decrease as the aperture ratio decrease. When the divider is located at $x/L = 3/10$, local Nusselt profile presents low values near the bottom of the cavity and a maximum value over the baffle height, in correspondence to the convex peak. The case with the lowest value of A_p shows a constant vertical profile along the region covered by the baffle. It is important to notice that increasing the Rayleigh number, the profile remains the same while the value of local Nu at first decreases until 1.2×10^5 and then increases. A different trend can be seen when the obstacle is fixed in the middle of the floor. Local Nusselt number values along the hot wall are more constant and the profile is thin; two different peaks appear for $A_p = 3/5$ cases. A very similar trend is displayed for the divider placed at $x/L = 7/10$. The only difference regards the lower zone of the hot wall where Nusselt values are higher than the previous case.

Compared to nonradiative results, radiation enhances local Nusselt number along the hot wall. Since the divider is assumed to be opaque to the radiation, the effect of radiation on the lateral wall is more significant along the region corresponding to the aperture zone.

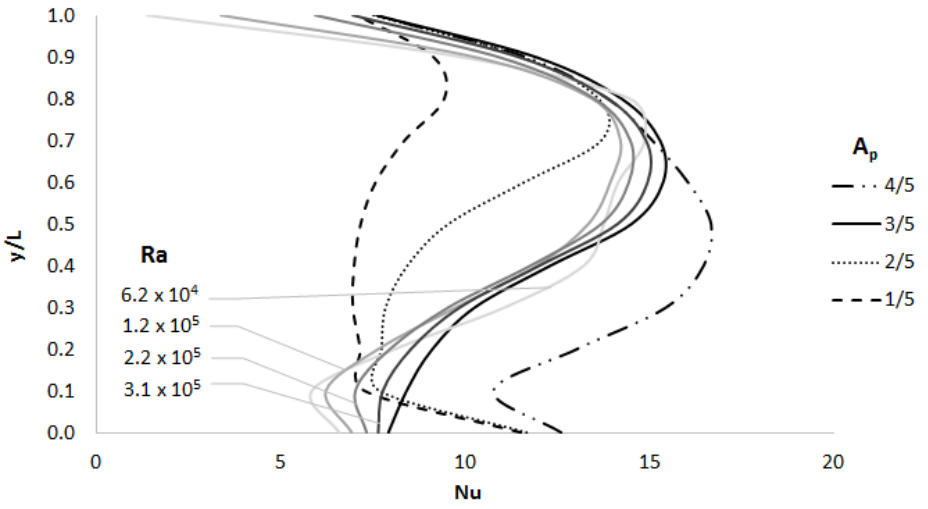

Figure 4.10: Numerical (convective-radiative model) local Nusselt number along the vertical hot wall for an enclosure with the baffle located at $x/L = 3/10$.

The average Nusselt number along the hot wall for the investigated cases is summarized in table 4.2; both overall and radiative Nusselt number are shown for all the different configurations. Radiation is the dominant mode of heat transfer and accounts for around $65 - 80\%$ of the overall heat transfer at the hot wall. Increasing the aperture ratio, all the three components of the average Nusselt number decrease. However, radiative and convective average Nu exhibit different trend as the Rayleigh number changes. Similarly to the pure convection results, Nu_{conv} increases as Ra increases while initially Nu_{rad} decreases to $Ra = 2.23 \times 10^5$ and then increases as Ra increases. The overall Nusselt number is the sum of these two values and it shows a mixing trend: Nu_{ove} decreases up to $Ra = 1.2 \times 10^5$ and then increases as Ra increases.

Analyzing the convective Nusselt number, it can be seen that Nu_{conv} for the pure

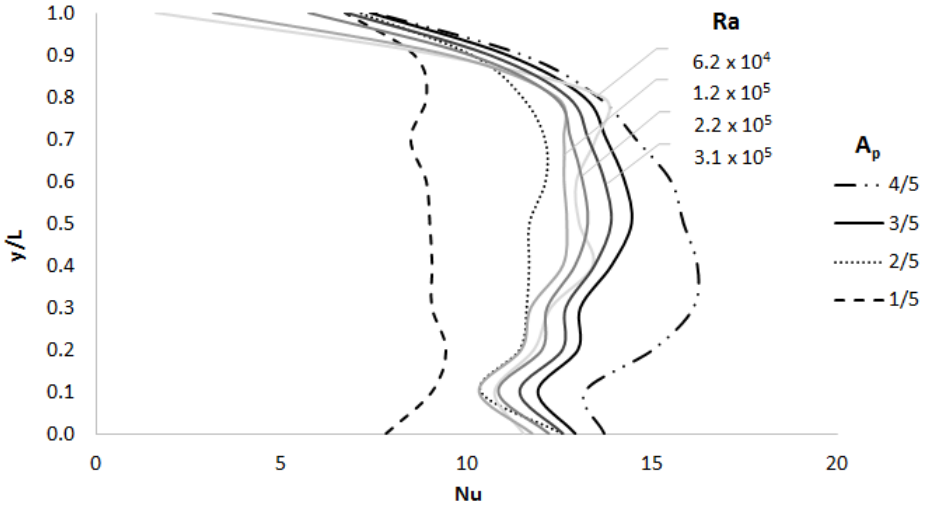

Figure 4.11: Numerical (convective-radiative model) local Nusselt number along the vertical hot wall for an enclosure with the baffle located at $x/L = 1/2$.

convection model is higher than Nusselt value for the radiative model; this displacement is generally lower than 5% but for some configurations it arrives at 17%. This is caused by the different temperature and flow field generated within the cavity by the presence of the radiative heat transfer. In fact, though in radiating case maximum and average velocity are higher than the ones in nonradiating case, the stream near the hot wall is hotter. The greater importance of the second phenomenon compared to the first one causes the decrease of the Nu_{conv} as illustrated in figure 4.13.

Table 4.2: Numerical average Nusselt number. A distinction is made between convective and radiative contribution.

		$A_p = 4/5$			$A_p = 3/5$			$A_p = 2/5$			$A_p = 1/5$		
x/L	Ra	Nu_{ove}	Nu_{rad}	Nu_{conv}	Nu_{ove}	Nu_{rad}	Nu_{conv}	Nu_{ove}	Nu_{rad}	Nu_{conv}	Nu_{ove}	Nu_{rad}	Nu_{conv}
3/10	6.2×10^4	13.06	10.20	2.85	11.30	8.77	2.53	9.26	7.15	2.11	7.89	5.91	1.97
	1.2×10^5	12.49	9.03	3.47	10.83	7.85	2.99	8.91	6.53	2.38	7.34	5.42	1.92
	2.2×10^5	12.82	8.70	4.12	11.12	7.64	3.47	9.20	6.46	2.74	7.32	5.38	1.93
	3.1×10^5	13.32	8.82	4.50	11.56	7.80	3.75	9.59	6.65	2.95	7.51	5.55	1.97
	3.8×10^5	13.81	9.05	4.76	1.99	8.05	3.95	9.97	6.89	3.08	7.76	5.76	2.00
1/2	6.2×10^4	13.18	10.32	2.86	12.00	9.45	2.54	10.36	8.41	1.95	8.95	7.28	1.68
	1.2×10^5	12.68	9.13	3.55	11.50	8.46	3.04	9.94	7.44	2.49	8.28	6.39	1.89
	2.2×10^5	13.09	8.78	4.31	11.85	8.11	3.74	10.29	7.23	3.05	8.29	6.14	2.15
	3.1×10^5	13.65	8.89	4.77	12.35	8.20	4.15	10.74	7.35	3.39	8.54	6.23	2.30
	3.8×10^5	14.18	9.11	5.07	12.82	8.40	4.41	11.15	7.56	3.59	8.81	6.42	2.40
7/10	6.2×10^4	13.31	10.34	2.97	12.65	9.93	2.72	11.81	9.47	2.33	10.48	8.42	2.06
	1.2×10^5	12.79	9.15	3.63	12.00	8.70	3.30	10.99	8.18	2.80	9.52	7.24	2.28
	2.2×10^5	13.17	8.80	4.37	12.25	8.32	3.93	11,07	7.76	3.31	9.39	6.85	2.54
	3.1×10^5	13.72	8.91	4.81	12.72	8.40	4.31	11.41	7.82	3.60	9.59	6.90	2.69
	3.8×10^5	14.25	9.14	5.11	12.78	8.21	4.58	11.78	8.00	3.78	9.85	7.06	2.78

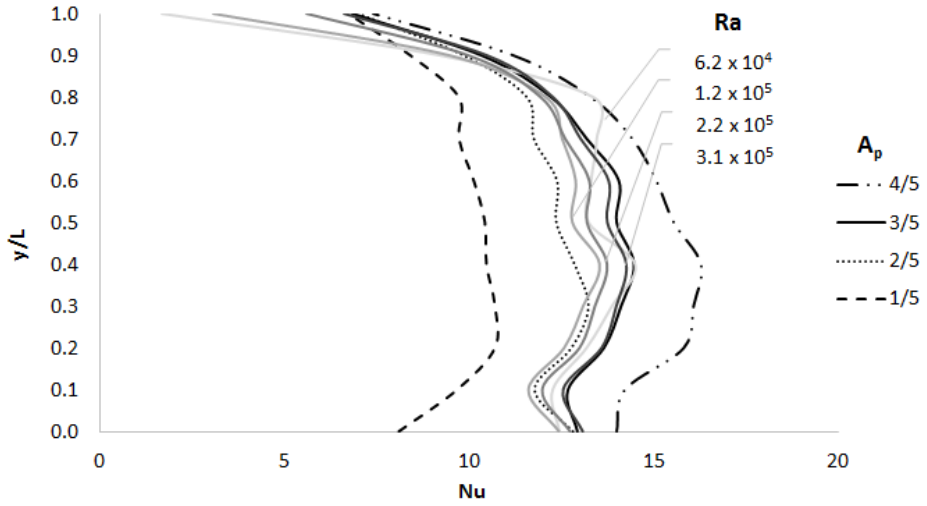

Figure 4.12: Numerical (convective-radiative model) local Nusselt number along the vertical hot wall for an enclosure with the baffle located at $x/L = 7/10$.

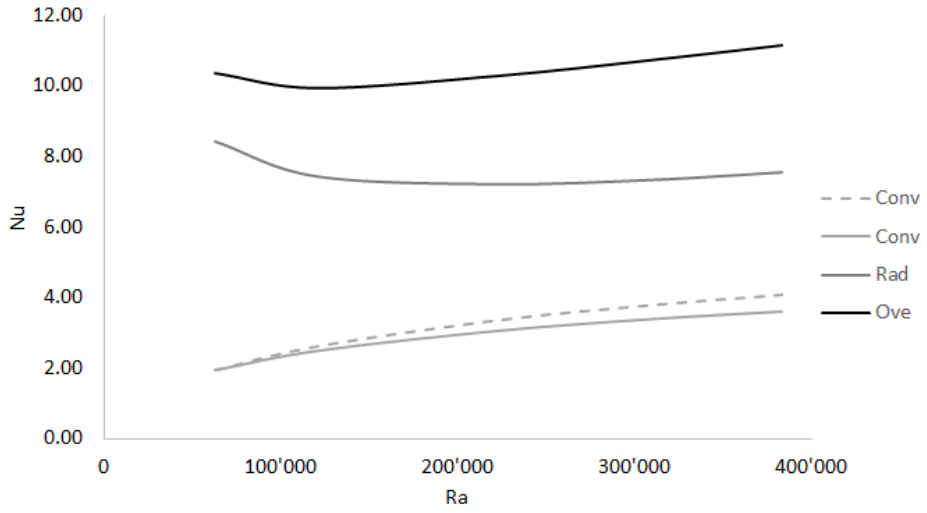

Figure 4.13: Numerical average Nusselt number for the case with the baffle located at $x/L = 1/2$ and $A_p = 2/5$. Dotted line represents the pure convection results while the continuous lines show the different contribution of radiative, convective and overall heat transfer.

Chapter 5

Effect of the tilting angle

In order to examine the effect of the variation of the gravity vector on the natural convection, four different tilting angles of the cavity ($0, \frac{\pi}{6}, \frac{\pi}{3}, \frac{\pi}{2}$) were investigated. An air-filled square enclosure with an internal vertical baffle of 1 cm $\times$1 cm size placed in the middle of the bottom wall was used. Experimental tests and numerical simulations were performed for a wide range of Rayleigh number ($6.25 \times 10^4 - 3.83 \times 10^5$). Results were expressed as velocity contour maps and streamline for a complete definition of the flow field; average and maximum velocity values were extracted for each case. Moreover, numerical temperature maps and the calculation of the Nusselt number allowed the comprehension of the thermal field within the cavity.

Figures 5.1, 5.2 and5.3 show the predicted effect of the tilting angle on the streamlines, scalar velocity maps and temperature maps for the studied cases. The configuration with $\theta = 0$ is considered the basic case and its description has already been made in chapter 3. The flow field is characterized by two fast regions in correspondence of both the hot and cold sidewalls and a low-velocity zone is located at the center of the enclosure. In front of the baffle, the warm stream descending down along the cold wall decelerates and a weak flow is observed in the region between the divider and the wall. The higher temperature of the obstacle forces the air to reach the top of the baffle and than the low-temperature gradient behind the divider causes the flow separation from the solid. In all cases, velocity value increases as Rayleigh number increases but qualitatively speaking the flow field does not change. When the cavity is inclined at $\frac{\pi}{6}$, the predicted velocity and temperature patterns are similar to the previous ones. The only difference can be observed behind the divider where the flow tends to rise to the top of the enclosure instead of descending to the bottom wall. Increasing the Rayleigh number, at the right corner of the obstacle the air increases its velocity and, consequently, the flow is forced to divide into two different streams: the first stream rises along the hot wall while the second one descends down in the region behind the divider and then separates in two other currents that get in along the solid surfaces (hot wall and baffle). At an inclination angle of $\frac{\pi}{6}$ and lowest Ra, separation behind the obstacle is complete and the entire stream goes up to the highest part of the hot wall. The entire region between the wall and the baffle is affected by a thermal stratification that prevents the flow entry. The two areas where the flow is faster move from the sidewall to the passive surfaces (top of the cavity and obstacle walls) while the stream near the hot and cold walls is weak. Moreover, the velocity pattern changes as the Rayleigh number increases over 2.23×10^5; a new recirculation zone can be clearly noted between the baffle and the hot wall while the central stagnant zone becomes

smaller. In these regions the isotherms are deformed. The configuration at $\theta = \frac{\pi}{2}$ means that the gravity vector is perpendicular to the active walls and parallel to the adiabatic ones. This pattern corresponds to the Rayleigh-Bernard convection because the active walls are located at the bottom (hot) and at the top (cold) of the enclosure. The streamlines and the isotherms are symmetrical whatever is the value of Ra. Four vortices can be distinguished and they correspond to four different circulations in the four edges of the cavity. Buoyancy force drives the flow along the inactive walls and at the top of the cavity the cold descending fluid joins up with the hot rising air. At the center of the enclosure, these two streams combine in a single main current that is forced to separate next to the top of the baffle. Two slow vortices develop between the divider and the sidewalls because here the weak flow is confined by the upper fluid.

The good agreement between numerical prediction and experimental results about the natural convection mechanism within the cavity can be observed in figures 5.4 and 5.5. Qualitatively the experimental flow pattern is well described by the numerical model and the main flow over the baffle is the same in both the streamlines maps. Some discrepancies can be seen in the region behind the obstacle, usually in the cases in which the inclination angle is $\frac{\pi}{6}$. In these cases, the recirculation zone between the divider and the hot wall is weaker than the main stream and the PIV system struggles to track the flow. Moreover, the effect of the reflection of the laser light on the baffle and (or) the not so perfect alignment of the obstacle in the cavity can affect the measurement in this zone. Since velocities increase as the tilting angle increases, at $\theta = \frac{\pi}{3}$ the vortex behind the baffle is well characterized by the experimental PIV measures and well described by CFD code. For $\theta = \frac{\pi}{2}$, the high difference between the upper and the bottom flow prevents the right visualization of the velocity field. The matching between experimental and numerical maps is not good, in particular near the hot wall where the flow is distinguished by a higher turbulence. Streamlines maps show clearly the four vortices but they are larger than the numerical ones.

The quantitative comparison between calculated and measured maximum and average velocities within the enclosure can be performed basing on the data showed in table 5.1. Looking at the table some considerations can be made. First of all, the velocities increase as the Rayleigh number increases. A general trend can be found for $\theta \leq \frac{\pi}{2}$: for all Ra lower velocities can be observed for small θ and velocities increase as θ increases. In a lot of cases and for the same Ra, the maximum velocity displacement between the different configurations increases as the Rayleigh number increases. Furthermore, the increase of both the maximum and average velocities is larger for $\theta = \frac{\pi}{3}$ and decreases moving to lower inclination angles. $\theta = \frac{\pi}{2}$ is a particular configuration because velocities do not follow the described trend; V_{max} and V_{ave} tend to decrease and in particular V_{max} reaches the lowest value. This fact can be induced by the different flow pattern generated by natural convection.

In addition to the results of the present work, table 5.1 also reports the results of Corvaro *et al.* [45] studies, useful to evaluate the combined effect of the tilting angle variation and the divider presence. Researchers investigated numerically and experimentally the influence of the direction of the gravity vector on natural convection of air within a square enclosure differentially heated from the side and without the divider. Results were found for a field of Ra between 1.2×10^5 and 4.67×10^5. The presence of the baffle within the enclosure produces an important qualitative and quantitative effect on the velocity field for $\theta \geq \frac{\pi}{6}$. Patterns substantially change and the main stream takes place along the top of the cavity instead of at the hot wall. Moreover, the flow accelerates at the right corner of the baffle, separates from it and then clutches to the hot wall at $y/L \approx 0.5$. V_{max} and V_{ave} increase up to 2 orders of

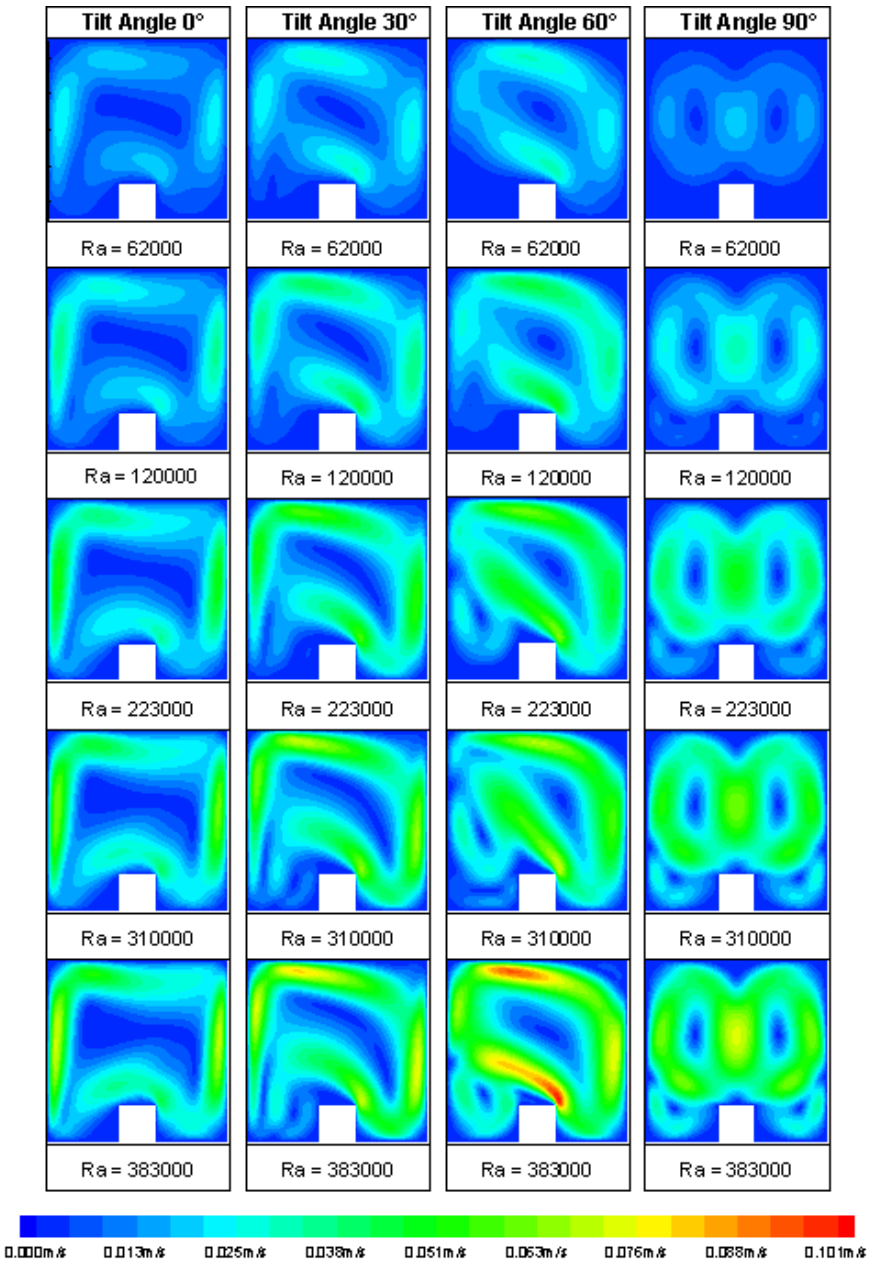

Figure 5.1: Numerical scalar velocity maps.

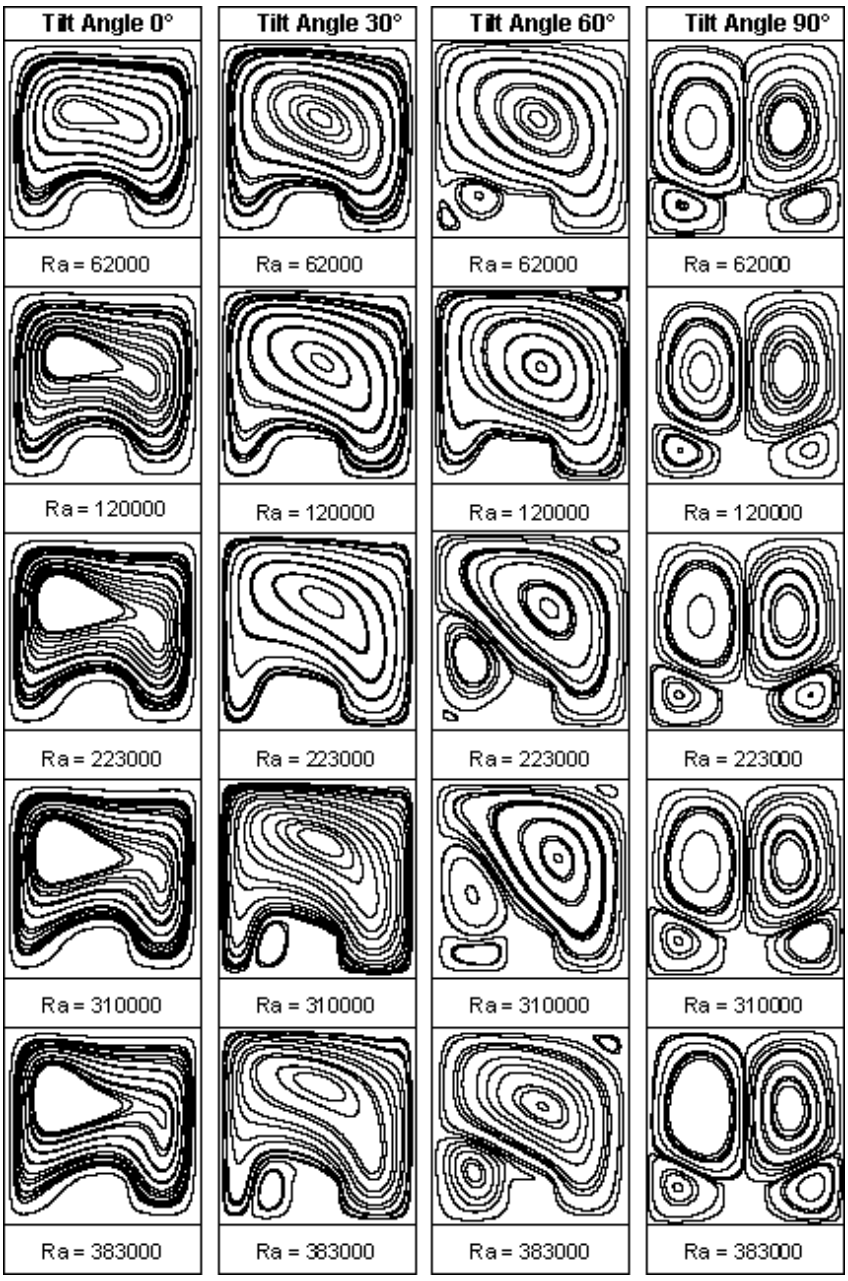

Figure 5.2: Numerical streamlines.

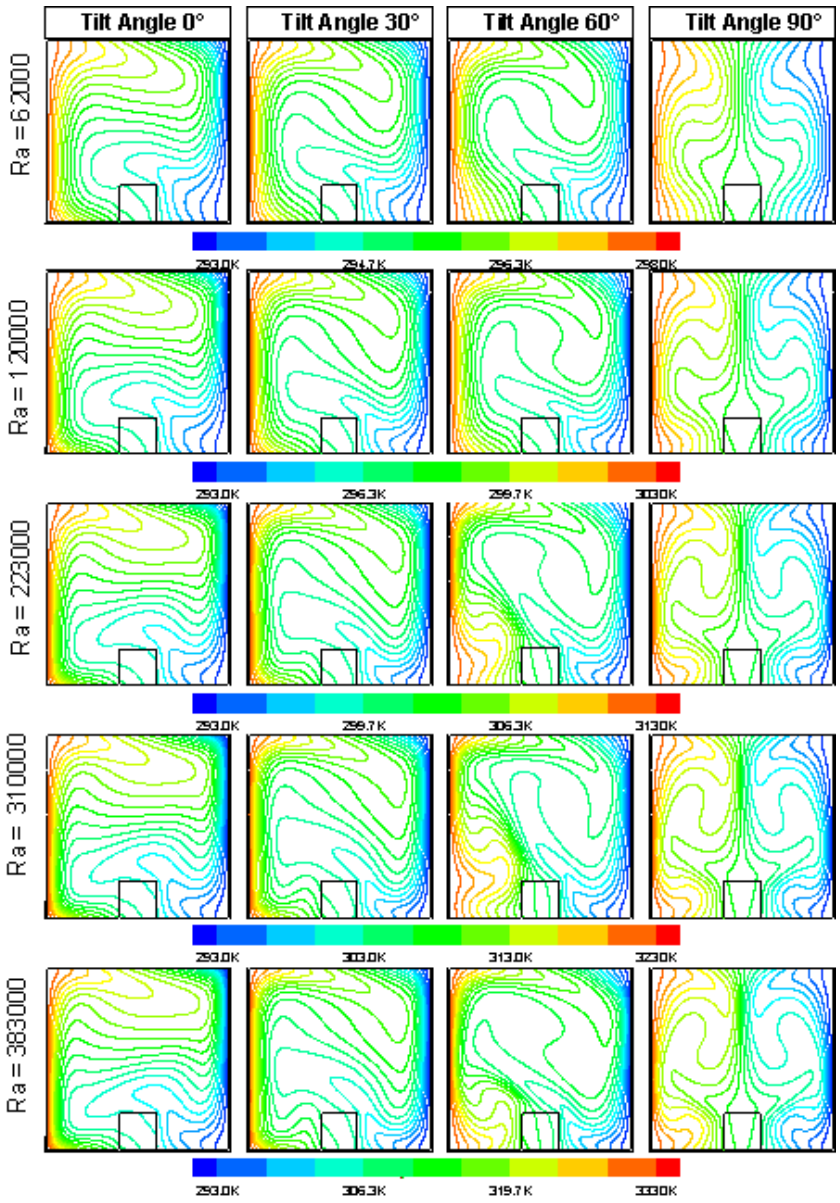

Figure 5.3: Numerical isotherms.

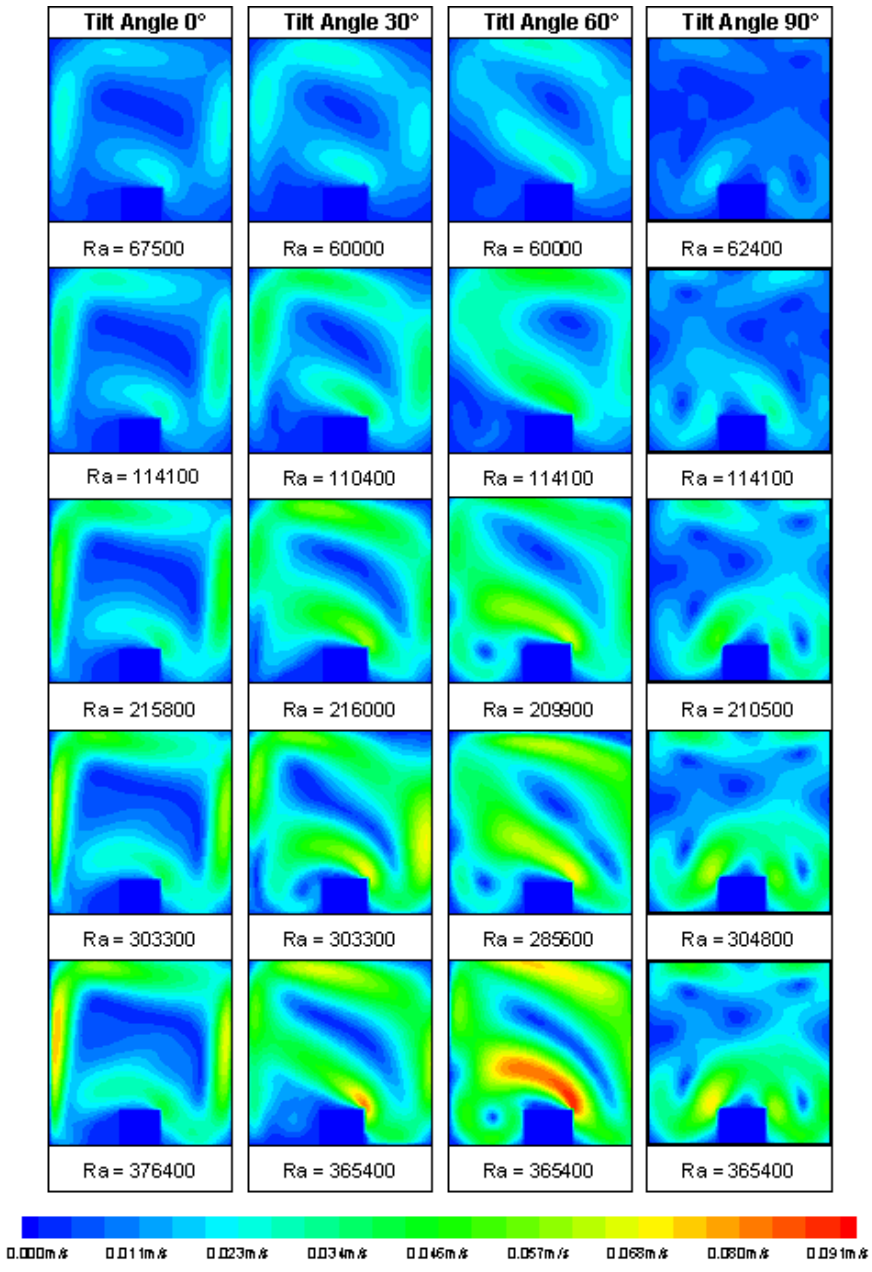

Figure 5.4: Experimental scalar velocity maps.

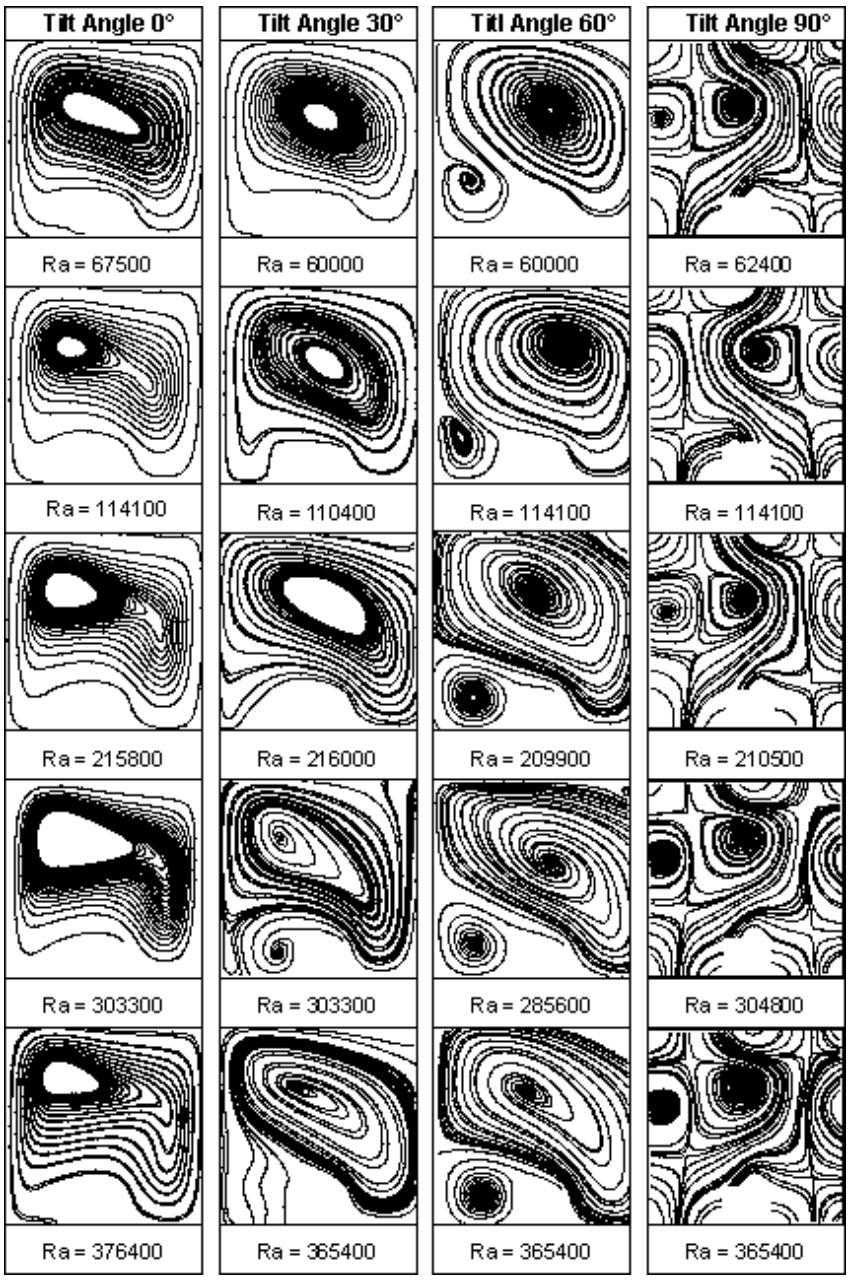

Figure 5.5: Experimental streamlines.

Table 5.1: Predicted (pure convection model) and measured maximum and average velocities. Comparison with Corvaro *et al.* [45] is also performed.

	Present study									**Corvaro *et al.* 2012 [45]**			
	Numerical			Experimental			Deviation			Numerical		Deviation	
θ	Ra	V_{max} m/s	V_{ave} m/s	Ra	V_{max} m/s	V_{ave} m/s	Ra %	V_{max} %	V_{ave} %	V_{max} m/s	V_{ave} m/s	V_{max} %	V_{ave} %
0	6.25×10^4	0.0245	0.0102	6.32×10^4	0.0242	0.0106	1.22	-1.17	4.38	-	-	-	-
	1.20×10^5	0.0361	0.0135	1.21×10^5	0.0354	0.0139	0.59	-2.10	3.41	0.0386	0.0137	-6.85	-1.78
	2.23×10^5	0.0517	0.0174	2.24×10^5	0.0506	0.0180	0.46	-2.08	3.00	0.0533	0.0174	-3.09	0.26
	3.10×10^5	0.0630	0.0201	3.10×10^5	0.0614	0.0204	0.28	-2.62	1.48	0.0710	0.0192	-12.77	4.45
	3.83×10^5	0.0721	0.0221	3.83×10^5	0.0694	0.0223	-0.15	-3.88	0.66	0.0766	0.0222	-6.26	-0.25
$\frac{\pi}{6}$	6.25×10^4	0.0298	0.0124	6.00×10^4	0.0285	0.0129	-4.17	-4.56	4.15	-	-	-	-
	1.20×10^5	0.0427	0.0166	1.10×10^5	0.0411	0.0171	-8.81	-3.88	2.76	0.0281	0.0095	34.14	42.93
	2.23×10^5	0.0575	0.0216	2.16×10^5	0.0605	0.0253	-3.06	4.86	14.73	0.0393	0.0114	31.67	47.20
	3.10×10^5	0.0700	0.0252	3.03×10^5	0.0702	0.0294	-2.07	0.23	14.47	0.0470	0.0127	32.89	49.53
	3.83×10^5	0.0806	0.0283	3.65×10^5	0.0815	0.0299	-4.88	0.99	5.52	0.0540	0.0138	33.04	51.17
$\frac{\pi}{3}$	6.25×10^4	0.0314	0.0124	6.00×10^4	0.0296	0.0129	-4.20	-6.25	3.80	-	-	-	-
	1.20×10^5	0.0484	0.0179	1.14×10^5	0.0480	0.0203	-5.28	-0.73	11.95	0.0123	0.0045	74.58	74.81
	2.23×10^5	0.0635	0.0240	2.10×10^5	0.0659	0.0273	-6.05	3.58	11.93	0.0163	0.0054	74.33	77.50
	3.10×10^5	0.0817	0.0302	2.86×10^5	0.0724	0.0319	-8.39	-12.97	5.49	0.0205	0.0066	74.92	78.12
	3.83×10^5	0.1015	0.0366	3.65×10^5	0.0911	0.0404	-4.88	-11.45	9.36	0.0234	0.0072	76.95	80.32
$\frac{\pi}{2}$	6.25×10^4	0.0185	0.0070	6.24×10^4	0.0200	0.0068	-0.10	7.53	-2.50	-	-	-	-
	1.20×10^5	0.0317	0.0129	1.14×10^5	0.0313	0.0112	-5.28	-1.16	-14.77	0.0016	0.0003	94.95	97.67
	2.23×10^5	0.0491	0.0208	2.11×10^5	0.0500	0.0188	-5.71	1.75	-10.79	0.0017	0.0003	96.54	98.56
	3.10×10^5	0.0623	0.0267	3.03×10^5	0.0630	0.0234	-1.55	1.06	-14.21	0.0016	0.0003	97.43	98.88
	3.83×10^5	0.0732	0.0315	3.65×10^5	0.0714	0.0291	-4.88	-2.62	-8.31	0.0015	0.0003	97.95	99.05

magnitude.

Local Nusselt number profile for each tilting angle and for the highest Rayleigh number is displayed in figure 5.6. A sharp peak characterizes the cases with $\theta = 0$, $\frac{\pi}{3}$ and $\frac{\pi}{2}$. These peaks are located respectively at $y/L \approx 0.2$, 0.5 and 0.4, in correspondence of the regions where the flow separated from the obstacle, reattaches itself to the hot wall. The peak is sharper for higher inclination angles and reaches its maximum value for $\theta = \frac{\pi}{3}$. A different profile with a more constant local Nu can be seen for $\theta = \frac{\pi}{6}$. This configuration presents two peaks: the first one at $y/L \approx 0.2$ where a particular recirculation zone with two different streams is observed behind the baffle. The second peak is located at $y/L \approx 0.6$ and is generated by the stream over the top of the divider.

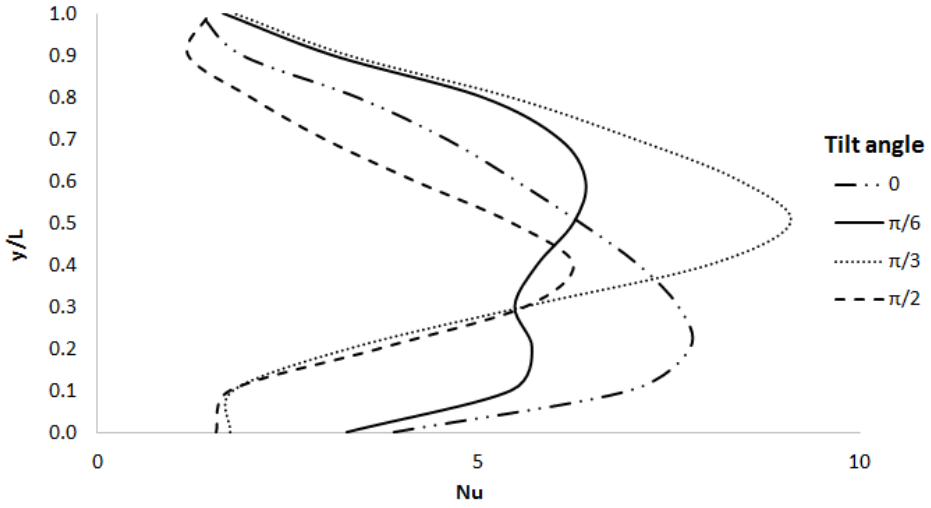

Figure 5.6: Numerical (pure convection model) local Nusselt number along the vertical hot wall for $Ra = 3.8 \times 10^5$.

The heat transfer rate across the hot wall is described by the average Nusselt number and its predicted value for the different cases is summarized in table 5.2. For each inclination angle $\overline{Nu}$ increases as the Rayleigh number increases, while for the same Ra the increase of the tilting angle causes a decrease in heat transfer rate. Corvaro *et al.* [45] found the same trend for a cavity without internal divider but in their study the reduction of the average Nusselt number is more emphasized, especially for the higher θ. Divergence between the two cases remains relatively limited (about the 5%) for $\theta = 0$ and progressively increases as the inclination angle increases until a maximum deviation of 30% ($\theta = \frac{\pi}{6}$), 120% ($\theta = \frac{\pi}{3}$) and 178% ($\theta = \frac{\pi}{2}$).

Table 5.2: Numerical average Nusselt number. Comparison with Corvaro *et al.* [45] is also performed.

	Present work				**Corvaro *et al.* (2012) [45]**				**Deviation**			
Ra	0	$\frac{\pi}{6}$	$\frac{\pi}{3}$	$\frac{\pi}{2}$	0	$\frac{\pi}{6}$	$\frac{\pi}{3}$	$\frac{\pi}{2}$	0	$\frac{\pi}{6}$	$\frac{\pi}{3}$	$\frac{\pi}{2}$
6.2×10^4	2.98	3.06	2.83	1.76	-	-	-	-	-	-	-	-
1.2×10^5	3.67	3.67	3.29	2.34	3.89	2.82	1.61	1.26	6	-30	-104	-86
2.2×10^5	4.48	4.41	3.79	2.90	4.62	3.59	1.71	1.24	3	-23	-121	-134
3.1×10^5	4.98	4.84	4.13	3.20	5.20	4.00	1.96	1.24	4	-21	-111	-158
3.8×10^5	5.34	5.12	4.32	3.39	5.70	4.26	2.00	1.22	6	-20	-116	-178

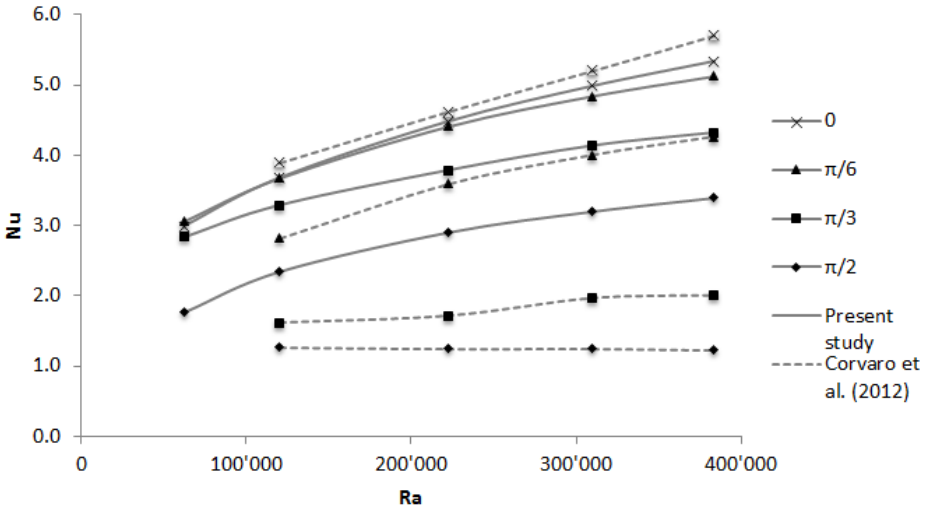

Figure 5.7: Numerical (pure convection model) average Nusselt number as a function of the Ra.

Chapter 6

Conclusions

Natural convection in a square cavity with an internal baffle and differentially heated from the side was investigated both experimentally and numerically. Air is the working fluid and the Rayleigh numbers examined range from 6.25×10^4 to 3.83×10^5. In case 1 the influence of the aperture ratio (or baffle height) and the influence of the baffle position have been studied. Moreover, the effect of radiation was considered to verify the importance of the radiative heat transfer compared to pure convection. In case study 2 the enclosure has been tilted with respect to the horizontal to simulate different directions of the gravity vector and analyze its effect on heat transfer. Experimental tests were carried out through Particle Image Velocimetry (PIV) technique; scalar velocity maps and streamlines maps were obtained as results. For each case, both maximum and average velocity values were extracted. A numerical investigation was performed using the CFD software ANSYS Fluent. Predicted velocity field maps were employed to verify the agreement between numerical and experimental results. Moreover, temperature maps and both local and average Nusselt number along the hot wall were used to complete the description of the phenomenon.

As seen in chapter 3 the presence of an internal adiabatic obstacle influences the flow field and the heat transfer within the cavity. In particular, a reduction of the heat transfer rate for the entire field of Rayleigh number can be observed. For a divider located in the middle of the floor, four different aperture ratios were examined; results show that the flow pattern is influenced by the Ra and A_p. For $Ra < 6.2 \times 10^5$ the velocity map seems symmetrical compared to the vertical axes passing through the center of the cavity. For higher Ra the flow becomes asymmetric and on the left side (near the hot wall) velocities are larger than on the right region (next to the cold wall). For the aperture ratio values of 4/5 and 3/5 the flow separation occurs behind the divider because the thermal field is horizontally stratified and the temperature difference is very low. Stream separation disappears as the aperture ratio reduces and for $A_p = 1/5$ the flow is divided into two different vortices on the side of the obstacle. Velocities increase as Ra increases and reach the maximum value for the highest aperture ratio. As regards the heat transfer, since the stream rises along the entire surface of the hot wall, the local Nu profile is rather constant. The average Nusselt number follows the same trend of the velocity and results show that if the convective flow is not completely developed, the heat transfer reduces. The aperture ratio plays an important role in heat transfer and Nu reduction in the worst case exceeds 60%, compared to an enclosure without division. As regards the influence of the divider position along the bottom wall, three different cases were evaluated at

$x/L = 3/10$, $1/2$ and $7/10$. The flow pattern is similar to the one previously described and it is characterized by a slow central stream and large velocities near the sidewalls. Velocities increase as Ra increases and they decrease as the aperture ratio decreases. In particular, for $A_p = 1/5$, since the divider leaves a small gap for the air passage, the convective current is divided into two distinct vortices. The baffle position mainly affects the region between the obstacle itself and the nearest vertical wall. The thermal stratification in that area prevents the flow inlet and the stream is forced to go toward the baffle if $x/L = 7/10$ or toward the higher part of the hot wall if $x/L = 3/10$. The different flow pattern next to the hot vertical surface causes a different heat exchange through the wall and therefore a particular local Nusselt number profile. When the baffle is located near the hot wall, the recirculated air removes a smaller amount of heat than the main stream from an area as large as the divider; two peaks can be seen in the local Nu profile. A single sharp peak appears for $x/L = 7/10$ because the main flow rises along the entire hot surface. Even though these profiles show some differences, the overall Nusselt number values are slightly different with a maximum deviation of 25%. The divider height has a stronger effect on the enclosures heat transfer than the divider position along the floor.

In case study 2 described in chapter 5 the same cavity with identical boundary conditions was used to investigate the combined influence of both the presence of a baffle and the direction of the gravity vector on natural convection. A simple configuration with central divider ($x/L = 1/2$) and an aperture ratio of $4/5$ was studied. Four tilting angles ($\theta = 0$, $\frac{\pi}{6}$, $\frac{\pi}{3}$ and $\frac{\pi}{2}$) were considered for a range of Rayleigh number between 6.25×10^4 and 3.83×10^5. The flow pattern within the cavity is considerably influenced by the direction of the gravity vector: the stream behind the baffle tends to arise instead of descending and in that region for $\theta \leq \frac{\pi}{6}$ a large vortex was generated by the convective flow. Velocities increase as Rayleigh number increases and decrease as θ increases. Maximum velocity is located near the hot wall for $\theta = 0$ but its position moved to the inactive top wall as the tilting angle increases. The case with $\theta = \frac{\pi}{2}$ can be considered alone because velocity field is quite different: four different vortices can be distinguished in the four edges of the enclosure. For this configuration both the flow and temperature pattern were perfectly symmetrical and the maximum velocity is reached in the center of the cavity where the two main streams join. Local heat transfer is affected by the different flow patterns and the local Nusselt number profiles show a sharp peak in correspondence of the area where the main stream is attached to the hot wall. Since for $\frac{\pi}{6}$ the recirculation area is larger, in this case, the Nu profile shows two peaks. The maximum overall Nusselt number deviation between the considered cases is 20% for $\theta \geq \frac{\pi}{3}$ but it arrives to 60% when $\theta = \frac{\pi}{2}$.

As regards the investigation method, PIV has proved to be an excellent system to measure the velocity field within the cavity. The flow analysis has been complex especially behind the divider where the presence of a small shadow cone prevented the correct display of the flow field. Moreover, the high deviation between the velocity of the main and secondary stream has complicated the simultaneous tracking of the entire flow field.

Natural convection was also numerically investigated using both a pure convective and a combined convective-radiative model. The aim of this analysis is to validate the numerical results obtained and understand the effect of radiative heat transfer on the flow within the cavity. The validation of numerical results is obtained comparing predicted velocity and streamlines maps with the experimental results: a good agreement was found and results are very close to each other. Using the pure convection model, deviation between numerical and measured values is generally lower than 11% and 8%

respectively for maximum and average velocities. The introduction of radiative heat transfer is difficult to evaluate. Radiation affects the zone between the hot wall and the divider and has a strong influence on the flow pattern in this reagion. It improves the description of the velocity field only when the baffle position is $x/L = 1/2$ and $7/10$ and for $A_p > 1/5$. However, if the agreement between predicted and experimental results is experessed in terms of maximum deviation, it reaches 16% and 10%.

Appendix A

Nomenclature

A.1 Latin Symbols

L	Characteristic dimension of the cavity, chosen equal to the side of the square section (m)
c_p	Specific heat (J/(kg K)
T	Temperature (°C)
Pr	Prandtl number
x	Abscissa, Cartesian axis direction
y	Ordinate, Cartesian axis direction
q''	Heat transfer rate (W/m^2)
h	Baffle height (m), Convective heat transfer coefficient (W/(m^2 K))
Nu	Local Nusselt number
$\overline{Nu}$	Average Nusselt number
s	Cavity length (m), Path lenght
Ra	Rayleigh number
D	Particle displacement (m)
$\mathbf{v}$	Velocity vector (m/s)
u	x-velocity component (m/s)
v	y-velocity component (m/s)
t	Time (s)
A_p	Aperture ratio ((L-h)/L)
p	Pressure (bar)

$\mathbf{g}$	Gravity acceleration vector ($\mathrm{m/s^{-2}}$)
$\mathbf{r}$	Position vector
d	Baffle width (m)
$\mathbf{s}$	Direction vector
s'	Scattering direction vector
a	Absorption coefficient
n	Refractive index
I	Radiation intensity (W)

A.2 Greek Symbols

α	Thermal diffusivity ($\mathrm{m^2/s}$)
β	Thermal expansion coefficient ($\mathrm{K^{-1}}$)
ΔT	Difference of temperatures between hot and cold walls (K)
δ	Thickness of the boundary layer (m)
ϵ	Emissivity
θ	Inclination angle of the cavity (rad)
λ	Thermal conductivity ($\mathrm{W/(m\,K)}$)
μ	Dynamic viscosity ($\mathrm{Pa\,s}$)
ν	Kinematic viscosity ($\mathrm{m^2/s}$)
ρ	Density ($\mathrm{g/m^3}$))
$\boldsymbol{\sigma}$	Stefan-Boltzmann constant ($\mathrm{W/(m^2\,K^4)}$)
$\boldsymbol{\sigma}_s$	Scattering coefficient
σ	Standard deviation
Φ	Phase function
ϕ	Azimuthal angle (rad)
Ω'	Solid angle (sr)

A.3 Subscripts

ave	Average
c	Cold
conv	Convective
h	Hot
max	Maximum
min	Minimum
ove	Overall
rad	Radiative
t	Thermal
w	Wall
∞	Quiescent condition

A.4 Acronyms

CCD	Change Coupled Device
CFD	Computational Fluid Dynamics
IA	Interrogation Area
PIV	Particle Image Velocimetry
PMMA	Polymethyl Methacrylate

Bibliography

[1] T V Radhakrishnan, A K Verma, C Balaji, and S P Venkateshan. "An experimental and numerical investigation of mixed convection from a heat generating element in a ventilated cavity". In: *Experimental Thermal and Fluid Science* 32.2 (2007), pp. 502–520 (cit. on p. xi).

[2] C Sanjuan, M N Sanchez, M del Rosario Heras, and E Blanco. "Experimental analysis of natural convection in open joint ventilated facades with 2D PIV". In: *Building and Environment* 46.11 (2011), pp. 2314–2325 (cit. on p. xi).

[3] F Corvaro, M Benucci, B Marchetti, F Polonara, and R C Grifoni. "The role of a novel frontal cover equipped with an adjustable electric resistance on the thermal performance of a central body radiator". In: *International Journal of Fluid Mechanics Research* () (cit. on p. xi).

[4] M M Alhazmy. "Internal baffles to reduce the natural convection in the voids of hollow blocks". In: *Building Simulation*. Vol. 3. 2. Springer. 2010, pp. 125–137 (cit. on pp. xi, 5).

[5] A Bairi. "Nusselt-Rayleigh correlations for design of industrial elements: Experimental and numerical investigation of natural convection in tilted square air filled enclosures". In: *Energy Conversion and Management* 49.4 (2008), pp. 771–782 (cit. on pp. xi, 40).

[6] D Das and T Basak. "Role of distributed/discrete solar heaters during natural convection in the square and triangular cavities: CFD and heatline simulations". In: *Solar Energy* 135 (2016), pp. 130–153 (cit. on p. xi).

[7] A Bairi, E Zarco-Pernia, and J M G De Mara. "A review on natural convection in enclosures for engineering applications. The particular case of the parallelogrammic diode cavity". In: *Applied Thermal Engineering* 63.1 (2014), pp. 304–322 (cit. on pp. xi, 7).

[8] D Duxbury. "An interferometric study of natural convection in enclosed plane air layers with complete and partial central vertical divisions." PhD thesis. University of Salford, 1979 (cit. on pp. 3, 4, 39).

[9] K H Winters. "The effect of conducting divisions on the natural convection of air in a rectangular cavity with heated side walls". In: *ASME Paper* 82-HT (1982), p. 69 (cit. on pp. 3, 4).

[10] M W Nansteel and R Greif. "Natural Convection in Undivided and Partially Divided Rectangular Enclosures". In: *Journal of Heat Transfer* 103 (1981), p. 623 (cit. on pp. 4, 6).

[11] M W Nansteel and R Greif. "An investigation of natural convection in enclosures with two- and three-dimensional partitions". In: *International Journal of Heat and Mass Transfer* 27.4 (1984), pp. 561–571 (cit. on pp. 4, 19, 39, 42).

[12] N N Lin and A Bejan. "Natural convection in a partially divided enclosure". In: *International journal of heat and mass transfer* 26.12 (1983), pp. 1867–1878 (cit. on pp. 4, 19).

[13] K H Winters. "Laminar natural convection in a partially divided rectangular cavity at high Rayleigh number". In: *International journal for numerical methods in fluids* 8.3 (1988), pp. 247–281 (cit. on p. 4).

[14] A T Kirkpatrik, M D White, and C B Winn. "Numerical study of high Rayleigh number natural convection flows in partitioned enclosures." In: 1987 (cit. on pp. 4, 40, 41).

[15] E Zimmerman and S Acharya. "Natural convection in an enclosure with a vertical baffle". In: *International Journal for Numerical Methods in Biomedical Engineering* 4.5 (1988), pp. 631–638 (cit. on pp. 4, 5, 39).

[16] R Jetli and S Acharya. "End wall effects on thermal stratification and heat transfer in a vertical enclosure with offset partitions". In: *The Canadian Journal of Chemical Engineering* 66.4 (1988), pp. 563–571 (cit. on pp. 4, 5).

[17] S Acharya and R Jetli. "Heat transfer due to buoyancy in a partially divided square box". In: *International journal of heat and mass transfer* 33.5 (1990), pp. 931–942 (cit. on pp. 4, 24, 39, 41, 42).

[18] D A Olson, L R Glicksman, and H M Ferm. "Steady-state natural convection in empty and partitioned enclosures at high Rayleigh numbers". In: *Journal of Heat Transfer* 112.3 (1990), pp. 640–647 (cit. on p. 4).

[19] S D Probert and J Ward. "Improvements in the thermal resistance of vertical, air filled, enclosed cavities". In: *Proc. 5th Int. Heat Transfer Conf.* 1974, pp. 124–128 (cit. on p. 5).

[20] H E Janikowski, J Ward, and S D Probert. "Free Convection in Vertical, Air-Filled Rectangular Cavities Fitted with Baffles". In: *Proc. 6th Int. Heat Transfer Conf.* Vol. 6. 1978, pp. 257–263 (cit. on p. 5).

[21] S M Bajorek and J R Lloyd. "Experimental investigation of natural convection in partitioned enclosures". In: *Journal of Heat Transfer* 104.3 (1982), pp. 527–532 (cit. on p. 5).

[22] R Jetli, S Acharya, and E Zimmerman. "Influence of baffle location on natural convection in a partially divided enclosure". In: *Numerical Heat Transfer, Part A: Applications* 10.5 (1986), pp. 521–536 (cit. on p. 5).

[23] R Jetli. "Natural convection in enclosures with offset baffles". PhD thesis. Louisiana State University, Baton Rouge, 1988 (cit. on p. 5).

[24] C Y Han and S W Baek. "The effects of radiation on natural convection in a rectangular enclosure divided by two partitions". In: *Numerical Heat Transfer: Part A: Applications* 37.3 (2000), pp. 249–270 (cit. on p. 5).

[25] E Bilgen. "Natural convection in enclosures with partial partitions". In: *Renewable Energy* 26.2 (2002), pp. 257–270 (cit. on p. 5).

[26] H Ambarita, K Kishinami, M Daimaruya, T Saitoh, H Takahashi, and J Suzuki. "Laminar natural convection heat transfer in an air filled square cavity with two insulated baffles attached to its horizontal walls". In: *Thermal Science and Engineering* 14.3 (2006), pp. 35–46 (cit. on p. 5).

[27] V A F Costa. "Natural convection in partially divided square enclosures: Effects of thermal boundary conditions and thermal conductivity of the partitions". In: *International Journal of Heat and Mass Transfer* 55.25 (2012), pp. 7812–7822 (cit. on p. 5).

[28] S Jani, M Mahmoodi, M Amini, and J E Jam. "Numerical investigation of natural convection heat transfer in a symmetrically cooled square cavity with a thin fin on its bottom wall". In: *Thermal Science* 18.4 (2014), pp. 1119–1132 (cit. on p. 5).

[29] Y S Sun and A F Emery. "Effects of wall conduction, internal heat sources and an internal baffle on natural convection heat transfer in a rectangular enclosure". In: *International Journal of Heat and Mass Transfer* 40.4 (1997), pp. 915–929 (cit. on p. 5).

[30] N Yucel and A H Ozdem. "Natural convection in partially divided square enclosures". In: *Heat and Mass Transfer* 40.1-2 (2003), pp. 167–175 (cit. on p. 5).

[31] P Kandaswamy, J Lee, A K A Hakeem, and S Saravanan. "Effect of baffle-cavity ratios on buoyancy convection in a cavity with mutually orthogonal heated baffles". In: *International Journal of Heat and Mass Transfer* 51.7 (2008), pp. 1830–1837 (cit. on p. 6).

[32] P Kandaswamy, A K A Hakeem, and S Saravanan. "Internal natural convection driven by an orthogonal pair of differentially heated plates". In: *Computers & Fluids* 111 (2015), pp. 179–186 (cit. on p. 6).

[33] A K A Hakeem, S Saravanan, and P Kandaswamy. "Buoyancy convection in a square cavity with mutually orthogonal heat generating baffles". In: *International Journal of Heat and Fluid Flow* 29.4 (2008), pp. 1164–1173 (cit. on p. 6).

[34] A K A Hakeem, S Saravanan, and P Kandaswamy. "Natural convection in a square cavity due to thermally active plates for different boundary conditions". In: *Computers & Mathematics with Applications* 62.1 (2011), pp. 491–496 (cit. on p. 6).

[35] F Corvaro and M Paroncini. "An experimental study of natural convection in a differentially heated cavity through a 2D-PIV system". In: *International Journal of Heat and Mass Transfer* 52.1 (2009), pp. 355–365 (cit. on p. 6).

[36] F Corvaro, G Nardini, M Paroncini, and R Vitali. "PIV and numerical analysis of natural convective heat transfer and fluid flow in a square cavity with two vertical obstacles". In: *International Journal of Heat and Technology* 33.2 (2015), pp. 51–55 (cit. on p. 6).

[37] B Alshuraiaan and K Khanafer. "The effect of the position of the heated thin porous fin on the laminar natural convection heat transfer in a differentially heated cavity". In: *International Communications in Heat and Mass Transfer* 78 (2016), pp. 190–199 (cit. on p. 6).

[38] J A Khan and Y Guang-Fa. "Comparison of natural convection of water and air in a partitioned rectangular enclosure". In: *International journal of heat and mass transfer* 36.12 (1993), pp. 3107–3117 (cit. on p. 6).

[39] K Hanjali, S Kenjere, and F Durst. "Natural convection in partitioned two-dimensional enclosures at higher Rayleigh numbers". In: *International journal of heat and mass transfer* 39.7 (1996), pp. 1407–1427 (cit. on p. 6).

[40] A Bairi, N Laraqi, and J M G de Maria. "Numerical and experimental study of natural convection in tilted parallelepipedic cavities for large Rayleigh numbers". In: *Experimental Thermal and Fluid Science* 31.4 (2007), pp. 309–324 (cit. on p. 7).

[41] A Bairi, J M G de Mara, N Laraqi, and N Alilat. "Free convection generated in an enclosure by alternate heated bands. Experimental and numerical study adapted to electronics thermal control". In: *International Journal of Heat and Fluid Flow* 29.5 (2008), pp. 1337–1346 (cit. on p. 7).

[42] B B Beya and T Lili. "Transient natural convection in 3D tilted enclosure heated from two opposite sides". In: *International communications in heat and mass transfer* 36.6 (2009), pp. 604–613 (cit. on p. 7).

[43] P Biswal, A Nag, and T Basak. "Analysis of thermal management during natural convection within porous tilted square cavities via heatline and entropy generation". In: *International Journal of Mechanical Sciences* 115 (2016), pp. 596–615 (cit. on p. 7).

[44] C Cianfrini, M Corcione, and P P Dell'Omo. "Natural convection in tilted square cavities with differentially heated opposite walls". In: *International Journal of Thermal Sciences* 44.5 (2005), pp. 441–451 (cit. on p. 7).

[45] F Corvaro, M Paroncini, and M Sotte. "PIV and numerical analysis of natural convection in tilted enclosures filled with air and with opposite active walls". In: *International Journal of Heat and Mass Transfer* 55.23 (2012), pp. 6349–6362 (cit. on pp. 7, 14, 76, 82–84).

[46] S M Elsherbiny and O I Ismail. "Heat transfer in inclined air rectangular cavities with two localized heat sources". In: *Alexandria Engineering Journal* 54.4 (2015), pp. 917–927 (cit. on p. 7).

[47] H Ozoe, H Sayama, and S W Churchill. "Natural convection in an inclined rectangular channel at various aspect ratios and angles-experimental measurements". In: *International Journal of Heat and Mass Transfer* 18.12 (1975), pp. 1425–1431 (cit. on p. 7).

[48] P K B Chao, H Ozoe, N Lior, and S W Churchill. "The Effect of Partial Baffles on Natural Convection in an Inclined Rectangular Enclosure PART I. Experimental Observations". In: *Chemical Engineering Fundamentals* () (cit. on p. 7).

[49] M Ghassemi, I Iran, M Pirmohammadi, and G Sheikhzadeh. "A Numerical Study of Natural Convection in a Tilted Cavity with Two Baffles Attached to its Isothermal Walls". In: () (cit. on p. 7).

[50] Z Altac and O Kurtul. "Natural convection in tilted rectangular enclosures with a vertically situated hot plate inside". In: *Applied Thermal Engineering* 27.11 (2007), pp. 1832–1840 (cit. on p. 7).

[51] Y Liu and N Phan-Thien. "A complete conjugate conduction convection and radiation problem for a heated block in a vertical differentially heated square enclosure". In: *Computational Mechanics* 24.3 (1999), pp. 175–186 (cit. on p. 7).

[52] H Bouali, A Mezrhab, H Amaoui, and M Bouzidi. "Radiation-natural convection heat transfer in an inclined rectangular enclosure". In: *International Journal of Thermal Sciences* 45.6 (2006), pp. 553–566 (cit. on p. 7).

[53] H Sun, E Chenier, and G Lauriat. "Effect of surface radiation on the breakdown of steady natural convection flows in a square, air-filled cavity containing a centered inner body". In: *Applied Thermal Engineering* 31.6 (2011), pp. 1252–1262 (cit. on p. 7).

[54] S Saravanan and C Sivaraj. "Combined natural convection and thermal radiation in a square cavity with a nonuniformly heated plate". In: *Computers & Fluids* 117 (2015), pp. 125–138 (cit. on p. 7).

[55] C Sivaraj and M A Sheremet. "Natural convection coupled with thermal radiation in a square porous cavity having a heated plate inside". In: *Transport in Porous Media* 114.3 (2016), pp. 843–857 (cit. on p. 7).

[56] A Yucel and S Acharya. "Natural convection of a radiating fluid in a partially divided square enclosure". In: *Numerical Heat Transfer* 19.4 (1991), pp. 471–485 (cit. on p. 7).

[57] P J Coelho, J M Goncalves, M G Carvalho, and D N Trivic. "Modelling of radiative heat transfer in enclosures with obstacles". In: *International Journal of Heat and Mass Transfer* 41.4-5 (1998), pp. 745–756 (cit. on p. 7).

[58] Dantec-Dynamics. *Dynamic Studio Software and Introduction to PIV Instrumentation*. Ed. by Gmbh. 2000 (cit. on p. 15).

[59] M Paroncini and F Corvaro. "Natural convection in a square enclosure with a hot source". In: *International journal of thermal sciences* 48.9 (2009), pp. 1683–1695 (cit. on p. 24).

[60] Fluent Incorporated. *FLUENT User's guide*. 2009 (cit. on p. 28).

[61] M W Nansteel. "Natural convection in Enclosures". PhD thesis. Department of Mechanical Engineering, University of California, 1982 (cit. on p. 39).